Heavy Quark Production at HERA

HABILITATIONSSCHRIFT

zur Erlangung der Habilitation
am Fachbereich Physik
der Universität Hamburg

vorgelegt von

Andreas B. Meyer

aus Bielefeld

Hamburg
2005

Abstract

Measurements of heavy quark production in ep collisions at HERA are reviewed. The experimental results collected so far provide key insights in the behaviour of the strong interactions, described by quantum chromodynamics, as well as in the structure of the proton, the photon and in heavy quark fragmentation mechanisms. The experimental methods for the study of heavy quark processes are presented. Based on the existing measurements, the program for future analyses is discussed.

Kurzfassung

Messungen der Produktion schwerer Quarks in ep-Kollisionen am Elektron-Proton Speicherring HERA werden dargestellt. Die bisher erzielten experimentellen Ergebnisse liefern wichtige Informationen über die durch die Quantenchromodynamik beschriebene starke Wechselwirkung, über die Struktur des Protons, des Photons und über Fragmentationsmechanismen. Die experimentellen Methoden zur Untersuchung der Prozesse mit schweren Quarks werden dargestellt. Ausgehend von den bisherigen Ergebnissen wird ein mögliches Programm für zukünftige Messungen entwickelt.

Contents

1 Introduction

Heavy quark production is a key process for the study of the theory of strong interactions, quantum chromodynamics (QCD). At the HERA storage ring at DESY, electrons of 27.6 GeV of energy are collided with 920 GeV protons, providing an ep center-of-mass energy of 318 GeV. HERA offers ample opportunities to study the production mechanisms of heavy quarks and to test all aspects of QCD, in both perturbative and non-perturbative regimes. In perturbative approaches the mass of the heavy quark m_q defines a 'hard' scale at which the strong interaction coupling constant α_S is evaluated and the condition $m_q \gg \Lambda_{QCD}$ implies that calculations in the framework of perturbative QCD should give reliable results. However, the steep energy dependence of the strength of the coupling constant (running of α_s) makes precise predictions difficult and leads to relatively large scale uncertainties. Processes in which no hard scale is present and α_S is large, e.g. the hadronization of heavy quarks into hadrons, are often described in phenomenological non-perturbative approaches.

The understanding of QCD, as one of the four fundamental forces of nature, is not only of principal interest in itself, it is also crucial for the search for physics beyond the Standard Model (SM). At many experiments the interpretation of the data depends on the precise knowledge of the rate of QCD processes, which are expected to form the most significant background at hadron colliders. The importance of a precise understanding of QCD is apparent when considering current and future accelerators, e.g. the Large Hadron Collider (LHC) which is anticipated to start in 2007. Many of these accelerators will have protons or photons as colliding particles with hadronic properties to be described in QCD.

Measurements of inclusive cross sections and exclusive final states have been performed both for electroproduction, often called Deep Inelastic Scattering (DIS), where the photon virtuality $Q^2 \gg \Lambda_{QCD}^2$, and for photoproduction ($Q^2 \sim 0$). The cross section in electron proton collisions is strongly dependent on Q^2. It is largest in photoproduction where the virtuality of the photon exchanged between the electron and the proton is very small, and the electron beam serves as a source of quasi-real photons with a wide energy distribution spanning the range between close to zero and the electron beam energy of 27.6 GeV. The photoproduction mechanism was previously studied extensively in fixed-target experiments using photon and lepton beams [1]. At HERA, the available center-of-mass energy is about one order of magnitude larger than at fixed-target facilities.

In the regime of deep inelastic scattering, the photon virtuality is large, $Q^2 \gg \Lambda_{QCD}^2$. Experimentally, the value of Q^2 is directly measurable at HERA at values larger than $Q^2 > 0.1$ GeV^2 up to values as large as 50000 GeV^2, the kinematic limit of Q^2 being the ep center of mass energy squared $s \approx 100000$ GeV^2. Heavy quark analyses have reached values of Q^2 as large as 1000 GeV^2. In the DIS regime, the photon virtuality Q^2 can be used as an energy scale for perturbative calculations and the validity of theoretical predictions as a function of the photon virtuality can be studied. Although the total rates are much smaller than those in photoproduction, the hadronic component of the photon is suppressed and more reliable theoretical and experimental results can be obtained.

Different theoretical approaches exist to describe the HERA data which are based on the factorization of the cross section into a hard scattering process, described by perturbative QCD,

1

and a non-perturbative part, given by the input distributions for the initial state partons in the proton and the exchanged photon and the hadronization of the final state particles.

Measurements of heavy quark production processes give access to a large number of theoretical and phenomenological issues and help to discriminate between the various models. Specifically, at HERA, heavy quark production processes can be used as a probe of the structure of the proton, and also the photon. The production of heavy quarks is directly sensitive to the gluon density in the colliding hadron which is most precisely determined from the scaling violations of inclusive structure function measurements. Measurements of heavy quark production, and also of other processes with exclusive final states, thus allow to test the universality of the parton density distributions. Furthermore, the fragmentation of the heavy quarks into the final state hadrons can be investigated and compared to existing results from other experiments.

In particular charm quarks are produced copiously at HERA. At sufficiently high photon virtualities, Q^2, the production of charm quarks constitutes up to 30% of the total cross section. In contrast, the inclusive beauty cross section is suppressed by the largeness of the b-quark mass and only becomes sizable ($\sim 10\%$) at $Q^2 \gtrsim 100$ GeV^2 where $Q^2 \sim (2m_b)^2$ or at large transverse momenta of the final state particles.

Heavy quark processes have been identified primarily using the 'golden channels' of resonance decays, $D^{*\pm} \to D^0\pi^\pm \to K^\mp\pi^\pm\pi^\pm$ [2–26] and $J/\psi \to \ell^+\ell^-$ [27–34]. Other resonances, such as D^+, D_s and Λ_c have also been reconstructed [6, 20, 26, 35]. More recently, charm and beauty analyses have been published using semi-leptonic decay channels [36–42] and/or lifetime tags using inclusive data samples [43–46]. Furthermore, first measurements in which both heavy quarks are identified [42, 47, 48] have been performed, the results of which provide sensitivity to further details of the heavy quark production process. Finally, the HERA experiments have been able to perform a number of spectroscopic analyses in which the wealth of charm events is exploited to perform searches for higher excitation resonances, such as D_1, D_2, [49, 50] and exotic bound states, such as pentaquarks [51–54]. $D^{*\pm}$ mesons have also been used to measure the production of charm in diffractive processes [55–58]. A discussion of the physics of open charm production in diffraction is however not included in this report.

Experimentally, the measurements of heavy quark production at HERA require extensive use of precision information from many parts of the detector. While the total cross section for heavy flavour production is relatively large, the small branching ratios for specific decay channels and limited detector acceptances usually lead to a substantial reduction of the size of the event samples useful for the heavy quark analyses. Various experimental techniques to identify heavy quark processes and to measure specific properties have been established and are discussed in this report.

This report is structured as follows: An overview of the theory of heavy quark production is given in section 2. Event generator programs for the simulation of heavy quark events and the calculation of cross sections are presented in section 3. The H1 and ZEUS detectors are described in section 4 and the experimental techniques are discussed in section 5. The experimental results obtained so far are presented and confronted with theory calculations (section 6). Finally, in section 7, future opportunities for further studies with heavy quarks at HERA are discussed.

2 Theory

The dominant production process of heavy quarks at HERA has been seen to be the boson-gluon fusion process (BGF) which is depicted in fig. 1. Theory calculations use a factorization

Figure 1: Diagram of the process of Boson-Gluon Fusion in ep-scattering.

ansatz in order to arrive at cross section predictions which can be compared with experimental data. In these factorization approaches, the cross section is composed of a non-perturbative part, which is given by the parton distributions of the initial state particles f_j^p, the perturbative evolution according to the evolution equation and a perturbative hard scattering process, i.e. the photon-parton cross section $\hat{\sigma}_{\gamma j}$, which is calculable in perturbative QCD:

$$\sigma_{dir}^{\gamma p}(P_\gamma, P_p) = \sum_i \int dx \, f_j^p(x, \mu_F) \, \hat{\sigma}_{\gamma j}(P_\gamma, x P_p, \alpha_s(\mu_R), \mu_R, \mu_F, \mu_\gamma). \tag{1}$$

In addition, to predict production cross sections for heavy hadrons and/or other exclusive final states, the fragmentation of the heavy quark into a hadron and additional final state particles are considered. Based on the assumption of universality, the non-calculable non-perturbative parts, i.e. usually the parton distributions and fragmentation functions are taken from measurements of other processes at HERA or other experiments. A number of conditions apply to HERA:

- Heavy quark processes are particularly well measurable at HERA in the region of Bjorken-x between 10^{-4} and 10^{-2}. In this region, gluons are the dominant partons in the proton. The heavy quark cross section is thus directly sensitive to the gluon density distribution in the proton. The kinematic range probed by HERA is relevant for the calculations of cross sections at future experiments, e.g. at the LHC.

- In photoproduction the incoming almost real photon may fluctuate into a hadronic state before undergoing a hard collision. The corresponding contribution to the cross section is referred to as **resolved**, in contrast to the case where the photon directly interacts with the hadron (**direct** or point-like). Separation of a cross section into a direct and resolved component is ambiguous beyond leading order: different choices of the factorization schemes lead to different definitions of the two components.

- For heavy quark processes the calculation of the 'hard' matrix element using perturbative QCD is facilitated by the heaviness of the quarks. Already the charm quark mass provides an energy scale, which allows perturbative expansion. Other possible scales are the photon virtuality Q^2 (for DIS) or the transverse momentum p_t of the final state particles (jets). Calculations for multi-scale processes, such as the production of charmed jets in DIS, have become available recently. Different approaches for the choice of the scale exist and are discussed below.

- The fragmentation of the heavy quark into a hadron and additional final state particles is usually described by phenomenological parameters as determined from experimental data. Fragmentation functions describing the longitudinal momentum transferred from the quark to the heavy hadron, and fragmentation fractions, describing the probability of a quark to hadronize into a particular hadron, have been measured primarily at e^+e^- colliders (such as LEP). Recent results at HERA have shown that the uncertainty by the use of parameters as determined at LEP is reasonably small.

2.1 Perturbative Calculations

Perturbative QCD calculations can be performed in the formalism of collinear factorization in which the DGLAP evolution equations [59] are used to describe the radiation of partons from the initial parton distribution in the proton and in the photon. In the collinear factorization ansatz the parton distributions in the proton (and the photon) are assumed to depend only on the scaling variable x and an energy scale μ, usually the photon virtuality Q^2. In particular, the initial partons in the proton are assumed to carry no transverse momentum. In the evolution, the partons are treated as massless on-shell particles. Factorization and renormalization scale parameters are used to absorb divergent parts of the perturbation series into parton distributions and α_S. In the DGLAP scheme, calculations up to next-to-next-to-leading order (NNLO) have become available recently, e.g. for inclusive cross sections [60].

In other approaches, such as the BFKL evolution equation [61–64], and later the CCFM evolution equation [65], the so-called k_t factorization formalism is used which is described in section 2.5.

Heavy Quark production poses a particular theoretical challenge as the presence of the heavy quark mass m_c or m_b introduces a new scale into the perturbative calculations. Quantitative calculations for heavy quark production at HERA have been performed by a number of authors, providing detailed results up to next-to-leading order in perturbation theory. Predictions for inclusive heavy quark distributions, as derived from fits to inclusive data from HERA and fixed target experiments [66–69], are available as a function of Q^2 and x. In global fits also other data, such as dijet data have been used [70–76]. Predictions for exclusive processes in which the topologies of the two quarks are explicitly taken into account, are available as a function of a number of variables, such as the transverse momenta p_t and/or pseudo-rapidity η for one or both of the heavy quarks and/or jets (see section 2.1).

Different schemes to calculate heavy quark production processes have been developed in the framework of collinear factorization which are expected to be valid in different kinematic regions:
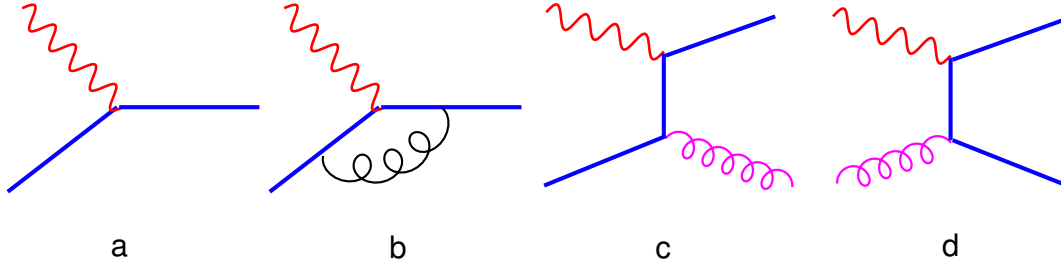
Figure 2: Leading diagrams for heavy quark production in the massless scheme at leading order (a) and next-to-leading order (b-d).

- In calculations for processes with light quarks, the mass of the light quarks is assumed to be zero. The quarks are treated as active partons in the proton, i.e. a density distribution for the quarks in the proton is used to describe the non-perturbative part of the calculation. The perturbative series is expanded using a scale-parameter μ as given by the photon virtuality Q^2 or the jet momentum p_t. Perturbative calculations are expected to converge for $\mu \gtrsim \Lambda_{QCD}$. Due to the heaviness of the quark mass m_q, this approach does not work for heavy quarks except in the extreme limit $\mu \gg m_q$, in which the heavy quarks can be treated as massless. In this 'massless' scheme, at leading order (LO), the quark parton model (QPM) process ($\gamma q \to q$, fig. 2a) is the dominant contribution. At next-to-leading order (NLO), virtual corrections are included (fig. 2b) and the QCD Compton ($\gamma q \to qg$, fig. 2c) and photon gluon fusion ($\gamma g \to q\bar{q}$, fig. 2d) processes also contribute. The massless approach is often referred to as the zero mass variable flavor number scheme (ZM-VFNS) [70, 71]. In this approach the heavy quarks are treated as infinitely massive below some scale $\mu \sim m_q$ and massless above this threshold.

- At values of $\mu^2 \sim M^2$, the 'massive' scheme [77–79], in which the heavy flavor partons are treated as massive quarks is more appropriate. In the massive scheme the dominant LO process is photon gluon fusion (PGF, fig. 3a) and the NLO diagrams are of order α_s^2 (figs. 3b-c). The scheme is often referred to as the fixed flavor number scheme (FFNS). As μ^2 becomes large compared to M^2, the FFNS approach is unreliable due to large logarithms in $\ln(\mu^2/M^2)$ in the perturbative series. Generator programs in this scheme which are applicable to HERA physics are available to next-to-leading order (FMNR [80], HVQDIS [81]). The fixed order massive scheme is also used in various Monte Carlo event generator programs which implement leading order matrix elements and parton showers to simulate higher order effects. A description of these programs is given in section 3.

- In order to provide reliable pQCD predictions for the description of heavy flavor production over the whole range in μ^2, composite schemes which provide a smooth transition from the massive description at $\mu^2 \sim M^2$ to the massless behavior at $\mu^2 \gg M^2$ have been developed. These composite schemes are commonly referred to as variable flavor number schemes (VFNS). The VFNS approach has been incorporated in various different forms to order α_s [75, 82–88] and to order α_s^2 [89, 90].

  In resummed or 'matched' next-to-leading-order QCD predictions the divergent logarithms are controlled by resummation techniques. Here, matched means that measures
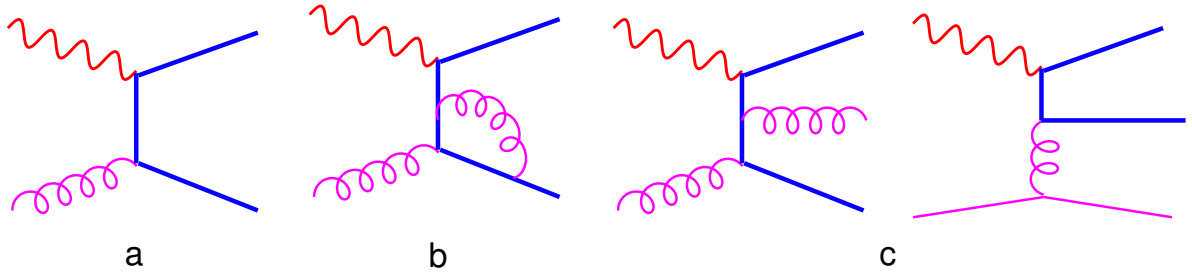
Figure 3: Leading diagrams for heavy quark production in the massive scheme at leading order (a) and next-to-leading order (b-d).

are taken to avoid double-counting of contributions which are contained in both the perturbative and the resummed part of the calculation, i.e.

$$\mathrm{FONLL} = \mathrm{FO} + (\mathrm{RS} - \mathrm{FOM0}) \times G(m, p_t), \qquad (2)$$

where FONLL stands for fixed-order plus next to leading logarithms, and FO is the fixed order, $\mathcal{O}(\alpha_{em}\alpha_s^2)$ result. RS is the resummed result, which includes all terms of the form $\alpha_{em}\alpha_s(\alpha_s \log p_t/m)^i$ and $\alpha_{em}\alpha_s^2(\alpha_s \log p_t/m)^i$ and neglects all terms suppressed by powers of the heavy quark mass m. FOM0 is the massless limit of FO, in the sense that all terms suppressed by powers of m are dropped, while logarithms of the mass are retained; thus FOM0 is the truncation of RS to order $\alpha_{em}\alpha_s^2$. $G(m, p_t)$ is an arbitrary dumping function, that must be regular in p_t, and at large p_t, it must approach unity up to terms suppressed by powers of m/p_t. In the matched calculation FONLL [87, 88, 91–93] differential cross sections are calculated to next-to-leading-log precision using perturbative fragmentation functions [94]. A similar approach is pursued in [95–100]. Here, the ZM-VFNS is used as a starting point, adjusting the factorization scales such that the massive calculation is reached for $m \to 0$.

2.2 Proton Structure

The process of heavy quark production is directly sensitive to the distributions of heavy quarks (massless approach, fig. 2) and/or gluons (massive approach, fig. 3) in the proton. In global fits to inclusive data, the gluon distribution $g(x, Q^2)$ is extracted by analysis of the scaling violations of the proton structure function assuming a certain functional form for $xg(x, Q^2)$. In contrast, heavy quark processes can be used to determine the gluon distribution directly, i.e. by reconstruction of the kinematics of the interacting partons from the measurement of the hadronic final state. Such direct measurements are complementary to the indirect analyses and – although still limited in statistics – they are in principle more sensitive to local variations. In fig. 4 a comparison is shown of the gluon distribution as extracted from global fits and from two sets of charmed $D^{*\pm}$-meson data collected at H1 in DIS and in photoproduction [4]. The gluon density is extracted from the D^* cross section using an unfolding procedure in which effects from gluon radiation and fragmentation are removed. The relative contribution from D^* production via quarks from the proton is subtracted. For the different bins of the measurement the gluon densities are obtained at different factorization scales as given by the phase space of the particular bin and evolved to a scale $\mu^2 = 25 \, \mathrm{GeV}^2$.
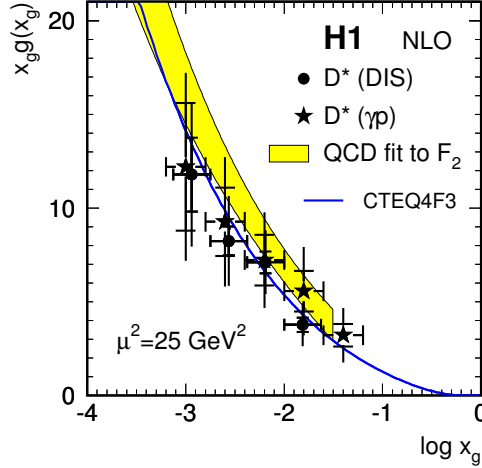
Figure 4: Gluon distributions $xg(x, Q^2)$ as extracted from D^* data [4]. The systematic error is a quadratic sum of all contributions and is dominated by the theoretical uncertainty on the charm quark mass (DIS sample) and the renormalization and factorization scale (photoproduction).

2.3 Photon Structure

In deep inelastic scattering the finite photon virtuality ensures that the timescale at which the process takes place is short and the photon acts like a point-like exchange boson. Towards smaller photon virtualities the photon becomes quasi-real and in photoproduction it can fluctuate into a hadronic final state. In resolved-photon processes (figs. 5b to d), the photon fluctuates into a hadronic state before the hard interaction and acts as a source of partons, one of which takes part in the hard interaction. Like for protons, the structure of resolved photons can be described by a photon structure function.

The size of these photon structure functions depends both on the approach in which the parton evolution is described (DGLAP, BFKL or CCFM equations) and on the order of the perturbative expansion. In the DGLAP approach, at next-to-leading order, most of the photon-structure is included in the hard matrix elements and the contributions from processes with resolved photons becomes small ($\lesssim 5\%$). Calculations using k_t factorization are able to give a reasonable description of the contributions from resolved photons already at leading order.

Parton density distributions for the photon have been extracted from measurements e.g. in $\gamma\gamma^*$ collisions at LEP [101]. In so-called Hadron-like processes a gluon from the photon interacts with a gluon from the proton (gluon-gluon-fusion, fig. 5b) to form a quark anti-quark final state. In contrast, in excitation processes (figs. 5c and d) the heavy quark is a constituent of the resolved photon. These contributions are relevant in the massless scheme where the heavy quarks are active partons in the photon. The two excitation diagrams differ mainly in the propagators of the hard matrix element. While the quark (i.e. fermion) propagator should cause the cross section to follow a $(1 - \cos\theta^*)^{-1}$ behavior the gluon (i.e. boson) propagator defines a $(1 - |\cos\theta^*|)^{-2}$ behavior, as in Rutherford scattering. Here, θ^* is the polar angle between the final state charm quark and the proton direction in the center-of-mass frame of the incoming hard partons.

Experimentally, the signature for resolved photon processes is the presence of a photon remnant, i.e. a low momentum hadronic final state which carries away part of the initial photon
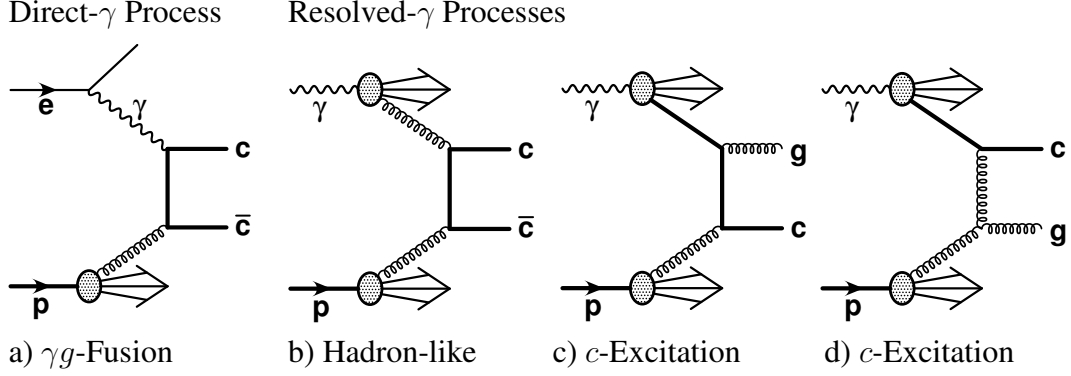
7

Direct-γ Process   Resolved-γ Processes

a) γg-Fusion   b) Hadron-like   c) c-Excitation   d) c-Excitation

Figure 5: Dominant diagrams in leading order pQCD for heavy quark photoproduction at HERA. The c in the diagrams stands for both charm and beauty. Note that the distinction between resolved and direct processes becomes ambiguous at next-to-leading order as the next-to-leading order diagrams contain contributions in which a gluon is one of the two leading final state partons.

energy which is not transfered to the parton participating in the hard process. In dijet events, the two leading jets provide a measure of the two hard final state partons and the fraction of the photon energy, in the proton rest frame, entering the hard interaction can be estimated using the observable

$$x_\gamma^{obs} = \frac{\sum_{Jet_1}(E - p_z) + \sum_{Jet_2}(E - p_z)}{\sum_h (E - p_z)}, \qquad (3)$$

where the sums in the numerator run over the particles associated with the two jets and that in the denominator over all detected hadronic final state particles. The measured jet kinematics are used to approximate the kinematics of the partons before the hadronization.

For the direct process (fig. 5a), x_γ^{obs} approaches unity, as the hadronic final state consists of only the two hard jets and the proton remnant in the forward region which contributes little to $\sum_h (E - p_z)$.

Detailed studies of the heavy quark final states separately for resolved-type ($x_\gamma^{obs} \lesssim 0.75$) and direct-type ($x_\gamma^{obs} \gtrsim 0.75$) events allow to gain quantitative understanding of the size of the different contributions and allow to test the assumption of universality of the photon structure function. Data analyses in which jets from gluons and quarks can be distinguished and different final state topologies can be separated, may be able to provide further tests of the validity of these concepts[1].

The contribution from resolved-photon processes is expected to vanish towards larger photon virtualities. First measurements however, indicate that the suppression of resolved-type events towards larger photon virtualities occurs much more slowly for charm than for light quark events [102]. This is shown in fig. 6 where only a small or no suppression of the resolved-type contribution as a function of Q^2 is seen. The data tend to disprove the expectation from the AROMA Monte Carlo generator [103] which implements only the direct matrix element, in the massive scheme. In contrast, the CASCADE Monte Carlo program [104] describes the

---

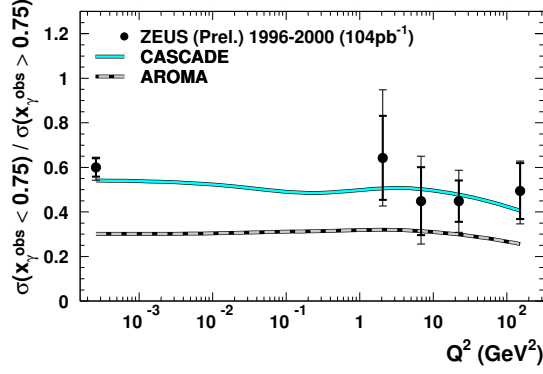[1]For a more detailed discussion see section 6.1.3.

Figure 6: Ratio of resolved-like to direct-like cross sections of dijet events containing a D^* meson as measured by ZEUS (preliminary) as a function of photon virtuality Q^2 (taken from [102]). Also shown are the expectations from the Monte Carlo generator AROMA [103] and CASCADE [104].

data rather well. In CASCADE, certain resolved-like contributions to the cross section are effectively implemented by use of the k_t factorization ansatz, as mentioned above. AROMA and CASCADE, as well as other Monte Carlo generator programs commonly used at HERA, are described in detail in section 3. Measurements based on larger statistics are necessary to determine the contribution from resolved processes as a function of Q^2 more precisely, and to improve the understanding of the interplay between the various hard scales and the hadronic contributions from the photon.

2.4   Fragmentation

In order to compare the calculations performed at parton level with measurements of final states the fragmentation and hadronization of the partons into hadrons have to be taken into account. While the parton interactions are treated in perturbation theory, the subsequent hadronization into measurable hadrons is usually described by phenomenological models. The transition from the heavy quark to a heavy hadron is usually divided into two aspects:

- Fragmentation functions describe the transfer of the quark's energy to a given hadron. Many forms of fragmentation functions exist, the most prominent being the Lund string model [105, 106], as implemented in the JETSET [107] and PYTHIA [108] Monte Carlo event generators, and the Peterson fragmentation function [109] which has the form

$$f(z) \propto \frac{1}{z(1 - 1/z - \epsilon/(1-z))^2} \tag{4}$$

where ϵ is a free parameter. The size of the parameter depends on the order of the perturbative calculation. In leading order calculations it absorbs effects that are contained in next-to-leading order calculations. A number of alternative parameterizations are available [110–112], some of which have been seen to be successful in describing the LEP data. In the parameterization by Kartvelishvili et al. [113],

$$f(z) \propto z^\alpha (1 - z) \tag{5}$$

9

and α is an adjustable parameter. The most precise measurements of the fragmentation parameters come from experiments at e^+e^- colliders where the knowledge of the initial state kinematics provides powerful constraint for these measurements and effects from interactions between the final state and the beam ('beam drag' [114]) are absent.

- Fragmentation ratios are used to describe the probability $f(h \to H)$ with which a heavy quark h hadronizes to form a heavy hadron H. For charm hadrons the fragmentation ratios have been measured to great accuracy at LEP [115, 116] and these measurements have generally been used in measurements at HERA to determine the charm quark cross sections from the measured rates of produced charmed hadrons. Many of the Monte Carlo simulations (as described in section 3) have been tuned to the measured values. Fragmentation ratios for higher excited states of hadrons (such as D^{**} and D_s) have only poorly been measured. Recent measurements indicate that excited heavy hadron states which subsequently decay via the strong interactions into ground state hadrons are more copiously produced than previously assumed [117]. The fragmentation function parameters obviously depend on the assumed fragmentation ratio for these decays. Consequently, analyses of these parameters need to take these correlations into account.

2.5 k_t Factorization

In the k_t factorization approach [118–121], to be used with the BFKL [61–64] or CCFM [65] evolution equations, parameters additional to x and Q^2 are used to describe the distribution of the partons in the proton. The unintegrated gluon density as a function of x, Q^2 and k_t, folded with off-shell matrix elements, is determined through fits to proton structure function data as measured at HERA [66, 67], where k_t denotes the transverse parton momentum emitted along the cascade. In unintegrated parton distributions, the dependence on the transverse parton momentum k_t emitted along the cascade is not integrated out. This is in contrast to the DGLAP approach in which, usually, the gluon density is integrated in that it only depends on the energy fraction x and on the squared transverse momentum transfer Q^2.

The partons entering the hard scattering matrix element are free to be off-shell, in contrast to the collinear approach (DGLAP) which treats all partons entering the hard subprocess as massless. Off-shell matrix elements of heavy flavor lepto- and hadroproduction processes have been calculated in [122, 123]. The CCFM evolution equations can be used with k_t factorization and they apply angular ordering which is a consequence of color coherence, i.e. due to the interference properties of the radiated gluons. As a result in the appropriate limit they reproduce the DGLAP [59] and the BFKL [61–64] approximation. At small values of the parton momentum fractions z, a random walk of the transverse parton momenta k_t is obtained.

3 Event Generators

3.1 Leading Order Parton Shower Calculations

Monte Carlo generator programs are commonly used to model physics processes. They provide samples of single events with their full set of initial state, intermediate and final state particles which follow distributions as predicted by the underlying QCD calculation. The fact that single physics events can be analyzed gives particular strength to Monte Carlo simulations: Both parton and hadron-level are accessible and detector effects, which lead to finite resolutions for the measurement of the particles, can be simulated by feeding the generated list of particles through detector simulation programs.

At HERA, the most commonly used Monte Carlo programs for the modeling of heavy quark physics are: PYTHIA [108], RAPGAP [124], AROMA [103] and HERWIG [125]. These programs are based on the DGLAP evolution equations [59] and provide leading order calculations of the cross sections. Recently, the Monte Carlo program CASCADE [104] was introduced which contains an implementation of the k_t factorization approach using the CCFM evolution equation [65], described in section 2.5.

In most Monte Carlo programs, and also in CASCADE, the formation of hadrons is simulated using the LUND string model [108] as implemented in JETSET [107]. Optionally, for heavy quarks, the Peterson fragmentation function [109] can be used. In HERWIG, a cluster algorithm is used to form hadrons from clusters of quark-antiquark states in a color-singlet configuration.

3.1.1 Monte Carlo Event Generators Using Collinear Factorization

In the Monte Carlo simulations based on the DGLAP evolution, collinear factorization of the parton density distributions and the hard matrix elements is assumed. In the DGLAP approximation the evolution from the partons density distributions leads to a strong ordering of radiated partons in transverse momentum k_t. The matrix elements are evaluated at leading order and effects from higher orders are mimicked using parton showers (PS) which are radiated from the initial and final state partons using a soft collinear approximation. The acronym LO+PS is generally used to indicate programs that implement the combination of leading order matrix elements with parton showers.

- The PYTHIA Monte Carlo generator [108] implements a number of different approaches to calculate ee, ep and pp cross sections and distributions. For the simulation of heavy quark production in ep scattering, most commonly, PYTHIA is used in the massive mode in which c and b quarks are generated dynamically using the boson-gluon fusion process. Alternatively, PYTHIA can be used in an inclusive mode in which direct and resolved events are generated using massless matrix elements for all quark flavours. Many analysis have confirmed that PYTHIA describes the shapes of event distributions in photoproduction impressively well. In contrast, the Q^2 distribution in electroproduction is, for most parameter choices, poorly described.

11

- The RAPGAP Monte Carlo generator [124] produces events using the massive approach. In contrast to older event generators, such as DJANGO [126] or AROMA [103], it provides a correct treatment of the diffractive contribution of inclusive scattering which makes up about 10% of the cross section. RAPGAP is interfaced with the program HERACLES [127] which simulates QED initial and final state radiation.

- AROMA [103] is a program to simulate the production of heavy quarks in the direct photon-gluon fusion process in ep scattering. AROMA does not include the generation of cross section contributions from resolved photon processes, and is thus of limited use for the photoproduction, and possibly the low-Q^2 regime, at HERA.

- HERWIG [125] is a general purpose physics event generator which includes the simulation of hard lepton-lepton, lepton-hadron and hadron-hadron scattering and soft hadron-hadron collisions in one package. HERWIG implements the cluster hadronization approach to describe the fragmentation of quarks into hadrons via non-perturbative gluon splitting. The colored objects in the final state are combined to color-singlet clusters which are subsequently fragmented into hadrons.

3.1.2 Monte Carlo Simulations Using k_t Factorization

The Monte Carlo generator CASCADE [104] contains an implementation of the k_t factorization approach (see section 2.5) using the CCFM evolution equation [65]. In CASCADE the direct heavy quark production processes $\gamma g \to c\bar{c}$ and $b\bar{b}$ are implemented using off-shell matrix elements convoluted with k_t-unintegrated parton distributions in the proton. In CASCADE, higher order parton emissions based on the CCFM [65] evolution equations are matched to $\mathcal{O}(\alpha_s)$ matrix elements in which the incoming parton can be off-shell. This implies that the parton kinematics are treated correctly. For the final state parton showers PYTHIA [108] is used. The unintegrated gluon density in the proton has been determined in fits to the inclusive structure function data, in the range $x < 10^{-2}$ and $Q^2 > 5$ GeV^2. With this input CASCADE has been able to correctly reproduce the b quark production cross-sections in $p\bar{p}$-collisions at the Tevatron [128].

3.2 Next-to-Leading Order Calculations

Calculations to next-to-leading order are expected to provide more reliable estimates of the total rates as they account for the presence of hard parton emissions. Furthermore, next-to-leading order calculations are necessary for the determination of fundamental parameters such as α_S and the parton density distributions. At next-to-leading order, the different diagrams produce both positive and negative contributions to the cross section. The negative contributions make it difficult to implement next-to-leading order calculations in full hadron level Monte Carlo event generators.

3.2.1 Fixed Order Parton Level Calculations

ep and γp event generators to next-to-leading order are available at the parton level. The program FMNR [80] implements cross section calculations for the photoproduction regime and the program HVQDIS [81] for the DIS case. Both programs are based on calculations in the massive scheme and provide weighted parton level events with two or three outgoing partons, i.e. a b quark, a $\bar{b}$-quark and possibly an additional light parton.

For calculations of 'visible' cross sections, such as D^* cross sections the programs can be extended to include the fragmentation of the heavy quarks into hadrons and optionally decays of the hadrons into final states e.g. with leptons. In a simple approach, the heavy quarks are 'hadronized' into a heavy hadrons by rescaling the three momentum of the quark according to the distribution as given by a fragmentation function. Usually, the Peterson fragmentation function [109] is used with parameter choices, e.g. as those determined in [129].

For the calculation of cross sections involving jets, a jet algorithm, e.g. the inclusive k_t algorithm (see section 5.4), is used on the final state partons, yielding parton level jets. For the comparison with experimental measurements – which are usually given at the hadron level, i.e. including fragmentation and hadronization effects – parton-to-hadron level corrections are applied to the parton level results. These corrections should in principle be performed in the same scheme (NLO) as the parton level calculations. However, for lack of more appropriate choices LO+PS Monte Carlo event generators (such as PYTHIA, HERWIG, RAPGAP or CASCADE described above) are commonly used to calculate the parton-to-hadron level corrections. The corrections range typically from -30% to $+5\%$ in both photoproduction and DIS, decreasing towards larger values of Q^2 and/or jet transverse momentum.

The theoretical uncertainties of the NLO calculations are estimated in the following way: For the heavy quark mass m_q, typically, central values of $m_c = 1.5$ and $m_b = 4.75$ GeV are used. The renormalization scales are set to the transverse masses $m_T = \sqrt{m_q^2 + p_{t,q\bar{q}}^2}$, where $p_{t,q\bar{q}}^2$ is the average of the squared transverse momenta of the quark and anti-quark. For beauty, the factorization scale μ_f is set to m_T while for charm $\mu_f = \sqrt{4(m_c^2 + p_{t,c\bar{c}}^2)}$. Here, $p_{tb\bar{b}}$ is the average of the transverse momenta of the two b quarks. In DIS, the scale $\sqrt{m_q^2 + Q^2}$ is used.

The theoretical uncertainties of the NLO calculation are usually estimated by variations of the renormalization and factorization scale parameters up and down by a factor of two and the c (b) mass between 1.3 and 1.7 (4.5 and 5.0) GeV. These variations, when combined, typically lead to a change in the cross section predictions of 30–35% for charm photoproduction and 20–30% for beauty photoproduction (FMNR). In DIS (HVQDIS) the uncertainties are typically between 10 and 20%.

The cross section variations when using different proton structure functions are less than 10% for most measurements. Further uncertainties (of order 10%) have been seen to arise from the implementation of muon decay spectra and fragmentation functions. These are usually taken from the spectra as implemented in the Monte Carlo simulations. The uncertainty due to variations of the fragmentation parameter ϵ by 25% is usually small ($\sim 3\%$).

It should be noted that the parameter choices and variations as described above are conventions which are mainly justified by the fact that the normalization of the cross sections and size

of the total systematic error obtained when following this procedure is plausible. A combined analysis using several data sets and measurements could be useful in order to determine the appropriate parameters more precisely, thus reducing the uncertainties due to the quark masses, the scales and the fragmentation functions and parameters for future predictions.

3.2.2 MC@NLO

Since recently the Monte Carlo generator program MC@NLO exists [130–132]. It provides a calculation of DGLAP evolution equations with NLO Matrix Elements which is matched with the generation of parton showers to describe higher orders which are not contained in the NLO calculations. It has been shown (see fig. 7) to successfully describe the beauty production measurements in $p\bar{p}$ collisions with data collected in Run-II at the Tevatron [133] but is yet to be adapted for the processes in ep collisions at HERA.
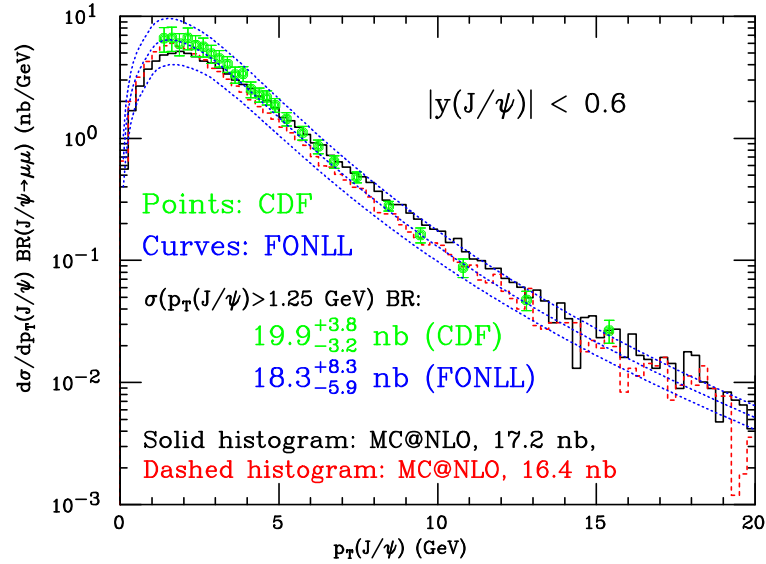

Figure 7: CDF J/ψ spectrum from B decays. Two MC@NLO predictions are shown as histograms (see [132] for details). The theory bands represent the FONLL prediction and systematic uncertainties [91].

4 The Experiments H1 and ZEUS at HERA

The electron proton storage ring HERA (fig. 8) at the DESY laboratory in Hamburg collides 27.5 GeV electrons or positrons with 920 GeV protons[2]. The storage ring has a circumference of $6.4\,\text{km}$ and consists of two separate accelerators. The beams are segmented into 180 colliding bunches each, providing a bunch crossing rate of 10 MHz. Four experiments are situated at HERA. The two collider experiments H1 and ZEUS have been in operation since 1992. In 1995 the HERMES experiment started data taking using the polarized electron beam on a fixed polarized gas target [134]. The HERA-B proton-proton fixed target experiment was operated between 1998 and 2003. HERA-B makes use of the proton beam halo using a wire target [135].
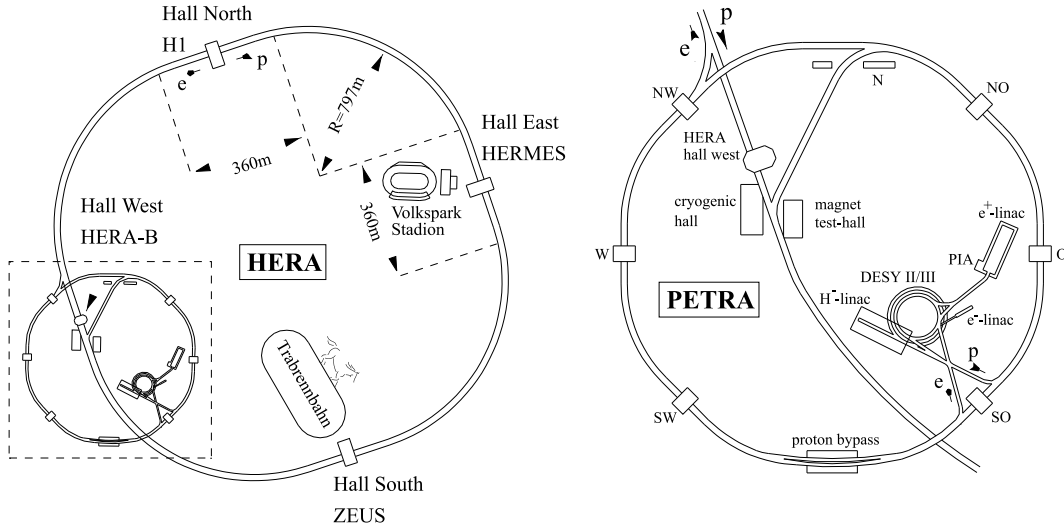

Figure 8: The HERA collider with the four experiments H1, ZEUS, HERMES and HERA–B on the left and its pre-accelerators on the right.

The H1 and ZEUS detectors are typical multi-purpose collider experiments. A schematic view of the ZEUS detector is shown in fig. 9. The physics programs comprise the full spectrum of QCD studies, measurements of the proton structure functions and exclusive hadronic final states, as well as electroweak physics and searches for new physics phenomena [136]. With an ep center-of-mass energy of 320 GeV the HERA collider experiments H1 and ZEUS are close to the present energy frontier for accelerator based experiments. Only the Tevatron experiments CDF and D0 [137, 138] have access to higher center-of-mass energies. Events in deep inelastic ep scattering have been measured down to values of x as low as $\sim 10^{-6}$ and up to values of Q^2 of $\sim 50,000\,\text{GeV}^2$. In QCD, measurements of exclusive final states comprise jet physics, heavy flavour production, processes in hard and soft diffraction and hadron spectroscopy.

In the years between 1992 and 2000 the collider experiments H1 and ZEUS collected an integrated luminosity of 100 pb^{-1} each. The bulk data were taken in the years 1996 through 2000. In the years 2001/2 a major luminosity upgrade of HERA was put in place accompanied by a number of upgrades of the H1 and ZEUS detectors, as described in section 7. The interaction points were equipped with new focusing magnets which allow for substantially increased

---

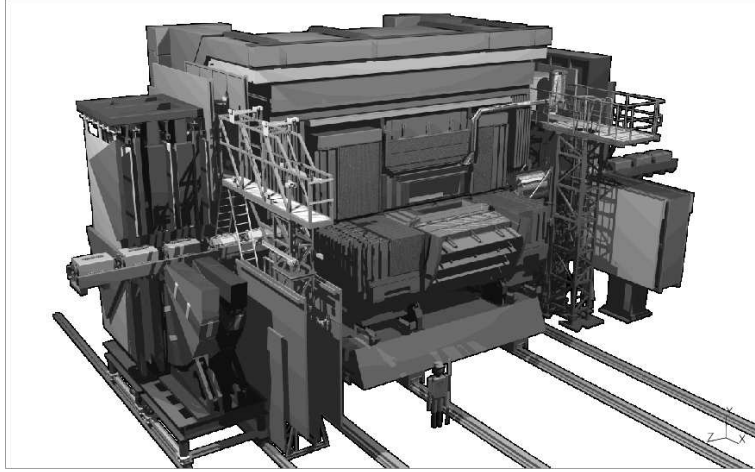[2]Until 1998 the proton energy was 820 GeV.

Figure 9: Schematic view of the ZEUS Detector.

specific luminosities. Since 2003/4 the HERA collider is running again and peak luminosities of larger than $4 \cdot 10^{31}$ cm^{-2} s^{-1} have been reached, to be compared with the design luminosity of $\sim 7 \cdot 10^{31}$ cm^{-2} s^{-1}. By the year 2007, an integrated luminosity of 500 pb^{-1}, useful for physics analyses, is expected to be produced for each of the two collider experiments.

The designs of the H1 and ZEUS detectors were chosen to be somewhat complementary, with emphasis on the reconstruction of the scattered electron in the case of H1 and on the precise calorimetric measurement of the hadronic final states in the case of ZEUS. Both experiments are capable of the triggering and reconstruction of events with heavy quark contents down to very low transverse momenta $p_t \gtrsim 1$ GeV. Charmonium is measured using the decays into leptons down to $p_t \sim 0$. A heavy quark candidate event in the H1 experiment is displayed in fig. 10.

In the following the experiments H1 and ZEUS are described[3], emphasizing those components that are most relevant for the triggering and reconstruction of heavy quark events, i.e. the tracking and vertexing detectors and the detectors used for lepton identification.

4.1 The H1 Experiment

The design of the 2800 ton H1 detector [139], schematically shown in fig. 10, emphasizes charged particle tracking in the central region as well as high calorimetric resolution for electromagnetic energy depositions.

The primary components of the H1 tracking system are two coaxial cylindrical jet–type drift chambers (CJC) covering the polar angle region between 15° and 165°. The two chambers consist of 30 (60) drift cells respectively with 24 (32) sense wires each strung parallel to the beam axis. The sense wires are read out at both ends, and the z-coordinate is measured by

---

[3]In this section, the detector configurations of the HERA-I running period are given. The HERA-II configurations are generally similar. Substantial upgrades to the HERA-I detector configurations are described in the context of the HERA-II physics program in section 7.
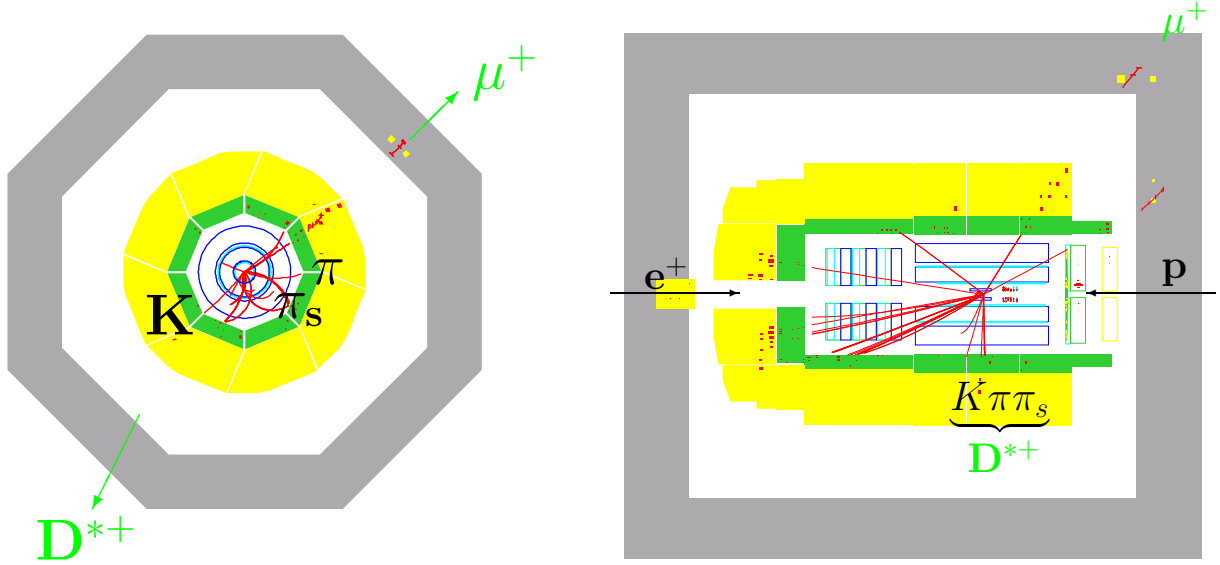
16

Figure 10: Display of a candidate for an event containing beauty quarks in the H1 Detector. The event is a candidate for the beauty production process process $ep \rightarrow eb\bar{b}X$ (as explained in section 6.3). One of the $\bar{b}$ quark decays into a positively charged muon which is detected as a track in the instrumented iron return yoke, the b quark forms a B hadron which decays into a D^{*+} meson. The D^{*+} meson candidate is reconstructed in the decay channel $D^{*+} \rightarrow D^0\pi^+ \rightarrow K^-\pi^+\pi^+$ from tracks measured in the inner tracking chambers.

charge division with a mean z-resolution of $\sigma_z = 55$ mm. The spatial resolution of the CJC in the $r\varphi$ plane is $\sigma_{r\varphi} = 130\,\mu$m. The momentum resolution in the plane transverse to the 1.2 Tesla solenoidal field is $\sigma(p_t)/p_t = 0.006\,p_t[\text{GeV}] \oplus 0.015$. The magnetic field is produced by a 5 m long superconducting solenoid of 5.8 m in diameter which encloses the calorimeter. Two further inner drift chambers and two multiwire proportional chambers (MWPC) serve to measure the longitudinal track coordinates and to provide trigger information.

A Central Silicon Track detector (CST) [140] is situated around the beam pipe, consisting of two 36 cm long concentric cylindrical layers of double-sided silicon strip detectors, at radii of 57.5 mm and 97 mm from the beam axis. The CST covers a pseudo-rapidity range of $30° < \theta < 150°$ for tracks passing through both layers. The double-sided silicon detectors provide resolutions of 12 μm in r-ϕ and 25 μm in z. Average hit efficiencies are 97% (92%) in r-ϕ (z). For a central track with CST r-ϕ hits in both layers, the transverse distance of closest approach dca of the track to the nominal vertex in x-y can be measured with a resolution of $\sigma_{dca} \approx$ 33 μm $\oplus$ 90 μm/p_t[GeV], where the first term represents the intrinsic resolution (including alignment uncertainties) and the second term is the contribution from multiple scattering in the beam pipe and the CST; p_t is the transverse momentum of the track.

The Forward Tracking Detectors cover a polar angular range between $5°$ and $30°$. The system consists of three supermodules composed of three planar drift chambers, a multiwire proportional chamber, a transition radiator and a radial drift chamber. The MWPCs serve for trigger purposes and complement the polar angular coverage of the central proportional chambers. The H1 main calorimeter employs a fine-grain liquid argon (LAr) sandwich structure in the barrel

17

and forward (proton-beam) region (with angular range from $4°$ to $155°$ in polar angle). In the backward region (with angular range from $155°$ to $177.5°$) a lead/scintillating–fiber calorimeter [141] provides an excellent energy resolution of $\sigma(E)/E = 0.07/\sqrt{E[\text{GeV}]} \oplus 0.01$, and a time resolution better than 1 ns. The electromagnetic section of the liquid argon calorimeter uses lead plates as absorber material. In the hadronic section (which provides a depth of ~ 5 nuclear interaction lengths) steel plates are used. In total there are 31,000 electromagnetic and 14,000 hadronic readout channels, segmented longitudinally and tranverse to the shower direction. The electromagnetic LAr calorimeter achieves an energy resolution of $\sigma(E)/E = 0.12/\sqrt{E[\text{GeV}]} \oplus 0.01$. The high degree of segmentation allows for a distinction between hadronic and electromagnetic energy depositions in the offline reconstruction, resulting in a hadronic energy resolution of $\sigma(E)/E = 0.55/\sqrt{E[\text{GeV}]} \oplus 0.01$.

Muons are identified as minimum ionizing particles in both the calorimeters and in the iron magnetic field return yoke surrounding the magnetic coil. The iron system is instrumented with 16 layers of limited–streamer tubes of 1 cm^2 cell size. Altogether the muon system consists of $\sim 100,000$ channels. Up to five out of 16 layers are used for triggering. In order to provide a two-dimensional track measurement five of the 16 layers are equipped in addition with strip electrodes glued perpendicular to the sense wire direction.

The H1 trigger and readout system consists of four levels of hardware and software filtering. Three of these layers, the first (L1) and second (L2) level trigger and the asynchronous online filtering (L4) - were operated in HERA-I. The third level is prepared to be used by the H1 Fast Track Trigger system (described in section 7.1.5). The L1 system is phase-locked to the HERA accelerator clock signal of 10.4 MHz and provides a trigger decision for each bunch crossing after 2.3 μs. The subdetector systems feed data into front-end pipelines and generate fast information (trigger elements) about general properties of the event. The trigger elements are sent to the central trigger logic which makes decisions on the basis of 128 logical combinations of these trigger elements. The L1 decisions are then validated by the second level trigger allowing 20 μs for the decision. The L2 trigger system implements conditions on topological properties of the events. Neural nets are used to combine information from several detector components. The subdetector data are read out asynchronously by the central data acquisition electronics and fed into the software filter (L4). The reading of events from the front-end buffers takes about 1.2 ms, during which no new events can be recorded. This dead-time is inherent to the architecture of the read-out electronics. At a typical L4-input rate of 50 Hz the dead-time is about $\sim 8\%$. In the L4 software filter the events are fully reconstructed and classified in different physics categories and monitoring channels. The reconstruction of a physics event typically requires 200 ms. Events classified as physics as well as monitor events are permanently stored at a typical rate of 5 to 10 events per second.

4.2 The ZEUS Experiment

The ZEUS detector [142,143] makes use of a 700–ton compensating uranium sampling calorimeter, with equal sampling fractions for electromagnetic and hadronic shower components. The calorimeter is made up of layers of 2.6 mm SCSN–38 scintillator and 3.3 mm stainless–steel–clad depleted-uranium plates. One layer corresponds to 1.0 radiation length (X_0) and 0.04 interaction lengths. This choice of layer thicknesses results in a sampling fraction of 4%

for electromagnetic and hadronic shower components, and hence compensation, and 7% for minimum–ionizing particles. The compensation results in a very good hadronic energy resolution of $\sigma(E)/E = 0.35/\sqrt{E[\text{GeV}]} \oplus 0.02$. The resolution for electromagnetic showers is $\sigma(E)/E = 0.18/\sqrt{E[\text{GeV}]} \oplus 0.01$.

The ZEUS solenoidal coil of diameter 1.9 m and length 2.6 m provides a 1.43 T magnetic field for the charged–particle tracking volume. The tracking system consists of a central wire chamber covering the polar angular region from $15°$ to $164°$, a forward planar tracking detector from $8°$ to $28°$ and a second planar tracking chamber in the backward direction, covering the region from $158°$ to $170°$. The momentum resolution attained is $\sigma(p_t)/p_t = 0.005\, p_t \oplus 0.015$ and a track is extrapolated to the calorimeter face with a transverse resolution of about 3 mm. Ionization measurements from the central tracking chamber also serve to identify electron–positron pairs from J/ψ decays. The muon system is constructed of limited streamer tubes inside and outside of the magnetic return yoke, covering the region in polar angle from $10°$ to $171°$. Hits in the inner chambers provide muon triggers for J/ψ decays.

The ZEUS trigger system consists of three layers. The first level trigger accepts events at a rate of about 300 Hz. The read out data are stored in digital or analog pipelines with a depth of 4.4μs until a global first level trigger decision is received. At the second level commercially available microprocessors analyze the digitized data of the components. The second level trigger processor functions as an asynchronous pipeline, i.e. a series of parallel processors. Beam gas background is rejected on the basis of calorimeter timing information which is available at this stage. The second level trigger is able to perform iterative calculations on large fractions of the full event information which are not possible in the pipelined structure of the first level trigger. These features enable the second level trigger to achieve a reduction of the first level trigger rate from ~ 300 Hz to ~ 100 Hz. The third level trigger provides a software filter in which the event rate is further reduced to the level of 15 Hz.

5 Experimental Methods

Heavy quark physics requires a precise experimental determination of the fraction of produced events containing heavy quarks. A number of methods has been established and those most widely used at the HERA experiments are discussed below. The identification algorithms are generally similar among the different high energy physics experiments in that characteristic signatures of the decay processes of heavy hadrons are exploited. Experimentally, the different techniques are somewhat complementary and range from the full reconstruction of the invariant mass using all decay particles to the measurement of the lifetime distribution of the hadrons by means of displaced vertices or track parameters. The methods, which are described in detail in the following, are often combined to enhance the significance of the heavy quark signal separation from the light-quark background.

5.1 Resonance Reconstruction

In most analyses signals for charm quarks have been obtained by full reconstruction of the decay particles of the charmed hadrons into which the quarks fragment. From the decay particles the invariant mass is reconstructed, such that the number of signal events can be determined from the resonance spectrum, above a non-resonant combinatorial background. The reconstruction of the invariant mass works particularly well in hadronic decays in which all final state particles are measured as charged particles in the tracking detectors. Calorimeter energy deposits are sometimes used for decay channels containing π^0 or γ.

The most widely used method to identify events containing charm is the reconstruction of events in the so-called 'golden decay' channel, in which the invariant mass of the $D^{*\pm}$ meson is reconstructed in the decay $D^{*\pm} \to D^0\pi^\pm \to K^\mp\pi^\pm\pi^\pm$. In fig. 11 the difference ΔM between the measured masses of the $K\pi\pi$ system and of the D^0 meson decaying into $K\pi$ is shown. The number of signal events and the amount of non-resonant background in the mass window is usually determined by a fit to the signal and the side bands. The width of the ΔM peak is governed by the experimental resolution of the pion track from the D^* decay, as resolution effects from the measurement of the two D^0 decay particles largely cancel in the subtraction. The ΔM distribution is therefore the preferred way to determine the number of D^* mesons in the sample.

The advantage of the full resonance reconstruction method is that all details about the heavy quark resonance and decay kinematics are known and the number of events can be determined precisely. The disadvantage comes from small branching ratios, $BR(D^{*\pm} \to D^0\pi^\pm \to K^\mp\pi^\pm\pi^\pm) \simeq 2.6\%$ [144] and limited detector capabilities such as finite detector acceptances and/or poor resolution. At small Q^2 the detector acceptance constrains measurements in which samples of fully reconstructed D^* mesons are used to about one third of the total phase space for charm production [5]. Limited detector resolution leads to the need for wide mass windows or large combinatorial background. Bad resolution is a particular issue for the identification and measurement of neutral particles at low energies as neither experiment, H1 nor ZEUS, have been designed for this purpose.

Figure 11: D^* signal from ZEUS in the decay channel $D^{*\pm} \to (D^0 \to K^{\mp}\pi^{\pm})\pi^{\pm}$. Events are selected in which the invariant mass of the $K\pi$ system is consistent with the mass of the D^0 (taken from [19]).

Figure 12: Specific ionization energy loss relative to that of a minimally ionizing particle, plotted against momentum, for a sample of D^* meson candidate events which also contain a proton candidate (taken from [51]). The curves indicate parameterizations of the most probable responses of the H1 drift chambers for pions, kaons and protons, respectively.

5.2 Particle Identification

Particle identification is often used in order to enhance the contribution from heavy hadrons and/or to reduce the combinatorial backgrounds. For the reconstruction of invariant mass spectra it is useful to identify charged pions, kaons and protons, such that particles that are clearly identified as not coming from the heavy hadron decay can be removed from the list of par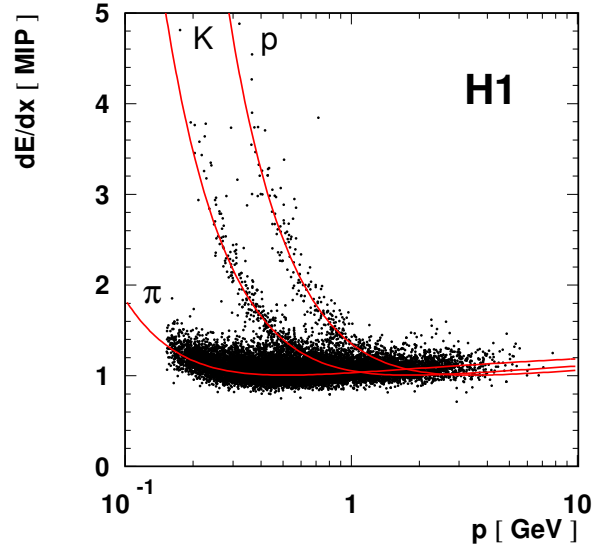ticles used for the mass reconstruction. Although not optimized for this purpose, the central drift chambers can be used to determine the specific energy loss dE/dx for a given particle. This energy loss depends on the velocity of the particle. The measurement of the summed charge of the hits of a drift chamber track, together with the measurement of the particle momentum thus allows to discriminate between π, K and p (see fig. 12). The H1 and ZEUS drift chambers provide a relative uncertainty for the charge measurement of typically 8%, leading to a K-p separation of $\sim 1\sigma$ at 2 GeV.

The identification of leptons originating from semi-leptonic decays of heavy hadrons is a very useful means for the selection of heavy quark event candidates. Furthermore, in charmonium decays into leptons, the lepton identification allows to remove the largest part of the combinatorial background for the reconstruction of the charmonium invariant mass.

The μ-identification is particularly simple as the instrumented iron return yokes are available for the reconstruction of muon tracks. The HERA experiments have full acceptance for the muons to be measured in the instrumented iron at transverse energies of 2.0 GeV and above. The muon identification can be enhanced by reconstruction of isolated energy deposits in calorimeter cells close to the extrapolated muon track, which are consistent with the amount of energy deposited by a minimally ionizing particle. The longitudinal segmentation of the H1 and ZEUS calorimeters allows to reconstruct quantities, such as the length of the track inside the calorimeter or the energy deposited in a narrow cone along the projected muon track, which provide for a muon fake probability of 1-2% at muon momenta of 1-2 GeV [145].

The separation between π and e in the calorimeter is important to suppress fake background in samples of semi-electronic decays. A detailed study of electron identification in the calorimeter in a dense hadronic environment has been given e.g. in [146].

5.3 Track-Cluster Matching

The energy of particles can be measured using the tracks (for charged particles) and the calorimeter (for all particles). Optimal experimental resolution for particle momenta and kinematic variables is obtained by combination of the information from the tracking detectors and the calorimeter, using a track-cluster matching algorithm.

Tracks measured in the tracking chambers are associated with energy depositions in the calorimeters in a way that avoids double-counting (of charged particle energies) and/or the omission of energy contributions (from neutral particles). In the usual approach well measured tracks are used for the measurement of the charged particles while neutral particles and particles at large energy scales ($E \gtrsim 20$ GeV) where the calorimeter resolution is superior to that of tracks, are measured using the calorimeter. For non-compensating calorimeters (such as the LAr-calorimeter of the H1 experiment) the treatment of calorimeter energy deposits requires the

classification as hadronic or electromagnetic shower in order to define the energy scale at which the calorimeter signals are evaluated and combined with the tracks. The classification, often called 'software compensation', is based on the compactness of the shower in the calorimeter. Fluctuations of the shower development and limited cell granularity make the classification ambiguous to a certain extent.

In the matching algorithm the tracks are extrapolated to the calorimeter and energy depositions behind the tracks in the calorimeter are masked out to avoid double-counting. The masking leads to the loss of neutral particles which are close to the charged particles, resulting in a systematically reduced experimental response by up to 10%. To minimize these losses matching and distance parameters are tuned in a detector specific way, taking resolutions, granularities and average particle multiplicities in physics processes into account. Remaining effects are generally well described by the Monte Carlo simulations and can in this way be removed from the results of the measurements.

The combined track-cluster objects are then used to calculate global kinematic event variables and to reconstruct jets and other components of the hadronic final state.

5.4 Jet Reconstruction

In recent analyses jets are usually reconstructed using the inclusive k_t algorithm [147, 148]. Different schemes are available [149] which define the merging of two objects into a single object based on distance parameters, and the calculation of the 4-vector of the resulting jet. The distance parameters d_{kl} are usually defined as momentum weighted distances in the η-ϕ plane, $d_{kl} = \min(p_{t,k}^2, p_{t,l}^2)((\Delta\eta)^2 + (\Delta\phi)^2)$. In the E recombination scheme the 4 vectors of the input objects are added to obtain the 4-vector of the massive jet. In the p_t recombination scheme only the 3-vector components of the input objects are taken into account and the obtained jets are made massless by setting their energy equal to the magnitude of their 3-momentum.

There are no theoretical arguments to prefer one or the other recombination scheme. For final states with beauty quarks the results of the different recombination schemes have been seen to give the same quantitative results to better than 10%.

5.5 Lifetime Tag

Vertex detectors can be used to detect vertices displaced from the primary interaction point. For charm mesons with lifetimes between 0.4 and 1 ps the typical spatial separation between their production vertex and the decay vertex is given by their $c\tau$ of 120 to 315 μm.

In a recent analysis at HERA, a complete reconstruction of charmed mesons was performed in combination with a lifetime tag to reduce the combinatorial backgrounds [6]. A sketch of the reconstruction procedure for the reconstruction of the long-lived $D^\pm$ meson candidates is shown in fig. 13. The main difficulty in the 3-body decays of the $D^\pm$ into $K^\mp\pi^\pm\pi^\pm$ is the combinatorial background which is large due to the large number of combinations of tracks that can wrongly be assigned to one of the decay particles. The signal-to-background ratio can drastically be improved by use of a lifetime tag in which it is required that the tracks originate
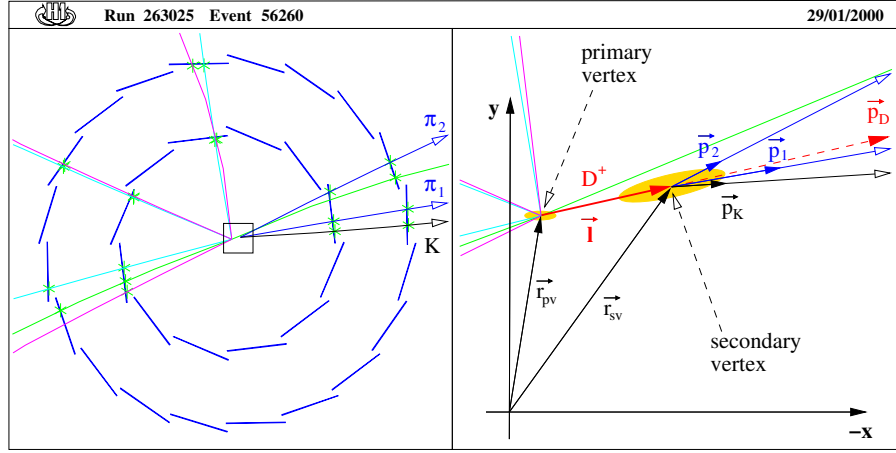
Figure 13: Reconstruction of a D^+ meson candidate by reconstruction the vertex from the decay particles $K^{\mp}\pi^{\pm}\pi^{\pm}$. The displacement of the secondary vertex is used to enhance the fraction of signal events in the sample (see fig. 14).
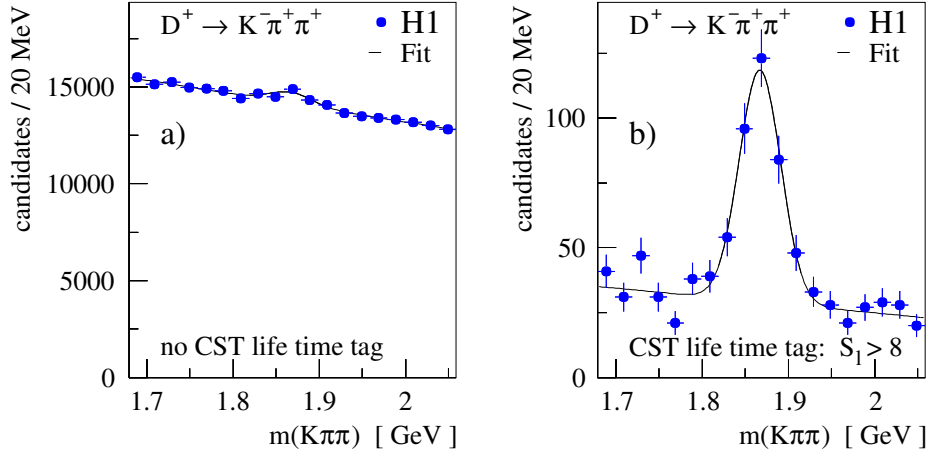

Figure 14: Invariant mass distribution $m(K\pi\pi)$ for $D^{\pm} \rightarrow K^{\mp}\pi^{\pm}\pi^{\pm}$ decay candidates, a) before and b) after a cut on the decay length significance $S_l > 8$ [6].

from a common displaced vertex. The vertex displacement is measured in the r-ϕ plane. In fig. 14 the mass spectrum is shown without and with the cut $S_l > 8$ on the vertex displacement. Here, S_l is the significance of the displacement, i.e. the distance between the primary and secondary vertices divided by the uncertainty of the distance measurement.

5.5.1 Single Impact Parameter Method

In many analyses, a complete reconstruction of the heavy hadron invariant mass and/or displaced vertex is not possible – nor is it necessary, as the partial reconstruction and identification of event characteristics that signify the presence of heavy quarks, e.g. the presence of a leading lepton or decay lifetime distributions, is often sufficient for the measurement of heavy quark production cross sections and event distributions. The main advantage of those measurements

$\alpha < \pi/2 \ \longrightarrow \ \delta = +|\delta|$ $\alpha > \pi/2 \ \longrightarrow \ \delta = -|\delta|$
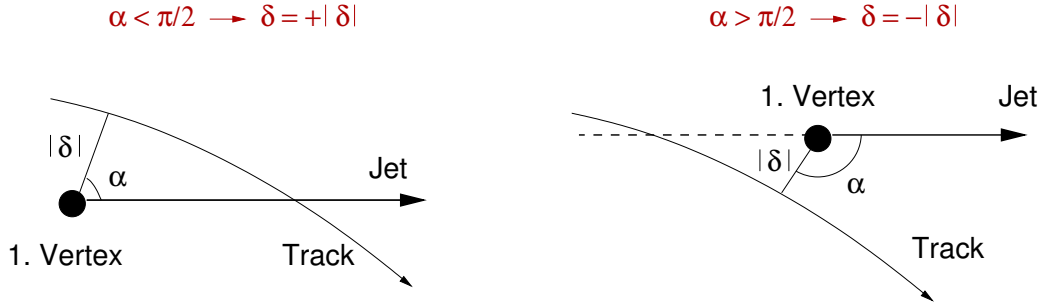
Figure 15: Sketch of the impact parameter reconstruction. The sign of the impact parameter is based on the angle between the jet and the line between the primary vertex and the point of closest approach of the track. The two cases for a) a positive sign and b) a negative sign are shown.

in which heavy hadrons are only partially reconstructed, is that they can be performed on samples of much larger statistics. For example, in more recent measurements, the measured lifetime distributions have been used to determine the fraction of events containing charm and beauty (see section 5.5.2). For these measurements it is sufficient to measure at least one charged decay particle track in the silicon detectors from which the lifetime information is extracted.

The reconstruction of secondary detached vertices is experimentally demanding. An unambiguous association of all tracks to the secondary vertex can only be achieved if the spatial precision of the track measurement is of the same order as the distance between the primary and the secondary vertex, i.e. $\mathcal{O}(100\mu m)$. Harsh track selection cuts are necessary to ensure that the tracks fulfill this criterion, leading to a significant loss of statistics. For quantitative analyses of heavy quark production rates, e.g. cross section measurements, the loss of signal events due to lifetime-based selection cuts needs to be precisely estimated. This would require to precisely describe the track reconstruction efficiencies and the spatial resolutions of all tracks used for the reconstruction of the heavy hadron.

In recent analyses of the H1 Collaboration, a simpler method has been successfully used, which is based on the measurement of the impact parameters of one or several tracks, and thus allows to maintain a larger number of signal event candidates than the secondary vertex method. In the impact parameter method, only a subset of the tracks originating from the displaced vertex is used to perform a lifetime tag. The impact parameter of a track is defined as the transverse distance of closest approach (DCA) of the track to the primary vertex point. The signed impact parameter δ (fig. 15) of the charged particle track with respect to the primary event vertex reflects the lifetime of the particle from which the charged particle decays. The signed impact parameter is defined by reference to the direction of the reconstructed particle or the jet to which the track is associated. Usually, the direction is reconstructed using a jet algorithm (see above). The signed impact parameter of a track is defined as positive if the angle between the jet direction and the line joining the primary vertex to the point of DCA is less than $90°$, and it is defined as negative otherwise (see fig. 15). The sign allows to statistically disentangle detector resolution effects and effects from the decay lifetime of the heavy hadron. Tracks from the decays of long lived particles will have positive impact parameters, if resolution effects are neglected. Tracks produced at the primary vertex result in a symmetric distribution around 0, i.e. negative impact
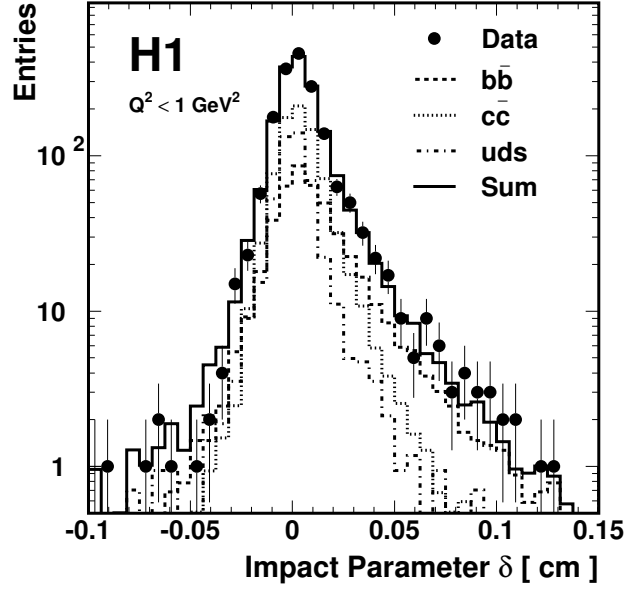
25

Figure 16: Distribution of the signed impact parameter of the muon track for a sample of photoproduction events with two jets and an identified muon. The solid line shows the distribution of the PYTHIA Monte Carlo simulation after a fit of the normalization of light quark, charm and beauty quark events [44].

parameters predominantly result from detector resolution effects.

Figure 16 shows the distribution of the impact parameter of an identified muon track for a sample of photoproduction events with two or more jets and a muon [44]. In this sample the contribution from heavy quarks is enhanced by the requirement that a muon with transverse momentum $p_t > 2.5$ GeV be present. The lifetime effects are apparent in the asymmetric distributions of the estimated charm and beauty contributions. The normalization of the contributions has been determined by a fit to the data. Details of this analysis are described in section 6.2.1.

5.5.2 Negative Subtraction Method

From the signed impact parameter a signed significance can be derived by dividing the measured signed impact parameter by the estimate of its resolution. Well measured tracks with large impact parameters lead to large values for the significance while badly measured tracks with large resolution remain in the core of the distribution. In fig. 17 the significance distributions of tracks is shown for a sample of events at large photon virtualities Q^2 [43]. A detailed description of the analysis based on such signatures is given in section 6.2.2. The selected tracks are required to have transverse momenta of larger than 500 MeV. No lepton or jet criteria are explicity imposed. Consequently, the relative contribution from charm and beauty events is significantly smaller than in fig. 16.

Only those tracks with an impact parameter of less than 0.1 cm enter the significance distributions S_1 and S_2 (fig. 17a and c). This selection suppresses contributions from decays of long lived particles containing strangeness and allows to achieve a reasonable discrimination of
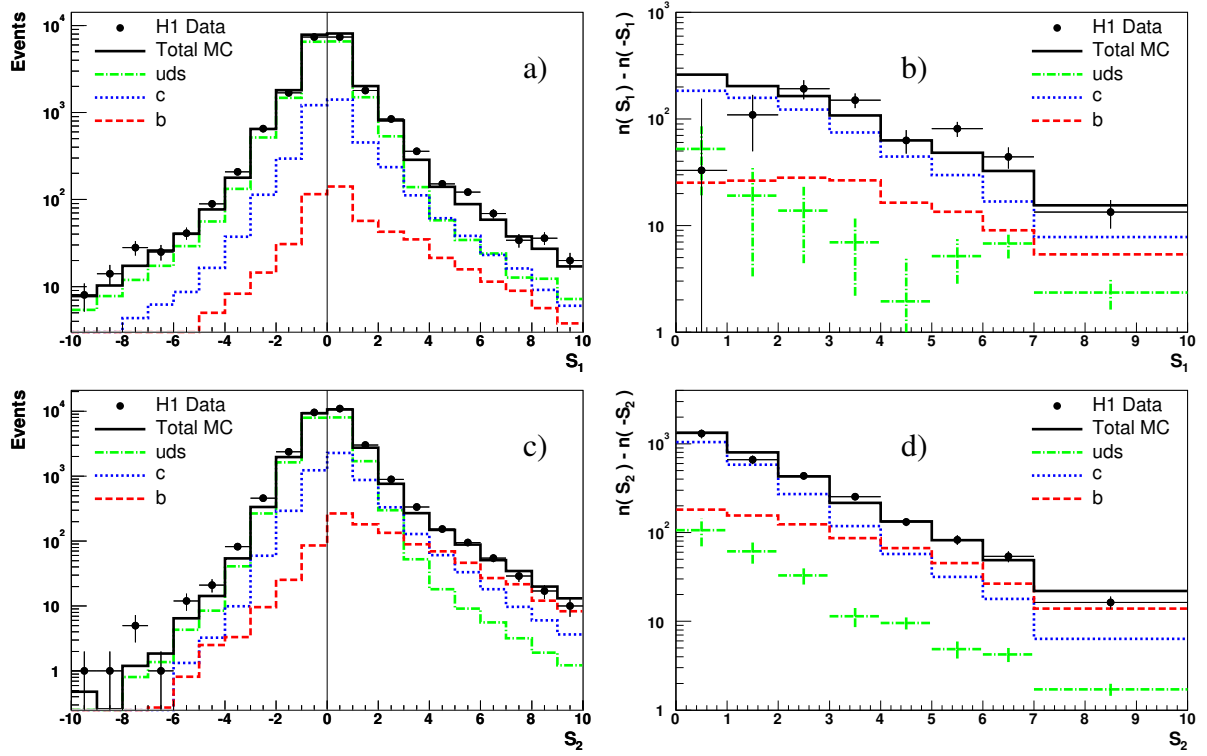
26

Figure 17: Significance distributions S_1 (a,b) and S_2 (c,d) before subtraction (a,c) and after subtraction (b,d) [43] (see text).

the charm and beauty components. Studies show that the significance distribution from strange particle decays is almost symmetric at small impact parameters. The distribution S_1 (fig. 17a) denotes the significance of the track with the highest significance in the event. Only those events are used in which there is only one selected track. The significance S_2 (fig. 17c) is defined for events with two or more selected tracks and where the track has the second highest significance of all selected tracks. In addition, it is required that the significance S_2 has the same sign as S_1 in the same event. The distributions are dominated by light quark events and exhibit large tails to both negative and positive values of significance with only a small asymmetry due to the long lived charm and beauty decays.

In the 'negative subtraction method' the negative bins in the significance distributions are mirrored at $S = 0$ and subtracted from the positive. This way, effects that lead to significance distributions which are symmetric around zero are removed. In particular, the uncertainties due to the impact parameter resolution and the light quark normalization are substantially reduced.

The subtracted distributions are shown in figs. 17b and d. The contributions from charm and beauty are determined by a fit which is performed simultaneously to both the subtracted S_1 and S_2 distributions and the total number of inclusive events before track selection. The shapes for the c, b and uds distributions are taken from Monte Carlo simulations and their normalization is fitted to the data. Only the statistical errors of the data and Monte Carlo simulation are considered in the fit. The Monte Carlo c, b and uds contributions in each x–Q^2 interval are allowed to be scaled by factors P_c, P_b and P_l, respectively. The fit to the S_1 and S_2 distributions mainly constrains P_c and P_b, whereas the overall normalization constrains P_l. The c and b quark fractions are distinguished in the fit by their different shapes in the S_1 and S_2 distributions.
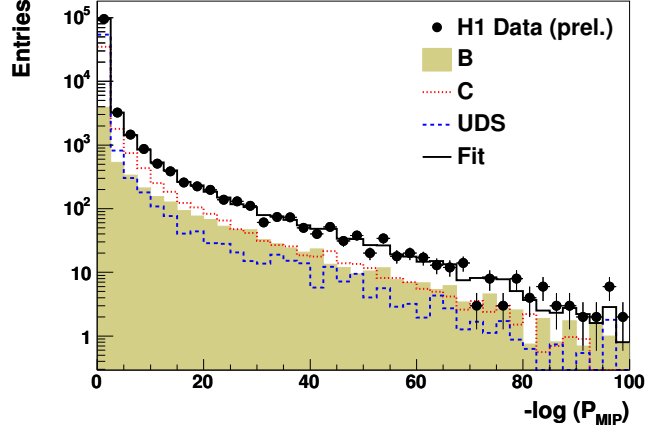
27

Figure 18: Distribution of the negative logarithm of the multi impact parameter probability. The decomposition of the simulation into b (shaded histogram), c (dotted line), uds (dashed line) is taken from the fit [45] (see text).

The precise simulation of the simulated shapes is crucial for inclusive lifetime tag analyses. In particular, the size of the b-fraction obtained from the fits is directly dependent on the decomposition of the simulated charm sample into events with short-lived and with long-lived charmed hadrons (e.g. $D^{\pm}$), since the long-lived charmed hadrons have lifetime distributions and track multiplicities which are similar to those of beauty hadrons. In existing H1 analyses charm fragmentation universality is assumed and the fragmentation fractions as described in [159] are used which are based on measurements at LEP, CLEO and ARGUS. Measurements of charm fragmentation at HERA are discussed in detail in section 6.1.6.

Results consistent with the negative subtraction method have been found using alternative methods, such as the multi-impact parameter method (MIP) and the method of deterministic annealing.

5.5.3 Multi-Impact Parameter Method

In this method, the impact parameters of all well measured, i.e. selected, tracks in a given jet are used to form a probability that the tracks come from the primary interaction point and not from the decay of a long lived particle. The quantity

$$P(S_i) = \frac{1}{\sqrt{2\pi}} \int_{S_i^2}^{\infty} e^{-t^2} dt,$$

can be interpreted as the probability that a track originates from the primary vertex. The probabilities for tracks with negative significances are set to unity. A multi impact parameter (MIP) probability P_{MIP} is then constructed by combining the probabilities of the N selected tracks within each jet:

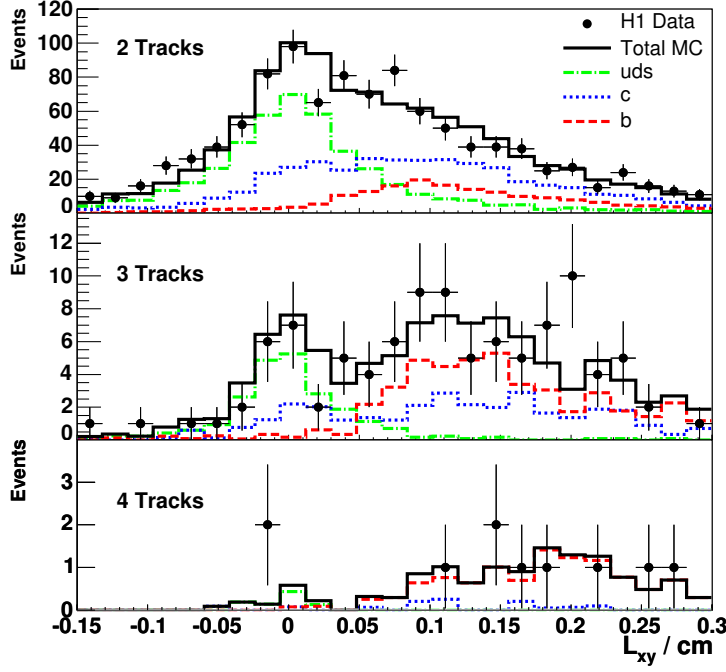$$P_{MIP} = \Pi \sum_{j=0}^{N-1} (-\ln \Pi)^j / j!,$$

Figure 19: The transverse distance between the primary and secondary vertex (L_{xy}) for events with two, three and four tracks associated with the secondary vertex. Superimposed on the data points are c, b and light quark contributions that have been scaled by the results of the fit to the distributions S_1 and S_2 using the negative subtraction method as described in section 5.5.2 [43].

where j runs over all selected tracks and

$$\Pi = \prod_{i=1}^{N} P(S_i).$$

The distribution of the negative logarithm $-\log(P_{MIP})$ for both jets is shown in fig. 18. The contributions from events containing b, c and uds quarks are determined by a fit [150,151] to the $-\log(P_{MIP})$ distribution, using the Monte Carlo expectations for the shapes of each of these quark flavours.

5.5.4 Deterministic Annealing

Another method to separate the quark flavours is based on the explicit reconstruction of decay vertices in the transverse plane. In the method of deterministic annealing [152], there is no definite assignment of tracks to vertices, but each track is assigned a weight with a range 0 to 1 for each vertex candidate, using the weight function of [153]. The larger the distance of the track to a vertex candidate, the smaller the weight. A simultaneous fit to a primary and a secondary vertex is made, with all tracks of the event considered for the primary vertex, whereas only tracks associated to the jet axis contribute to the secondary vertex. The vertex configuration that minimizes the global fit χ^2 is found iteratively.

In fig. 19 the decay length distributions are shown for events at large Q^2 with secondary vertices made up of two, three and four tracks, respectively. The decomposition into uds, c
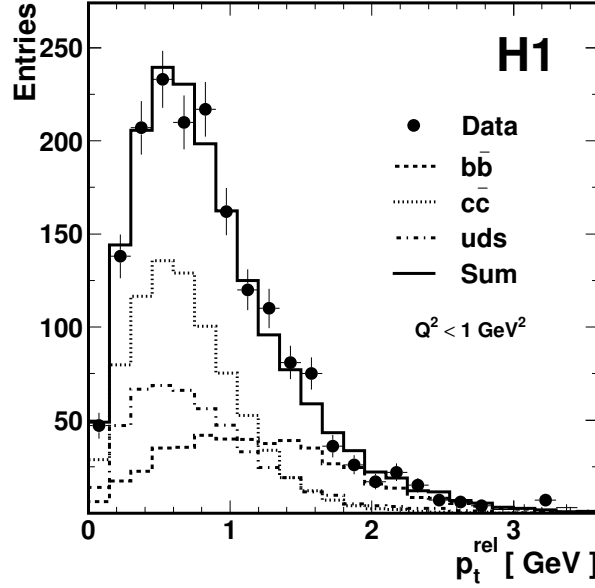
Figure 20: Distribution of the transverse momentum of the decay muon track candidate for a sample of photoproduction events with two jets and an identified muon. The solid line shows the distribution of the PYTHIA Monte Carlo simulation after a fit of the normalization of light quark (dash-dotted), charm quark (dotted) and beauty quark (dashed) events (see text).

and b is indicated using the results from the fit of the negative subtraction method as described above in section 5.5.2. The fig. 19 shows that the two methods give consistent results.

5.6 Relative Transverse Momentum Distribution p_t^{rel}

Events with heavy quarks are often identified using semi-leptonic decays of heavy hadrons. In these events the decay lepton is typically one of the leading particles in the event. While a fraction of the decay particles, e.g. the neutrino escape detection such that the mass of the heavy hadrons can not precisely be measured, it is nevertheless possible to reconstruct distributions which reflect the mass of the heavy hadron. These distributions are significantly different for charm and for beauty and therefore allow the determination of the relative contributions from charm and from beauty in a given event sample. The observable p_t^{rel}, i.e. the transverse momentum of the decay lepton relative to the direction of the parent quark, as estimated by the jet axis, provides a clear signature for beauty. Due to their larger mass, events with decays of B-hadrons populate higher values of p_t^{rel} as shown in fig. 20. The transverse momentum p_t^{rel} of the muon with respect to the axis of the associated jet exhibits a much harder spectrum for muons from b decays than for the other sources. At HERA, several analyses of beauty production have made use of the p_t^{rel} distribution and are described in section 6.2.1.

5.7 Triggering

Like most modern colliders, HERA produces a large total interaction rate which exceeds the readout rate and data storage capabilities of the H1 and ZEUS detectors and necessitates the use

of a sophisticated trigger system to select the physics events of interest. The trigger systems, as described in section 4 are complex multi-channel and multi-layer trigger and filter systems, which are optimized to maximize the statistics of selected physics processes, while suppressing beam backgrounds and downscaling the high-rate inclusive ep-scattering processes with no particular final state signatures.

The majority of heavy quark events is produced in the kinematic region of small transverse momenta p_t and small photon virtualities Q^2. This kinematic region is of particular interest as the various scale variables Q^2, p_t and m_c or m_b are of small and/or similar size. The total cross section in this region is dominated by processes with light quarks. Experimentally, particle identification is difficult and beam backgrounds are abundant. Triggering events with heavy quarks is particularly challenging as the effective rate of events with identifiable final state signatures is suppressed by the relatively small heavy quark production cross sections, the subsequent branching ratios, and the experimental acceptance limitations.

Typical trigger conditions used to collect events with heavy quarks implement a number of conditions in order to achieve reasonable purity of the triggered data samples and acceptably low rates. The efficiencies for heavy flavour triggers strongly depend on the physics channel (i.e. event selection) and range from $\sim 50\%$ for low-multiplicity events (e.g. J/ψ) in photoproduction to $\sim 90\%$ in electroproduction.

In both experiments H1 and ZEUS, triggering relies heavily on the evaluation of information from the tracking and calorimeter devices. The ZEUS trigger algorithms are more calorimeter–based, exploiting the excellent time resolution of the calorimeter, while that of H1 emphasizes tracking algorithms for reconstruction of the interaction vertex. Several detector components are used for the suppression of backgrounds from cosmic rays or beam gas interactions and for the identification of events with particular final states:

- The fast calorimeters (those with time resolution ~ 1 ns) are used to select ep events based on the arrival time of the scattered electron signal (H1) or all final state particles (ZEUS). Out-of-time backgrounds are further suppressed by veto-conditions using coincidences of signals in scintillator counters situated along the beam pipe. At ZEUS, the shaping, sampling, and pipelining algorithms permit the reconstruction of shower times with respect to the bunch crossings with a resolution of better than 1 ns. The timing information provides essential rejection against upstream beam–gas interactions.

- The H1 first level track trigger makes use of proportional chambers and drift chambers to determine the number of tracks, the event vertex position and the time. The central proportional chambers are used for fast reconstruction of the position of the interaction vertex in z and of the time of the interaction. The main purpose of this trigger is the suppression of proton beam backgrounds which produce tracks from vertices outside the interaction region. Furthermore, the trigger is used to estimate the event multiplicities. The trigger information is based on combinations of pad signals of the proportional chambers from which track directions are inferred using look-up tables. 16 histograms (one for each ϕ sector) containing the z-positions of the tracks extrapolated to the beam axis are combined in a z-vertex histogram which is used to determine the position of the vertex in z. The z-vertex trigger provides trigger elements to the L1 system, encoding significances and multiplicities of the vertex information, and more detailed information to

31

the L2 system. The H1 drift chamber trigger finds charged tracks in the r-ϕ projection. Drift time patterns from digitized hits in several layers (with wires parallel to the beam axis) are compared to predefined masks to determine kinematic properties of the tracks. The charge of the tracks can be measured and several transverse momentum thresholds, configurable in value, are used to classify tracks and to count track multiplicities. The system is optimized for the measurement of tracks from the interaction region and thus suppresses backgrounds due to beam-wall interactions or cosmic ray particles.

At ZEUS, the drift chamber trigger alone determines the number of tracks and whether they originate from the interaction region. This is done by applying lookup tables to two dimensional projections of the r and z coordinates of the hits in the central and forward track detectors. The rate reduction is obtained by the rejection of beam backgrounds and the downscaling of inclusive electron-proton scattering events with no particular final state signature for events with $Q^2 < 20\,\mathrm{GeV}^2$.

- The muon triggers use signals from the inner drift chambers and signals in the instrumented iron of the central muon detector. The H1 muon detector trigger is segmented into several modules. Coincidence of hits in several layers of the same module lead to a positive trigger signal from the muon systems. At ZEUS a muon track candidate in the central drift chamber with one or more hits in the muon chambers can be validated by energy in the calorimeter above a threshold of 460 MeV.

6 Experimental Results from HERA-I

In this section an overview of the results and measurements obtained with HERA-I data is given. In general, due to acceptance limitations of the experimental apparatus, the measurements are performed in restricted kinematic regions, which differ between different analyses, depending on the analysis technique and data sample. The tables 1, 2, 3 give an overview of the measurements of charm and beauty processes at HERA.

In order to allow for comparisons of measurements with results from other experiments or with theory predictions most analyses perform extrapolations of their data into unmeasured regions. The size of the corrections are often as small as a few percent but can reach a factor of order 10 in rare cases. In analyses using D^*-mesons the momentum and angular distributions of the decay particles ($K\pi\pi$) are usually assumed to be known and are extrapolated, such that the quoted cross sections are independent of the detector-specific cuts on the decay particles. These corrections are typically of order 25% reaching up to 50% at small values of $p_t(D^*)$. In analyses with jets, detector effects are removed by correcting the measured distributions to the hadron-level. Depending on the analysis the hadron-level may be differently defined, e.g. using the heavy hadrons before before or after the decay and including or excluding neutrinos. In some analyses, the results are extrapolated to a larger phase space using model assumptions (as taken from next-to-leading order (NLO) calculations or LO+PS Monte Carlo models) of the angular and momentum spectra of the particles and jets. In these cases the extrapolation factors can become fairly large leading to corrections of the cross sections of up to a factor of 5. The uncertainties arising from these extrapolations are therefore often difficult to determine and the extrapolated results should be treated with caution.

6.1 Open Charm Production

Charm production has been measured in a number of analyses, the first observations at HERA dating back to the year 1995 [2, 11]. Since then, with increasing statistics and continuously upgraded detectors the measurements have become increasingly precise and detailed in their scope. Inclusive charm production has been measured in both photoproduction [2, 7, 12, 19] and electroproduction [3–5, 8, 13, 15, 16, 43]. Reconstructed D^* mesons have also been used for measurements of open charm in diffraction [55–58], a process which is not addressed in this report.

6.1.1 Photoproduction of Charm

Recent measurements of inclusive photoproduction of D^* mesons were performed by H1 [7] and by ZEUS [19] using the decay channel $D^* \to D^0\pi_s$ with $D^0 \to K^-\pi^+(+c.c.)$. The D^* signal used for the ZEUS analysis is shown in fig. 11 in section 5. In fig. 21 the ZEUS data are compared with predictions from two next-to-leading order calculations, namely the fixed order massive calculation FMNR [80] and the matched calculation FONLL [92] (sections 2.1 and 3.2.1). For the calculations the scale parameters are chosen to be $\mu_R = \mu_F = m_T = \sqrt{m_c^2 + p_{c,T}^2}$, where μ_R is the renormalization scale parameter and μ_F is the factorization scale

	Analysis	Data	Kinematic Region				
			Q^2 [GeV^2]	y	p_t^D [GeV]	η^D	Other cuts
[2]	D^* in γp	1994	< 0.01		> 2.5	$-1.5...1.0$	$159 < W_{\gamma p} < 242$ GeV
			< 4		> 2.5	$-1.5...1.0$	$95 < W_{\gamma p} < 268$ GeV
[3]	D^*, D^0 in DIS	1994	$10...100$	$0.01...0.7$			
[4]	D^* DIS	94-96	$2...100$	$0.05 ... 0.7$	> 1.5	$-1.5...1.5$	
	D^* γp		< 0.01	$0.29...0.62$	> 2.5 GeV		$|\hat{y}(D^*)| < 1.5$
			< 0.009	$0.02...0.32$	> 2.0 GeV		$|\hat{y}(D^*)| < 1.5$
[5]	D^* DIS	96-97	$1...100$	$0.05...0.7$	> 1.5	$-1.5...1.5$	
	F_2^c		$1...100$	$0.05...0.7$			
[6]	D DIS	99-00	$2...100$	$0.05...0.7$	> 2.5	$-1.5...1.5$	$E_{t,jet_{1(2)}} > 4(3)$ GeV $-1 < \eta_{jets} < 2.5$
[8]	D^* DIS + jets	99-00	$2...100$	$0.05...0.7$	$1.5...15$	$-1.5...1.5$	
[7]	D^* in γp	99-00	< 0.01		> 2	$-1.5...1.5$	$171 < W_{\gamma p} < 256$ GeV
[9]	D^* + jet in γp	99-00	< 0.01		> 2	$-1.5...1.5$	$171 < W_{\gamma p} < 256$ GeV $p_t^{jet} > 3.0$ GeV
[47]	$D^*\mu$ γp	97-00	< 1	$0.05...0.75$	> 1.5	$-1.5...1.5$	$p^{\mu} > 2.0$ GeV $|\eta^{\mu}| < 1.735$
[43]	F_2^c high Q^2	99-00	> 150	$0.1...0.7$			
[46]	F_2^c low Q^2	99-00	$2...120$	$0.1...0.7$			
[45]	Charm jets γp	99-00	< 1	$0.15...0.8$			$p_t^{jet_{1(2)}} > 11(8)$ GeV $-0.8 < \eta_{jets} < 1.3$
[10]	D^* in DIS	2000	$2...100$	$0.05...0.7$	> 1.5	$-1.5...1.5$	$p_{t,jet}^{D^*} > 3$ GeV

Table 1: Overview of the measurements of open charm production at H1.

parameter, and $m_c = 1.5$ GeV. The uncertainties are estimated by variation of μ_R from $0.5m_T$ to $2m_T$ and m_c from 1.3 GeV to 1.7 GeV. Good general agreement is seen with relatively large theoretical uncertainties as estimated by simultaneous variation of the renormalization scale and the mass of the charm quark. The central values of the NLO predictions reproduce the shape of the $d\sigma/dW$ distribution and general trends of the $d\sigma/dp_t$ distributions. However, the central NLO predictions significantly underestimate the data over almost the whole kinematic range. The FONLL predictions do not provide a better description of the data than does the NLO calculation. For large $p_t(D^*)$, the FONLL predictions lie further below the data than does the NLO calculation.

In fig. 22 D^* photoproduction data from H1 are shown [7]. In this data sample the low angle scattered electron is detected in an electron detector situated 33 m away from the interaction point close to the beam pipe in electron direction. This requirement, necessary for trigger purposes, leads to a constraint on the range in $W_{\gamma p}$ of the data sample to $171 < W_{\gamma p} < 256$ GeV and restricts the statistical precision. The range in Q^2 is restricted to < 0.01 GeV^2. The data are compared with the fixed order massive calculation from [80] and the massless calculation from [96]. For the massive calculation the renormalization and factorization scales were chosen as $2\mu_R = \mu_F = 2\sqrt{m_c^2 + p_{t,c}^2}$, different from the choice of ZEUS (see above). For calculation in the 4-flavour massless scheme the BKK fragmentation function has been applied [96, 98] and the renormalization and factorization scales have been chosen as $\mu_R = \mu_F = 2\sqrt{m_c^2 + p_{t,c}^2}$ for the central prediction. The theories agree in general with the data. However, the massive

34

	Analysis	Data	Kinematic Region				
			Q^2 [GeV^2]	y	p_t^D [GeV]	η^D	Other cuts
[11]	D^* γp	1993	< 4	$0.15...0.84$	> 1.7	$-1.5...1.5$	
[12]	D^* in γp	1994	< 4	$0.15...0.87$	> 3.0	$-1.5...1.0$	
[13]	D^* in DIS	1994	$5...100$	< 0.7	$1.3...9.0$	$-1.5...1.5$	
[14]	D^* in γp	96-97	< 1	$0.19...0.87$	> 2.0	$-1.5...1.5$	
[38]	$c \to eX$ in DIS (dE/dx)	95	$2.5...170$				$-4.1 < \log(x) < -2.2$ $1.2 < p_{track} < 5.0$ $0.65 < \theta_{track} < 2.5$ rad $E_{em}/E_{tot} > 0.9$
[37]	$c \to eX$ in DIS (dE/dx)	96-97	$1...1000$	$0.03...0.7$			$1.2 < p_{track} < 5.0$ $0.65 < \theta_{track} < 2.5$ rad
[15]	D^* DIS, $K2\pi$ D^* DIS, $K4\pi$	96-97	$1...600$ $1...600$	$0.02...0.7$ $0.02...0.7$	$1.5...15$ $2.5...15$	$-1.5...1.5$ $-1.5...1.5$	
[17]	D^* dijets in γp	96-00	< 1		> 3.0	$-1.5...1.5$	$E_{t,jets} > 5$ GeV $|\eta^{jets}| < 2.4$ $130 < W_{\gamma p} < 280$ GeV $M_{jj} > 18$ GeV $|\bar{\eta}| < 0.7$
[16]	D^* in DIS	98-00	$1.5...1000$	$0.02...0.7$	$1.5...15$	$-1.5...1.5$	
[23]	D in DIS	98-00	$0.05...0.7$ $1.5...1000$	$0.02...0.85$ $0.02...0.7$	$1.5...9$ > 3.0	$-1.5...1.5$ $-1.6...1.6$	
[24]	$D^\pm$ in DIS	2004	> 4		> 2.0	$-1.5...1.5$	
[22]	D^*+jets in γp	98-00	< 1		> 3	$-1.5...1.5$	$130 < W_{\gamma p} < 280$ GeV $E_t^{jet} > 6$ GeV $-1.5 < \eta^{jet} < 2.4$
[21]	D^*+jets in γp (frag. funct.)	98-00	< 1		> 2	$-1.5...1.5$	$130 < W_{\gamma p} < 280$ GeV $E_t^{jet} > 9$ GeV $-2.4 < \eta^{jet} < 2.4$
[19]	D^* in γp	98-00	< 1		$1.9...20$	$-1.6...1.6$	$130 < W_{\gamma p} < 285$ GeV $p_t(D^*)/E_t^{\theta>10°} > 0.15$
[20]	D in γp	98-00	< 1		> 3.8	$-1.6...1.6$	$130 < W_{\gamma p} < 300$ GeV
[49]	D^{**}	95-00			> 2	$-1.5...1.5$	$p_t(D^*)/E_t^{\theta>10°} > 0.15$
[50]	$D_{s1}^\pm$	95-00			> 2	$-1.5...1.5$	$p_t(D^*)/E_t^{\theta>10°} > 0.15$
[25]	D^*+dijets in γp	98-00	< 1				$E_t^{jet} > 7(6)$ GeV $-1.5 < \eta^{jet} < 2.4$ $130 < W_{\gamma p} < 280$ GeV
[26]	D DIS	98-00	$1.5...1000$	$0.02...0.7$	> 3	$-1.6...1.6$	

Table 2: Overview of the measurements of open charm production at ZEUS.

calculation appears to produce somewhat too hard a p_t spectrum while the massless calculation fits the data better both in shape and in normalization.

6.1.2 Inclusive Charm Production in DIS

Recent measurements of inclusive D^* meson production cross sections in DIS are presented in fig. 23 [8, 16]. The two data sets agree with each other within the large experimental errors of the preliminary H1 data and are described by the NLO QCD prediction HVQDIS [81].
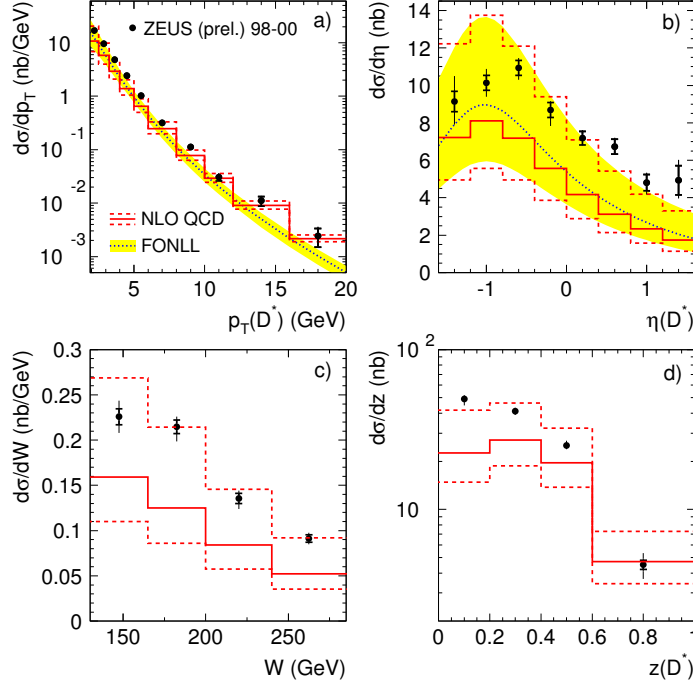
Figure 21: Differential cross sections for inclusive D^* photoproduction in the process $ep \rightarrow D^*X$:a) $d\sigma/dp_t$, b) $d\sigma/d\eta$, c) $d\sigma/dW$ and d) $d\sigma/dz$ [19]. The predictions of NLO calculations with the central choice of parameters are given by the solid histograms [80]. The dashed histograms show the scale uncertainties of the fixed order NLO prediction (see text). The FONLL predictions [92], are shown as dotted curves and their uncertainties are given by the shaded bands.
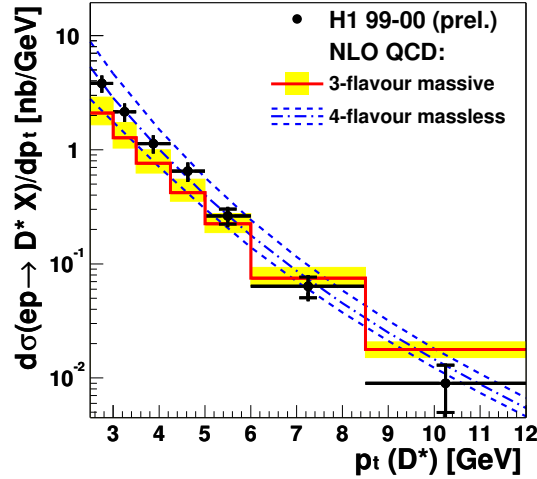

Figure 22: Differential D^* photoproduction cross section $d\sigma/dp_t$ as a function of p_t of the D^* meson. The data are compared with NLO QCD calculations in the 3-flavour massive [80] and in the 4-flavour massless scheme [96] (taken from [7]).
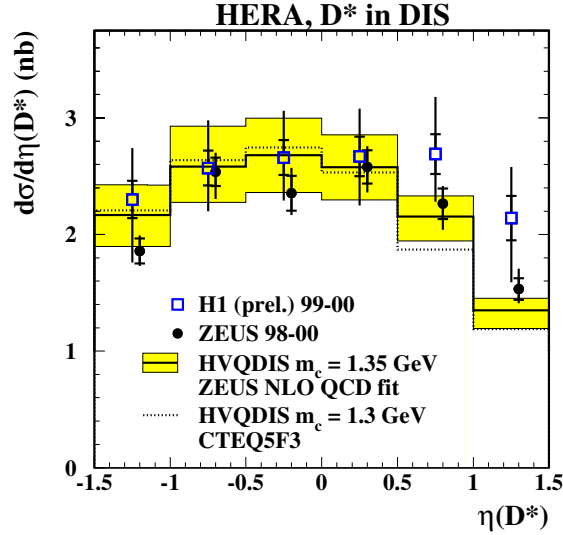
36

Figure 23: a) Inclusive D^* cross sections in DIS from both HERA experiments compared with a prediction from NLO QCD [8, 16].

ZEUS and H1 have measured the open-charm contribution $F_2^{c\bar{c}}$ to the proton structure function F_2. In fig. 24 the structure function $F_2^{c\bar{c}}(x, Q^2)$ is shown as a function of x in different bins of Q^2. The data from H1 [5, 43, 46] and ZEUS [15, 16] are found to be in good agreement with each other and with the prediction in next-to-leading order as taken from a recent ZEUS NLO fit [68]. The data rise with increasing Q^2, the rise becoming steeper at lower x, demonstrating the property of scaling violations in charm production. The uncertainty on the theoretical prediction comes from the uncertainty of the PDF fit to the inclusive data from which the charm component is calculated dynamically, i.e. in the massive scheme. At small and moderate Q^2, the uncertainty in the data is comparable to the PDF uncertainty shown. This implies that the double-differential cross sections could be used as an additional constraint on the gluon density in the proton. At moderate Q^2 the most precise measurement of $F_2^{c\bar{c}}$ [46] is achieved by evaluation of the charm lifetime distribution in an inclusive event sample using the H1 silicon vertex detector. Details of the analysis method and results are given in sections 5.5.2 and 6.2.2.

6.1.3 Charm Jet Cross Sections

The measurement of D^* mesons in events with dijets enhances the sensitivity to higher order effects. Figure 25 shows the H1 cross sections in the DIS regime for the production of dijets in association with a D^* meson versus the D^* meson production cross section [8]. A transverse momentum of at least 4(3) GeV is required for the highest (second highest) p_t jet, respectively. The Monte Carlo simulations RAPGAP, AROMA, CASCADE all reproduce the inclusive cross section but do not describe the cross section of dijets in association with a D^* meson. While RAPGAP and AROMA (based on the DGLAP evolution equations) are too low in normalization, the CASCADE Monte Carlo generator (based on the CCFM equation) is too high. HERWIG fails to describe the data for both the inclusive and the dijet selection.

In dijet processes the contribution from resolved processes can be measured. The variable x_γ^{obs} gives the energy fraction in the proton rest frame, of the parton from the photon entering
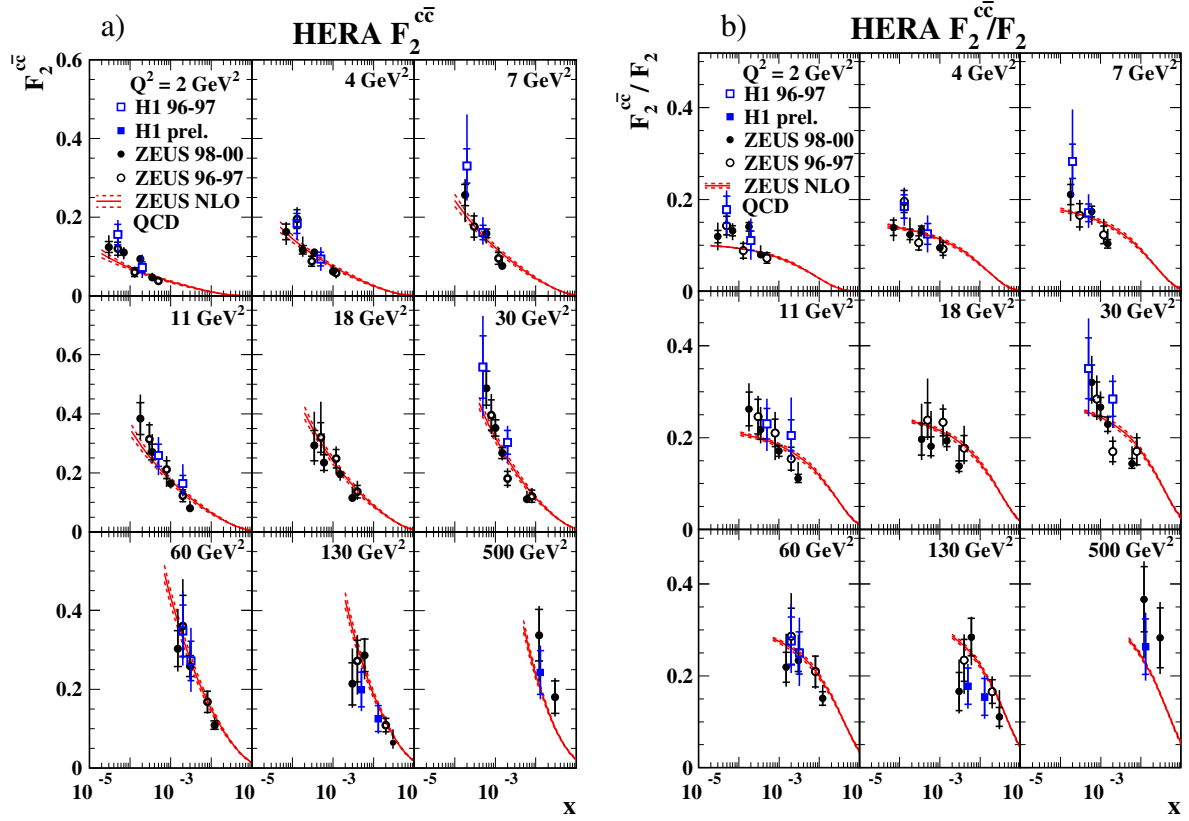
Figure 24: Measurements of the contribution $F_2^{c\bar{c}}$ from charm to the proton structure function $F_2(x, Q^2)$. The H1 and ZEUS data are presented as functions of x in different bins of Q^2 and compared with a prediction at next-to-leading order.

the hard subprocess. It is reconstructed using the two highest transverse energy jets as

$$x_\gamma^{\text{obs}} = \frac{\sum_{\text{jet1,2}}(E - p_z)}{2yE_e} \tag{6}$$

where E_e is the electron beam energy and y is the photon inelasticity, i.e. the fractional electron energy carried by the exchanged photon. For the direct process (fig 5a in section 2.3), x_γ^{obs} approaches unity, as the hadronic final state consists of only the two hard jets and the proton remnant in the forward region. Energy depositions of the proton remnant in the forward direction contribute little to x_γ^{obs} since $\sum_h(E - p_z) \approx \sum_h E(1 - cos\theta)$ and $\theta_{p-\text{remnant}}$ is close to 0. In resolved processes (fig. 5b-d in section 2.3) x_γ^{obs} can be small. Other effects that lead to values of x_γ^{obs} smaller than unity are jet splitting, i.e. when two jets are reconstructed which originate from the same mother parton, and higher order effects, e.g. when hard gluons are radiated off the quarks.

The ZEUS dijet photoproduction cross section [17] as a function of x_γ^{obs} is shown in the figures 26a and b compared with predictions from PYTHIA [108], HERWIG [125] and CAS-CADE [104], as well as a fixed order massive calculation [80] in NLO QCD. A significant part of the cross section is situated at low values of x_γ^{obs}. In the approach of collinear factorization at leading order this is consistent with the presence of resolved photon processes.

38

H1 preliminary

$\sigma(D^* jjX)$ [nb]

- ● H1 D^*
- ■ CASCADE ε=0.10
- ▲ CASCADE ε=0.078
- ▼ CASCADE ε=0.035
- ☆ RAPGAP dir.+res.
- ✩ RAPGAP dir.
- ⊕ HERWIG
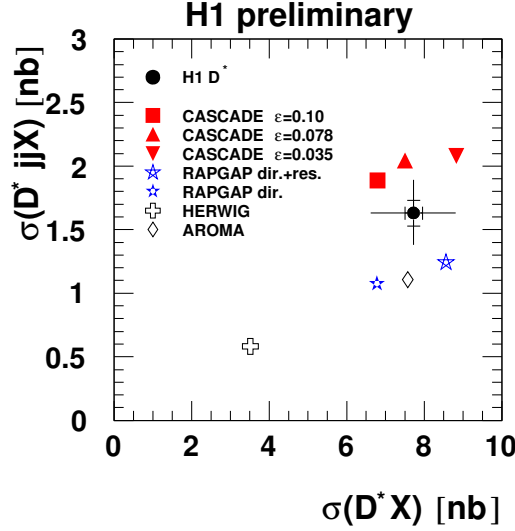- ◇ AROMA

$\sigma(D^* X)$ [nb]

Figure 25: The D^* dijet cross section versus the inclusive D^* cross section in comparison with various models [8]. The dijet cross sections as a function of E_t of the leading jet are shown in fig. 60.

6.1.4 Dijet Angular Distributions

Angular distribution of jets are measured to study the distributions of the outgoing partons and to gain understanding of the parton dynamics of the underlying sub-processes. As described in section 2.3 different types of resolved processes are expected to contribute. In the case of excitation diagrams (fig. 5c-d) both quark and gluon propagators are possible. In $g-$exchange (fig. 5d in section 2.3), the spin-1 propagator of the gluon leads to a steeper angular dependence ($\sigma \sim (1 - |\cos\theta^*|)^{-2}$) than for quark exchange ($\sigma \sim (1 - |\cos\theta^*|)$).

Figures 26c-f show the differential cross-section $d\sigma/d\cos\theta^*$ for both direct ($x_\gamma^{\mathrm{obs}} > 0.75$) and resolved enriched ($x_\gamma^{\mathrm{obs}} < 0.75$) samples [17]. Here, θ^* is the angle between the charm-jet axis and the p-beam direction in the dijet rest frame. The charm jet is identified by association of the D^* meson with the jet using a criterion $R = \sqrt{(\eta^{jet} - \eta^{D^*})^2 + (\phi^{jet} - \phi^{D^*})^2} < 0.6$. Positive (negative) values of $\cos\theta^*$ correspond to cases in which the identified charm jet, which is associated to the reconstructed D^* meson, is oriented in the direction of the incoming proton (photon). The shaded areas for $x_\gamma^{\mathrm{obs}} < 0.75$ and $x_\gamma^{\mathrm{obs}} > 0.75$ are, respectively, the contamination of the genuine direct and resolved PYTHIA contributions. The measured differential cross sections $d\sigma/d\cos\theta^*$ for both samples are significantly different. For $x_\gamma^{\mathrm{obs}} < 0.75$ a particular enhancement of the cross section for charm jets is seen in the photon direction (negative $\cos\theta^*$). In contrast, in the region $x_\gamma^{\mathrm{obs}} > 0.75$ the angular distributions reveal a much shallower behaviour. The differences provide an indication that a sizable fraction of the resolved photon events proceeds via gluon exchange for which a steep angular distribution is expected.

New preliminary results are available for the angular correlations in azimuth in charmed photoproduction events containing jets. In leading order the $\Delta\phi$ distribution is expected to show a sharp peak at $180°$. Contributions from higher orders, i.e. hard gluon radiation, as well as fragmentation and detector resolution effects smear the distributions out. The ZEUS experiment uses a dijet sample to measure the difference $\Delta\phi$ of the two jets [25] while H1
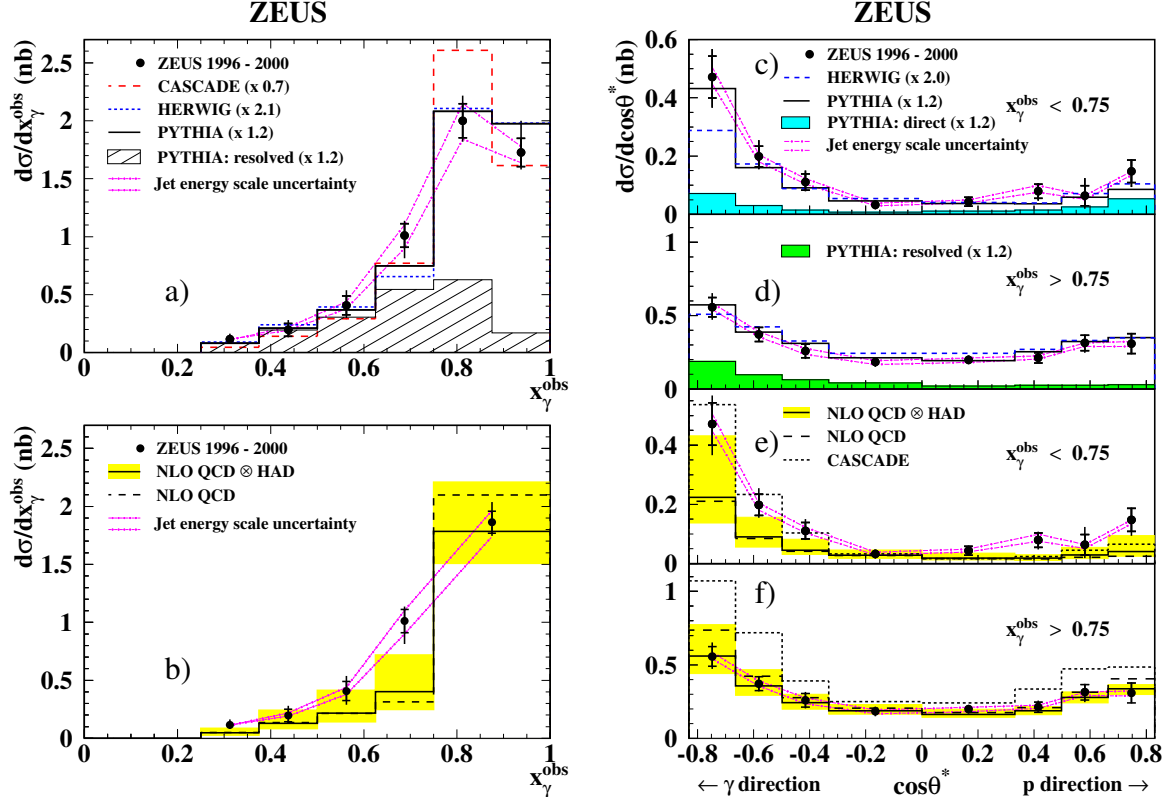
39

Figure 26: Differential D^* dijet photoproduction cross sections from ZEUS [17], a) $d\sigma/dx_\gamma^{obs}$ in comparison with Monte Carlo generators CASCADE, PYTHIA and HERWIG, b) $d\sigma/dx_\gamma^{obs}$ in comparison with NLO FO predictions after hadronization correction (full lines) and at parton level (dashed lines). c-f) $d\sigma/d\cos\theta^*$ as a function of $\cos\theta^*$ for the region of $x_\gamma^{obs} < 0.75$ (resolved-enhanced, c and e) and $x_\gamma^{obs} > 0.75$ (direct-enhanced, d and f) (see text). Also shown are predictions from Monte Carlo generators (c and d) which are individually scaled in normalization and from a NLO fixed order QCD calculation (e and f). The dashed-dotted lines show the jet-energy-scale uncertainty of the data.

measures the difference between the reconstructed D^* meson and the leading jet which does not belong to the D^* meson [9]. In fig 27 the two measurements are shown, revealing similar features. The data have a shallower behaviour in $\Delta\phi$ than the theories, indicating that the theories, at next-to-leading order, can not fully account for the amount of gluon radiation seen in the data.

6.1.5 Charm Fragmentation Functions

Samples of charmed dijet events, where charm is identified by the presence of a D^*-meson have been used to perform measurements of the fragmentation functions [10, 21]. The distributions are parameterized by fragmentation functions which describe the transfer of the quark's energy to a given hadron (see section 2.4). Comparisons of the HERA measurements with data from experiments at e^+e^- colliders provide tests of the universality of charm fragmentation.
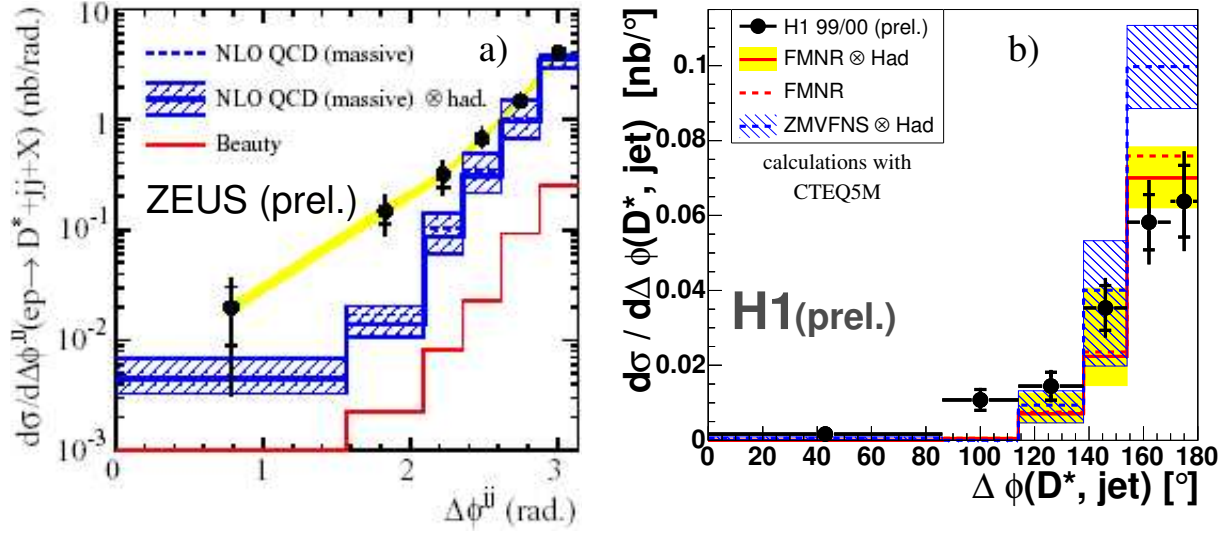
Figure 27: Differential cross sections as a function of $\Delta\phi$ for a) a charmed dijet sample from ZEUS [25] in comparison with a massive NLO calculation, b) a D^*-jet sample from H1 [9] in comparison with massive (FMNR) and massless (ZMVFNS) NLO calculations.
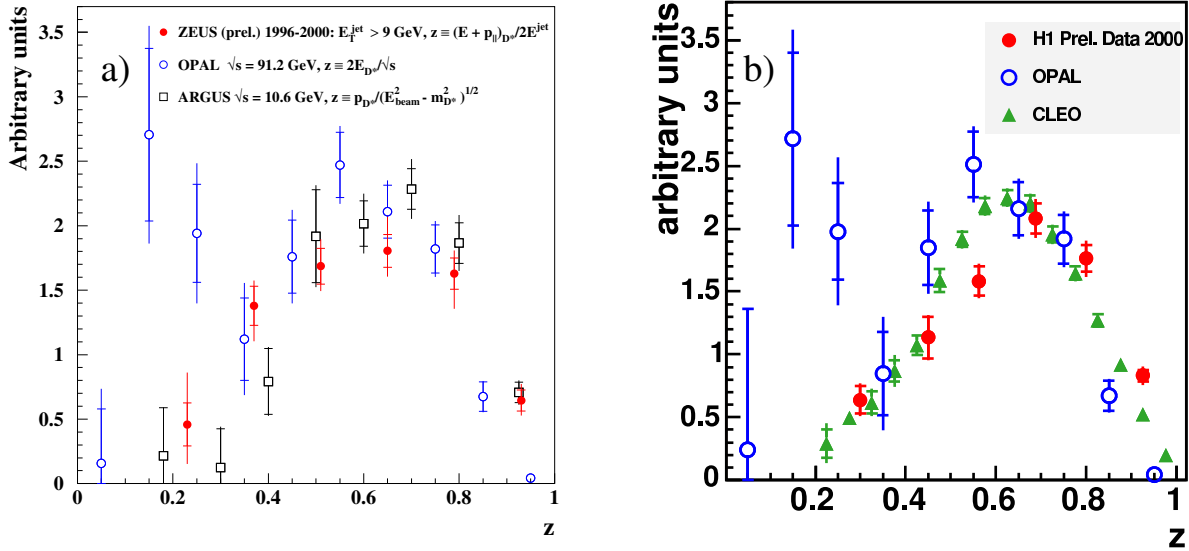

Figure 28: Shape comparison of the event distribution as a function of a) z_{jet} for the ZEUS data (solid points), compared to measurements of the OPAL (open circles) and ARGUS (open squares) collaborations, and b) z_{hem} for the H1 data (solid points), compared to the same OPAL data as shown in a) (open circles) and the CLEO data (triangles).

41

At HERA, in contrast to e^+e^- colliders, the kinematics of the initial boson-gluon state are not constrained such that the relative hadron momentum must be determined solely from the measured final state observables. Figure 28 shows the acceptance corrected distributions of the ZEUS and H1 charm dijet events as a function of the fragmentation variable z, which describes momentum fraction carried by the D^* meson relative to the initial charm quark.

In the case of ZEUS [21] (fig. 28a) photoproduction data with two jets of high transverse energy, $E_t > 9$ GeV, are used and the observable z is reconstructed as

$$z_{jet} = \frac{(E + p_\parallel)^{D^*}}{2E^{jet}}, \tag{7}$$

where $p_\parallel$ is the longitudinal momentum of the D^* meson relative to the axis of the associated jet of energy E^{jet}.

The H1 collaboration [10] (fig. 28b) uses an inclusive sample of D^* mesons in DIS, $2 < Q^2 < 100$ GeV^2, with jets of at least 3 GeV in transverse momentum, and also an alternative method to reconstruct the observable z. In the hemisphere method, the projections of the particle momenta perpendicular to the γ^*p axis are calculated and a thrust axis is found. The projected event is divided into two hemispheres, one of them containing the D^* meson and other hadrons. z is then defined as

$$z_{hem} = \frac{(E + p_\parallel)^{D^*}}{\sum_{\text{hem}}(E + p)}, \tag{8}$$

where in the denominator the energies and three-momenta of all particles with momentum projections in the D^* hemisphere are summed. In contrast to the jet method used for the ZEUS measurement, the hemisphere method includes contributions from hard gluons in analogy with the method used in e^+e^- experiments.

The ZEUS and H1 data show similar features as those from OPAL [154], ALEPH [115], ARGUS [155] and CLEO [156] and reach a compatible precision. The CLEO and ARGUS data are situated at a similar center-of-mass energy of the $c\bar{c}$-pair as those of H1, i.e. at $\sqrt{s} \approx 10$ GeV, while the OPAL and ALEPH data are significantly higher ($\sqrt{s} = 91.2$ GeV). The OPAL data show a large contribution from gluon splitting at small values of z due to the large jet energy available at LEP. The result supports the assumption of universality of the charm fragmentation functions made in earlier measurements and allows to improve the uncertainties due to fragmentation effects for future measurements. A fit of the ZEUS photoproduction data to the Peterson fragmentation function [109] using the PYTHIA leading order parton shower Monte Carlo generator and the Lund string fragmentation model for lighter flavours [108] yields a value for the Peterson fragmentation parameter $\epsilon = 0.064 \pm 0.006^{+0.011}_{-0.008}$ [21]. The H1 DIS data [10] show a somewhat harder z-spectrum and the corresponding Peterson fragmentation parameter is found to be $\epsilon_{jet} = 0.030^{+0.006}_{-0.005}$, using the same reconstruction of z_{jet} as ZEUS, which is based on reconstructed jets, as given in equation (7). For the hemisphere method, as given in equation (8), a somewhat smaller value $\epsilon_{hem} = 0.018^{+0.004}_{-0.003}$ is found. For both analysis from ZEUS and H1, the determination of the fragmentation functions in the framework of a next-to-leading order calculation is not yet available.
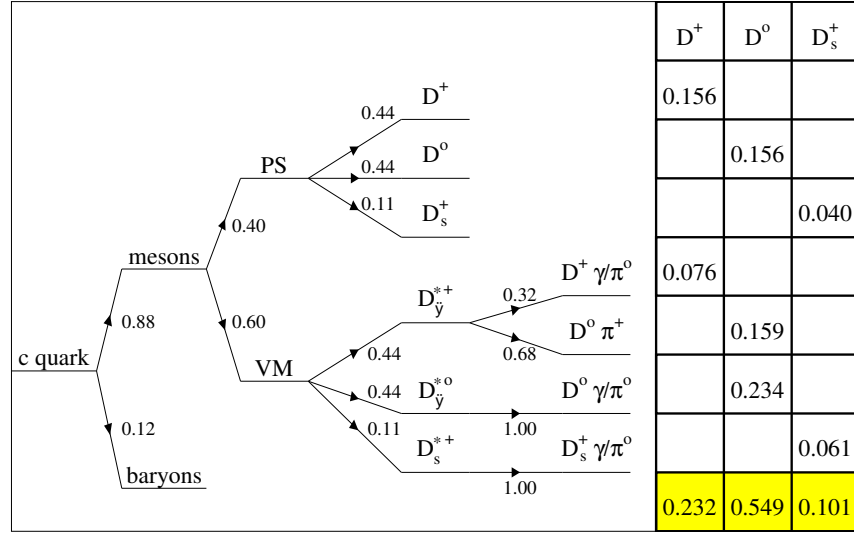
	D^+	D^o	D_s^+
D^+	0.156		
D^o		0.156	
D_s^+			0.040
$D^+ \, \gamma/\pi^o$	0.076		
$D^o \, \pi^+$		0.159	
$D^o \, \gamma/\pi^o$		0.234	
$D_s^+ \, \gamma/\pi^o$			0.061
	0.232	0.549	0.101

Figure 29: The charm fragmentation tree into D and D^* mesons. The numbers indicate the world average values for the fragmentation fractions [144]. The table to the right sums the contributions of the directly and indirectly produced pseudo scalar D mesons to the $f(c \to D)$ factors.

6.1.6 Charm Fragmentation Fractions

The probability of a c quark to hadronize as a particular charm hadron, D^+, D^0, D_s, D^* or Λ_c is described by the charm fragmentation fractions $f(c \to D$ or $\Lambda_c)$. Like the fragmentation functions, the fractions are assumed to be universal and previous measurements of charm cross sections have used the values in [144] which are dominated by results from e^+e^- experiments [115, 116, 129, 154, 155, 157–159].

The fragmentation fractions for charm at HERA are determined by separate measurements of the production cross sections for four D mesons and the Λ_c baryon, in both photoproduction (ZEUS [20]) and in DIS (H1[4] [6] and ZEUS [26]). The following channels and their corresponding charge conjugates are used: $D^+ \to K^-\pi^+\pi^+$, $D^0 \to K^-\pi^+$, $D_s^+ \to \phi\pi^+ \to (K^+K^-)\pi^+$, $D^{*+} \to D^0\pi_s^+ \to (K^-\pi^+)\pi_s^+$, $\Lambda_c \to K^-p\pi^+$.

In fig. 29 the various charmed D mesons are shown, grouped in scalar and vector mesons. The experimentally determined fragmentation factors $f(c \to D, \Lambda_c)$ include all possible decay chains that result in that particular charmed hadron, in addition to the direct production. The measured pseudoscalar D^+, D^0 and D^s mesons contain a large fraction of mesons produced in $D^*_{(s)}$ decays and the Λ_c contains small fractions from decays of the strange-charm baryons $\Xi^{\pm}$, Ξ^0 and Ω_c^0.

The differential production cross sections for all four D mesons measured by the H1 collaboration [6] in the same kinematic region are shown in fig. 30. The measured visible cross sections are scaled by the fragmentation fractions as determined from the integrated cross sections. The similarity of the distributions implies that the fragmentation fractions are independent of kinematics and can be measured from the integrated D meson cross sections.

---

[4]In the H1 analysis the Λ_c baryon resonance was not reconstructed and the fragmentation fraction for the Λ_c was taken from [144].
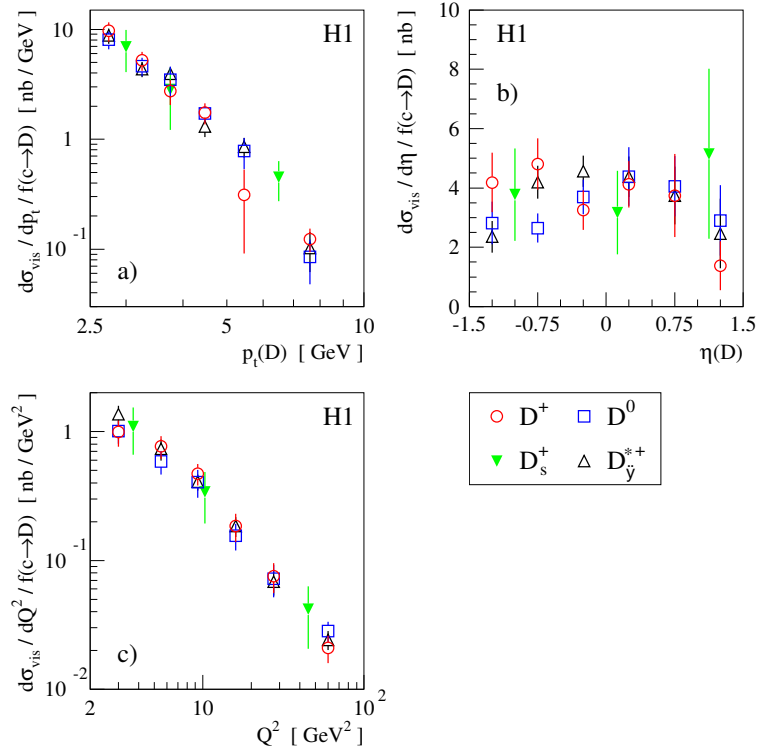
Figure 30: Visible differential production cross sections for four D mesons in the DIS regime, divided by their respective measured fragmentation factors [6]. a) D meson transverse momentum $p_t(D)$, b) pseudo-rapidity $\eta(D)$, c) photon virtuality Q^2. An overall common systematic error of 15% is not shown.
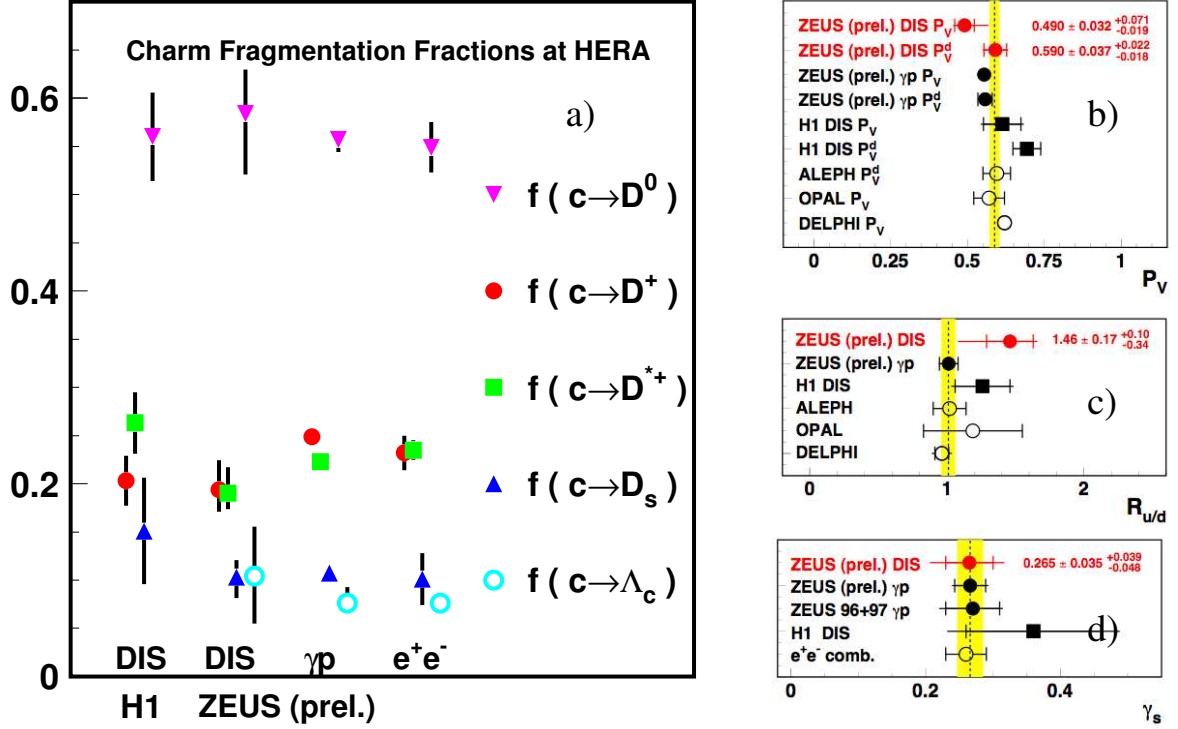
Figure 31: Charm fragmentation fractions for different processes. a) Data from DIS (H1 [6], ZEUS [26]), γp (ZEUS [20]) and e^+e^- [144] measurements are compared for the different charm hadrons. b-d) Ratios of the total production rates b) P_V, c) $R_{u/d}$ and d) γ_s from H1, ZEUS and e^+e^- experiments.

Constraints can be explicitly imposed on the measurements, which improve the experimental accuracy. The constraint $1 = f(c \to D^+) + f(c \to D^0) + f(c \to D_s) + f(c \to \Lambda_c, \Xi_c, \Omega_c)$ introduces contributions to charm fragmentation processes which are not determined in the analyses. World average values [144] are taken instead.

Figure 31a shows the results for fragmentation fractions as determined at HERA and at e^+e^- colliders. The values in different kinematic regimes and at the different colliders are in good agreement, so the assumption that charm fragmentation fractions are universal is confirmed.

Ratios of the total production rates are used to perform further tests of the universality of charm fragmentation. The fraction P_V of D mesons produced in a vector state is consistent among the various experiments (fig. 31b). The expected isospin invariance of the fragmentation process, as quantified by the observable $R_{u/d}$ which gives the probabilities for a charm quark to hadronize together with a u or a d quark, is seen to be fulfilled (fig. 31c). The strangeness suppression factor γ_s (fig. 31d) is found to be of order 30%. These results support the universality assumptions for charm fragmentation.

6.2 Beauty Production

For beauty production, theoretical calculations in perturbative quantum chromodynamics are expected to give predictions that are more reliable than for charm, as the mass m_b of the b quark

	Analysis	Data	Kinematic Region		
			Q^2 [GeV^2]	y	Other cuts
H1					
[36]	$b \to \mu X$ in γp	1996	< 1	0.1...0.8	$35° < \theta^\mu < 130°$ $\quad p_t^\mu > 2.0$ GeV
[44]	$b\bar{b} \to \mu jj$ in γp	99-00	< 1	0.2...0.8	$p_t^{jet\,1\,(2)} > 7\,(6)$ GeV $\quad |\eta^{jet}| < 2.5$ $-0.55 < \eta^\mu < 1.1$ $\ p_t^\mu > 2.5$ GeV
	$b \to \mu j$ in DIS	99-00	2...100	0.1...0.7	$p_{T,jet}^{Breit} > 6$ GeV $\quad |\eta^{jet}| < 2.5$ $-0.75 < \eta^\mu < 1.15$ $\ p_t^\mu > 2.5$ GeV
[47]	$bb \to D^*\mu$ in γp	96-00	< 1	0.05...0.75	$p_t(D^*) > 1.5$ GeV $\quad |\eta(D^*)| < 1.5$ $p^\mu > 2.0$ GeV $\quad |\eta^\mu| < 1.735$
[43]	F_2^b at high Q^2	99-00	> 150	0.07...0.7	
[46]	F_2^b at low Q^2	99-00	2...120	0.07...0.7	
[45]	dijets in γp	99-00	< 1	0.15...0.8	$p_t^{jet_{1(2)}} > 11\,(8)$ GeV $\quad -0.8 < \eta_{jets} < 1.3$
ZEUS					
[39]	$b\bar{b} \to ejj$ in γp	96-97	< 1	0.2...0.8	$E_t^{jet\,1\,(2)} > 7\,(6)$ GeV $\quad |\eta^{jet}| < 2.4$ $|\eta^{e^-}| < 1.1$ $\ p_t^{e^-} > 1.6$ GeV
[40]	$b\bar{b} \to \mu jj$ in γp	96-00	< 1	0.2...0.8	$p_t^{jet\,1\,(2)} > 7\,(6)$ GeV $\quad |\eta^{jet}| < 2.5$ $-1.6 < \eta^\mu < 1.3\ p^\mu > 2.5$ GeV or: $1.48 < \eta^\mu < 2.3\ p^\mu > 1(4)$ GeV
[41]	$bb \to \mu j$ in DIS	99-00	> 2	0.05...0.7	$E_{T,jet}^{Breit} > 6$ GeV $\quad -2 < \eta_{jet}^{lab} < 2.5$ $(-0.9 < \eta^\mu < 1.3\ p_t^\mu > 2.0$ GeV$)$ or: $(-1.6 < \eta^\mu < -0.9\ p^\mu > 2.0$ GeV$)$
[48]	$bb \to D^*\mu$	96-00	< 1 > 2	0.05...0.85 0.05...0.7	$p_t^{D^*} > 1.9\ |\eta_{D^*}| < 1.5$ $p_t^\mu > 1.4$ GeV $\ -1.75 < \eta_\mu < 1.3$
[42]	$bb \to \mu\mu$	96-00			$-2.2 < \eta_\mu < 2.5$ $\quad p_t^{\mu_1} > 1.5$ GeV $p_t^{\mu_2} > 1.8$ GeV for $\eta < 0.6$ $p^{\mu_2} > 2.5$ GeV or $p_t^{\mu_2} > 1.5$ GeV for $\eta > 0.6$

Table 3: Overview of the measurements of open beauty production at H1 and ZEUS.

($m_b \sim 5$ GeV) provides an energy scale in a region in which perturbative approaches have been successful in describing the data.

Experimentally, measurements of beauty production are somewhat more challenging than measurements of charm production because the beauty cross sections and branching ratios are significantly smaller than those of charm. Consequently, the explicit reconstruction of hadronic resonances containing beauty is not viable at HERA, due to lack of statistics. The measurements preformed at the HERA experiments H1 and ZEUS make use of semi-leptonic decays of beauty hadrons and, in more recent analyses, lifetime distributions have been used to distinguish beauty from charm and light quark events (see also section 5.5). In table 3 an overview of the measurements of beauty production performed at HERA is given.

The first measurements of the beauty cross section at HERA [36,39] were higher than pQCD predictions, calculated at next-to-leading order. Similar observations were made in hadron-hadron collisions [160] and also in two-photon interactions [161].
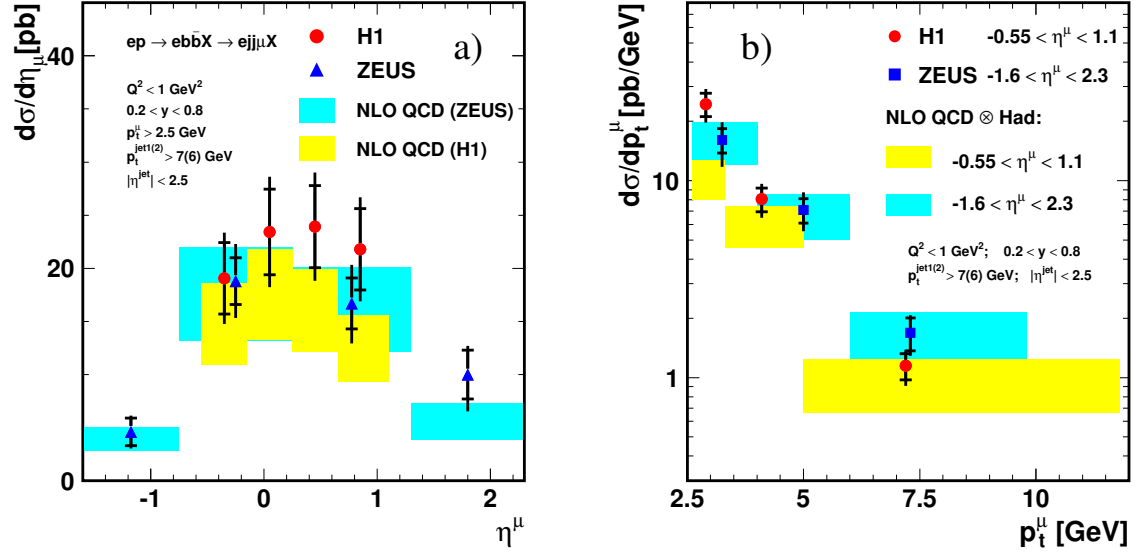
Figure 32: Differential beauty photoproduction cross sections from H1 [44] and ZEUS [40] as a function of a) the pseudo-rapidity and b) the transverse momentum of the muon. The shaded bands reflect the predictions from FMNR as calculated for the ZEUS data (dark shaded) and H1 data (light shaded).

6.2.1 Jet-Muon Analyses

Both H1 and ZEUS have presented measurements in which the events containing beauty are identified using high p_t muons from semileptonic b decays [36–41, 44]. The beauty signal events are distinguished from the charm and light quark background by means of observables which exploit the large mass (H1 and ZEUS, see section 5.6) and the long lifetime of the b quarks (H1, see section 5.5).

Figure 32 shows the differential photoproduction cross-sections as a function of the muon pseudo-rapidity for the process $ep \rightarrow eb\bar{b}X \rightarrow e\,\text{jet}\,\text{jet}\,\mu$. The H1 [44] and ZEUS [40] data, which are in reasonable agreement, are compared to NLO calculations in the massive scheme [80]. The same scales and parton density distributions are used in both analyses. While the ZEUS data are well described by the theory, the H1 data at low transverse momenta are observed to be somewhat higher than the expectations. The errors of the theory prediction are dominated by the uncertainties of the renormalization scale and the b quark mass. In the calculations different parameter choices, e.g. for the modeling of the hadronization and decay of the B hadron, lead to variations of the prediction of up to $\sim 12\%$.

ZEUS [41] and H1 [44] have also measured the jet-muon beauty cross section in DIS events with at least one hard jet in the Breit frame, $p_{t,Breit}^{jet} > 6$ GeV, together with a muon for photon virtualities $Q^2 > 2$ GeV^2. The measurements from H1 and ZEUS are performed in slightly different kinematic regions (see table 3). Comparisons of the data with the NLO QCD calculation in the massive scheme [81] show that the data are higher than the predictions by about 2 standard deviations.
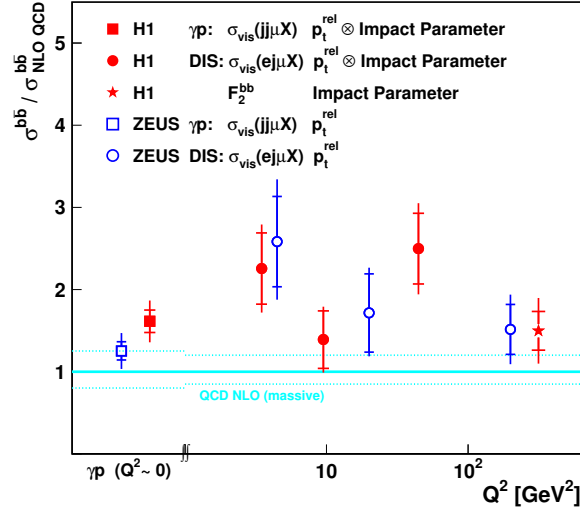
Figure 33: Ratio of beauty production cross section measurements at HERA [40, 41, 43, 44] to the NLO QCD predictions FMNR (photoproduction) and HVQDIS (DIS).

The results of the beauty measurements with jets and muons at HERA are summarized in fig. 33 where the ratios between the measured beauty production cross sections and the corresponding next-to-leading order predictions in the massive scheme [80, 81] are shown as a function of the photon virtuality Q^2. The data tend to be somewhat higher than the predictions but still in agreement.

In earlier measurements [36, 39] NLO QCD predictions were used to extrapolate the measured visible cross sections for dijet events with a lepton to more inclusive μ or b-quark production cross sections. In these measurements softer jet and muon cuts were used in order to overcome statistical limitations. In [40] ZEUS extracted the b quark differential cross section as a function of the quark transverse momentum for a b quark pseudo-rapidity range in the laboratory frame $|\eta_b| < 2$ and the result was found to be consistent with the previous ZEUS result from semi-leptonic B decays into electrons [39], translated into the b quark cross section for $p_t^b > 5$ GeV and $|\eta| < 2$ and also with the most recent results. In a previous measurement by H1 [36] the inclusive $b \rightarrow \mu X$ cross section was found to be 2.3 standard deviations higher than the new measurement [44] when extrapolated into the same kinematic range using the same model assumptions. In this early measurement the cuts on the jet and muon transverse momenta were comparably loose (see table 3). It can be concluded that the difference between this measurement and the later measurements is not due to extrapolation effects, as suggested e.g. in [162, 163], but mainly results from experimental effects which may occur when going to small values of p_t of the b-quark. Similar excesses of the cross section above expectation appear to be visible in other measurements of the beauty cross sections which probe the region of small p_t of the beauty quark (see sections 6.3.1 and 6.3.2).
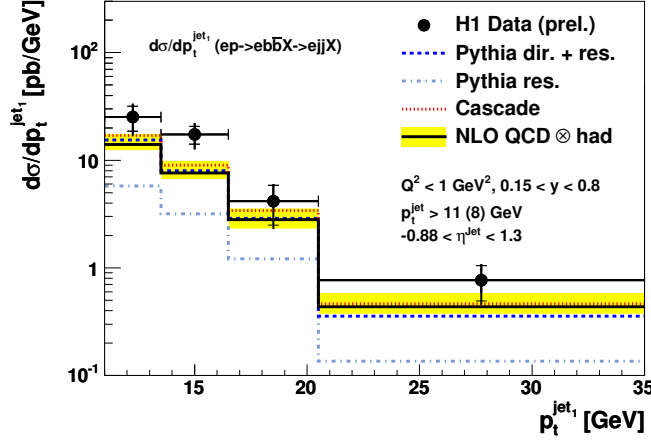
48

Figure 34: Differential beauty photoproduction cross section as a function of the jet transverse momentum as determined from lifetime distributions [45]. Also shown are the NLO QCD expectation in the massive scheme [80] as well as the Monte Carlo calculations PYTHIA [108] and CASCADE [104].

6.2.2 Inclusive Lifetime Tag Analyses

The H1 Experiment has reported new beauty and charm measurements [43, 45, 46] in which the impact parameters of selected tracks coming from secondary decay vertices are used to identify beauty and charm events (see section 5.5.2). The track selection requires full silicon vertex detector information and imposes a transverse momentum cut $p_t > 500$ MeV.

The dijet beauty photoproduction cross section is measured for events with two jets with $p_t > 11(8)$ GeV [45] in the central region of pseudo-rapidity. In fig. 34 the differential cross section is presented as a function of the jet transverse momentum p_t. The data are found to be higher than predictions from the NLO QCD calculation in the massive scheme FMNR [80] and from the Monte Carlo programs PYTHIA [108] and CASCADE [104] by about a factor of 1.8. The result for the charm dijet cross section as obtained in the same analysis shows good agreement of the theory with the data.

The beauty and charm structure functions have been determined by the H1 collaboration in the range $12 < Q^2 < 650$ GeV and $0.07 < y < 0.7$ (see fig. 35). In this kinematic range, more than 80% of the charm events and more than 96% of the beauty events have a track within the detector acceptance. The extrapolation from the measured sample to the full phase space is therefore small, leading to small uncertainties due to model assumptions. This is the first measurement of $F_2^{b\bar{b}}$.

The measurements of $F_2^{b\bar{b}}$ are shown in fig. 35. The results for $F_2^{c\bar{c}}$ from this and other analyses are shown in fig. 24. Scaling violations are visible which increase towards lower values of x, indicating that towards low x charm and beauty production is dominated by the boson-gluon fusion process. The beauty data are compared with a NLO QCD predictions from NLO QCD [164] and with a recent prediction in NNLO [60]. Both calculations are performed in the variable flavour number scheme. The predictions of the QCD calculations are compatible with the data.
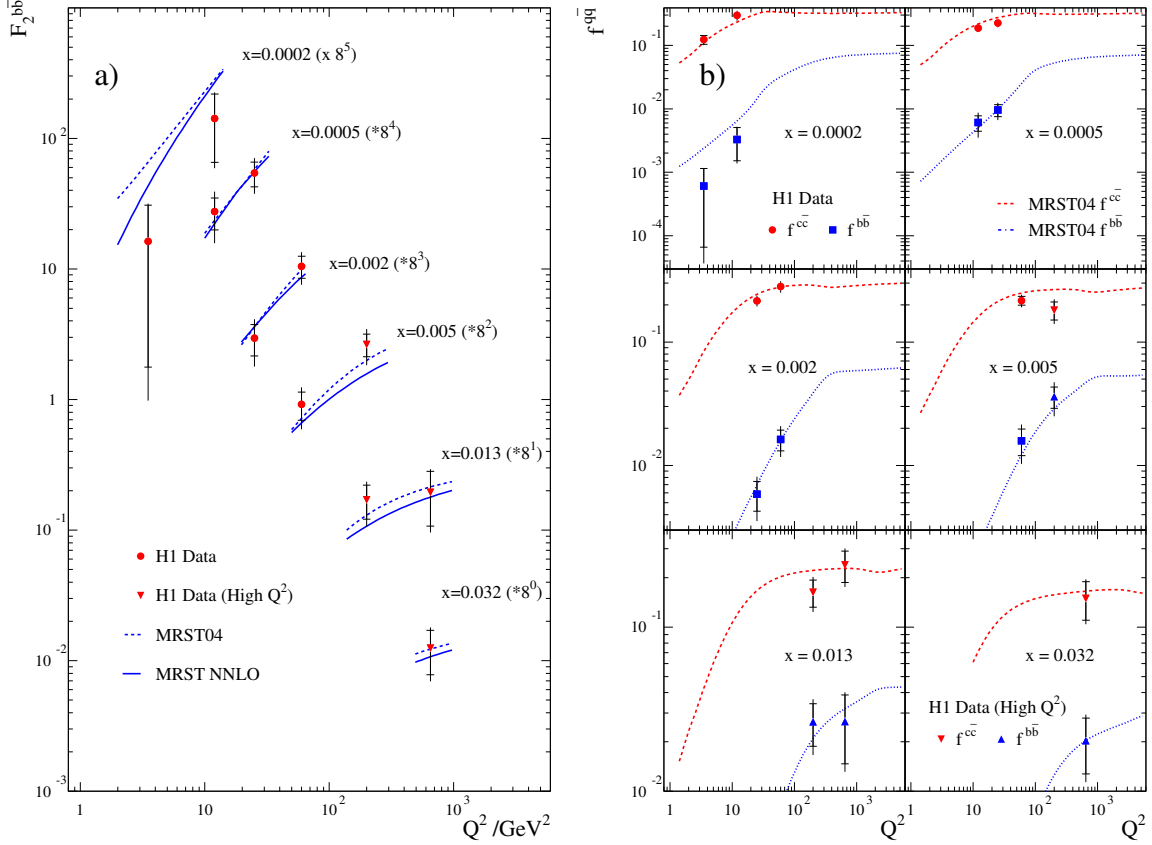
Figure 35: a) The measured structure function $F_2^{b\bar{b}}$ shown as a function of Q^2 for different values of x. The inner error bars show the statistical error, the outer error bars represent the statistical and systematic errors added in quadrature. The data are compared with a NLO QCD prediction [164] and with a NNLO QCD prediction [60]. b) The contributions to the total cross section $f^{c\bar{c}}$ and $f^{b\bar{b}}$ (see text) shown as a function of Q^2 for different bins of x. The lines indicate the prediction from the NLO QCD fit in the variable flavour number scheme [164].

In fig. 35b the measurements are presented in the form of the fractional contribution to the total ep cross section

$$f^{c\bar{c}} = \frac{\mathrm{d}^2\sigma^{c\bar{c}}}{\mathrm{d}x\mathrm{d}Q^2}\bigg/\frac{\mathrm{d}^2\sigma}{\mathrm{d}x\mathrm{d}Q^2}. \tag{9}$$

The b fraction $f^{b\bar{b}}$ is defined in the same manner. NLO QCD is found to give a good description of the data, as shown by comparison with the ZM-VFNS prediction from the H1 PDF 2000 fit.

6.3 Quark-Antiquark Tag Analyses

Events in which both heavy quarks are identified are of particular interest for the study of final state configurations. These 'two-quark tag' events provide access to new tests of higher order QCD effects. For instance, in the photon-gluon rest frame the angle between the heavy quarks is $180°$ in the leading order picture, but in next-to-leading order it can deviate significantly due to hard gluon radiation. In the k_t factorization approach. the $q\bar{q}$ pair is expected to be sensitive to possible transverse momenta k_t of the gluons entering the quark pair production process.

Figure 36: Definition of the correlation regions in terms of $\Delta\Phi$ and the relative charges of the D^* meson and the muon. The sketches illustrate the $\Delta\Phi - \Delta Q$ correlations in $c\bar{c}$ and $b\bar{b}$ quark decays to $D^*\mu$.
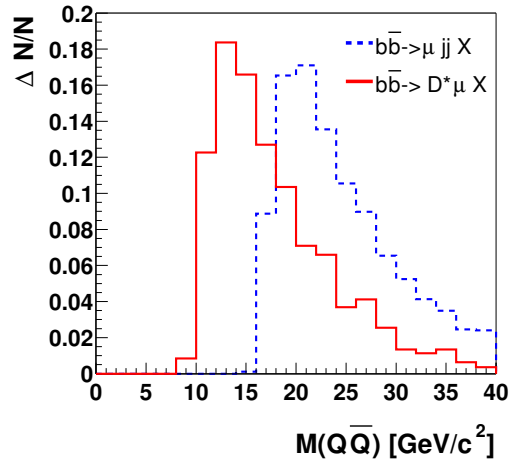

Figure 37: Distribution of the invariant mass $M(Q\bar{Q})$ of the quark pair as simulated in Pythia for the selected sample of $D^*\mu$ events (solid line) and for the selection of the beauty enriched di-jet event sample in which two jets at transverse momenta of 6 and 7 GeV are required in addition to a muon (see section 6.2.1).

		Cross section [pb]
H1 Charm	Data	$250 \pm 57 \pm 40$
	PYTHIA (direct)	$242(142)$
	CASCADE	253
	FMNR	286^{+159}_{-59}
H1 Beauty	Data	$206 \pm 53 \pm 35$
	PYTHIA (direct)	$57(44)$
	CASCADE	56
	FMNR	52^{+14}_{-9}
ZEUS Beauty	Data	$214 \pm 52(stat.)^{+96}_{-84}(syst.)$
	PYTHIA (direct)	80
	HERWIG	38

Table 4: Measured $D^*\mu$ cross sections for charm and beauty production in comparison with results from theory predictions.

Furthermore, in semileptonic decays the charge of the final state lepton in combination with the relative angle to the reconstructed charm hadron can be used to separate charm and beauty contributions to the heavy quark cross section.

6.3.1 $D^*\mu$ Correlations

ZEUS and H1 have performed analyses of $D^*\mu$ correlations [47, 48] in which the D^* is reconstructed in the decay $D^{*\pm} \rightarrow D^0\pi^\pm \rightarrow (K^\mp\pi^\pm)\pi^\pm$. The separation of charm and beauty production exploits the charge and azimuthal angle correlations of the D^* meson and the muon. Four different correlation regions are defined which are populated differently by charm and beauty events (see fig. 36), thus allowing to separate the cross section contributions from charm and beauty quark pairs.

In the approximation in which the directions of the D^* meson and the muon are identified with those of the quark and antiquark, only one correlation is possible for $c\bar{c}$ pairs, and the events populate region IV. In contrast, beauty events populate regions II,III, and IV depending on whether the muon originates from the same b quark as the D^* or from the opposite $\bar{b}$. The correlations for the D^* and the muon are smeared out by the leptonic decay spectrum and by fragmentation effects. Higher order QCD effects like gluon radiation and/or an initial transverse momentum of the gluon should also be visible. Possible physics backgrounds come from $B^0\bar{B}^0$ mixing and Cabibbo suppressed decays $b \rightarrow cW^-$, $W^- \rightarrow \bar{c}s$. Experimentally, background contributions originate from events with fake D^* mesons, i.e. from combinatorial background, or from fake muons.

Monte Carlo simulations are used to account for smearing effects and backgrounds. The normalization of the combinatorial background is fitted using right and wrong charge combinations of the D^0 decays in each region separately. Here, wrong charge combinations are given by $D^{*\pm} \rightarrow (K^\pm\pi^\mp)\pi^\pm$. The relative fractions of beauty and charm are then extracted from a fit to the four correlation regions.
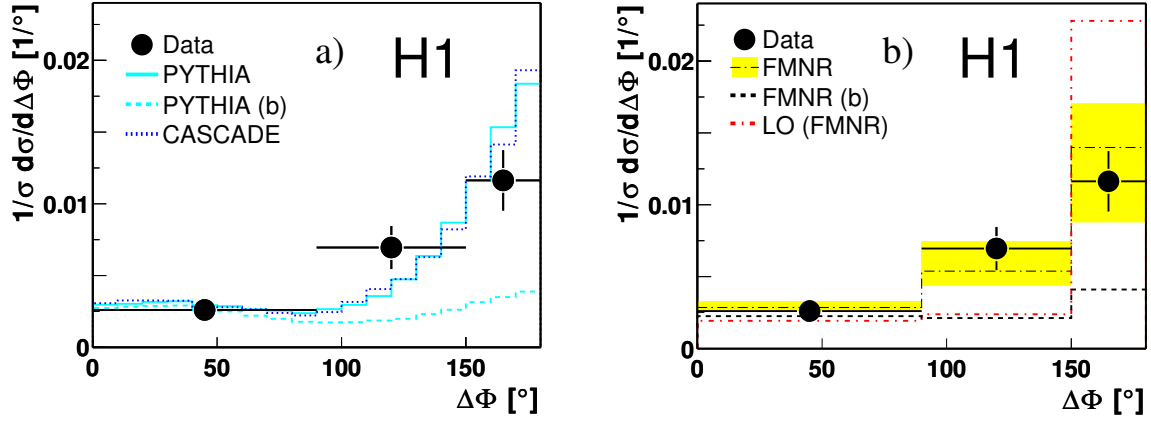
Figure 38: Normalized differential $D^*\mu$ cross sections for the azimuthal angle difference $\Delta\Phi$ between the muon and the D^* meson. The data are compared with predictions from a) the LO+PS Monte Carlo generators Pythia and Cascade and b) with LO and NLO predictions from the FMNR program.

The analysis does not depend on the reconstruction of jets and is thus capable of accessing a kinematic region of lower invariant masses $M(Q\bar{Q})$ than the measurements of the beauty cross section for events with jets in the final state (see fig. 37).

The normalized differential cross section of the $D^*\mu$ sample is compared with LO+PS predictions from Pythia and Cascade (fig. 38a) and with predictions from FMNR at LO and at NLO (fig. 38b). The data show the expected deviations from the LO calculations due to higher order effects: the observed $\Delta\Phi$ peak around $180°$ is broader than the LO computation. The data are in good agreement with the NLO calculation and also with PYTHIA and CASCADE. Although different approaches are used in PYTHIA and CASCADE to compute the evolution of the partons from the proton and the hard interaction, the differences between the two simulations are smaller than the experimental errors.

The visible beauty and charm cross sections as measured using $D^*\mu$ correlations by H1 [47] and by ZEUS [48] are compared with theory predictions. The results are listed in table 4 and are also shown in fig. 40. Comparison of the measurement with the theory predictions shows that the beauty cross sections extracted from the $D^*\mu$ data are consistently higher by roughly a factor 3 to 4 than the expectations from theory. In contrast, the corresponding charm cross sections are generally well described by theory.

6.3.2 $\mu\mu$ Correlations

The ZEUS experiment has measured the beauty cross section, using a sample of events in which the two muons are identified in the pseudo-rapidity range $-2.2 < \eta < 2.5$ [42]. The analysis provides almost full rapidity coverage and thus gives access to a direct measurement of the total beauty cross section. The beauty cross section is extracted from the like-sign and unlike-sign subsamples by adjusting the beauty contribution in the Monte Carlo simulation such that the normalization of the data is recovered. The normalization of the unlike-sign charm background
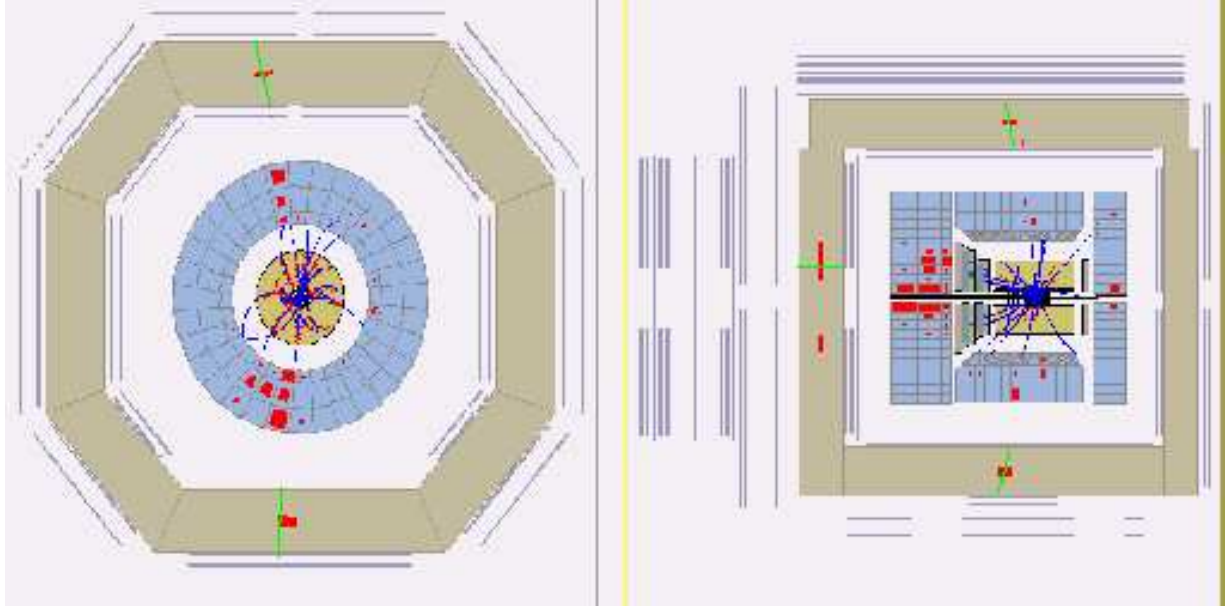
Figure 39: Candidate of an event with beauty quarks which both decay into muons in the ZEUS detector.

is fixed to the results from the corresponding measurements. It is assumed that the background from light-quark events is the same in the like-sign and unlike-sign samples.

The results of the various measurements of beauty production at HERA are shown in fig. 40. In this figure the ratios between the measured cross section and the predictions from the fixed order massive calculations in perturbative QCD are depicted. All the measurements are in reasonable agreement within the errors. Note that the kinematic region of the various measurements can differ drastically.

6.4   Charmonium Production

A special case of charm fragmentation is charmonium production where the two charm quarks combine to form a colorless hadron. Like open charm production, charmonium production at HERA occurs dominantly through photon-gluon fusion: a photon emitted from the incoming electron or positron interacts with a gluon from the proton to produce a $c\bar{c}$ pair that subsequently forms a charmonium state. Comprehensive reports on the physics of charmonium production are available [165, 166].

In this section the measurements of the production rates and polarization states of J/ψ and $\psi(2S)$ mesons from H1 and ZEUS (see table 5) are described.

6.4.1   Inelastic Photoproduction of Charmonium

Many models have been suggested to describe inelastic charmonium production in the framework of perturbative QCD, such as the color-singlet model (CSM) [167–170], the color-eva-
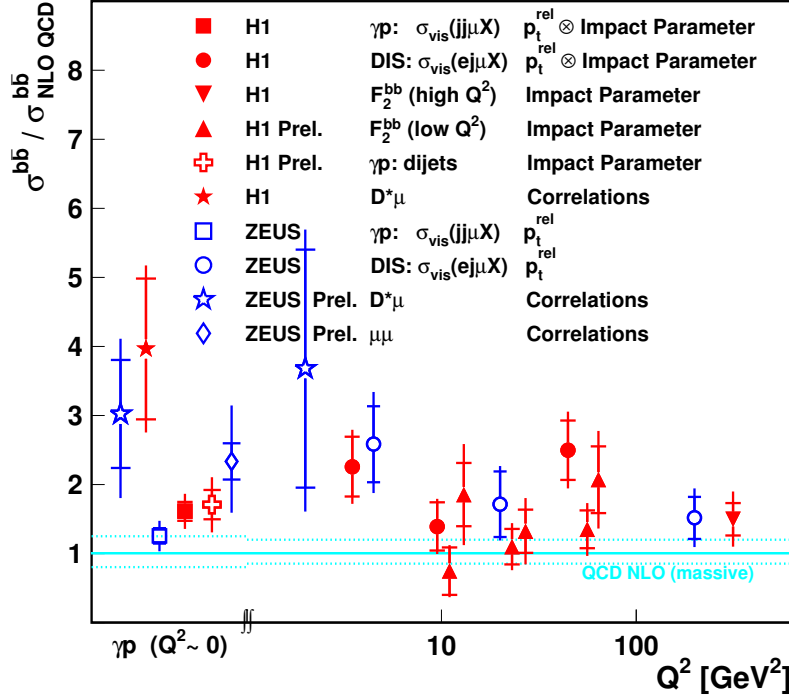
Figure 40: Summary of beauty measurements at HERA. The ratio of the cross sections to the predictions from the programs FMNR (HVQDIS) is shown. The open points and squares refer to the measurements with jets and muons (see fig. 33), the stars correspond to the measurements using $D^*\mu$ correlations. The horizontal position of the photoproduction measurements, at $Q^2 < 1\,\mathrm{GeV}^2$, is chosen arbitrarily for better visibility.

	Analysis	Data	Kinematic Region				
			Q^2 [GeV^2]	$W_{\gamma p}$	$p_{t,\psi}^2$ [GeV]	$z_{J/\psi}$	$Y_{\psi,lab}$ (Rapidity)
H1							
[27]	J/ψ in γp	1994	< 4	50...150		0.45...0.9	
[28]	J/ψ in DIS	95-97	2...80	40...180		0.2...1.0	
[29]	J/ψ in γp	96-00	< 1	60...260	1...60	0.05...0.9	
[30]	J/ψ in DIS	97-00	2...100	50...225	> 1	0.3...0.9	
ZEUS							
[31]	J/ψ in γp	1994	< 4	$50 - 180$	> 1	0.4...0.9	
[32]	J/ψ and $\psi(2S)$ in γp	96-97	< 1	50...180		0.1...0.9	
[33]	J/ψ in DIS	96-00	2...80	50...250		0.2...0.9	$-1.6...1.3$
[34]	J/ψ in γp polarization	96-00	< 1	50...180	> 1	0.1...0.9	

Table 5: Overview of the measurements of inelastic charmonium production at H1 and ZEUS.
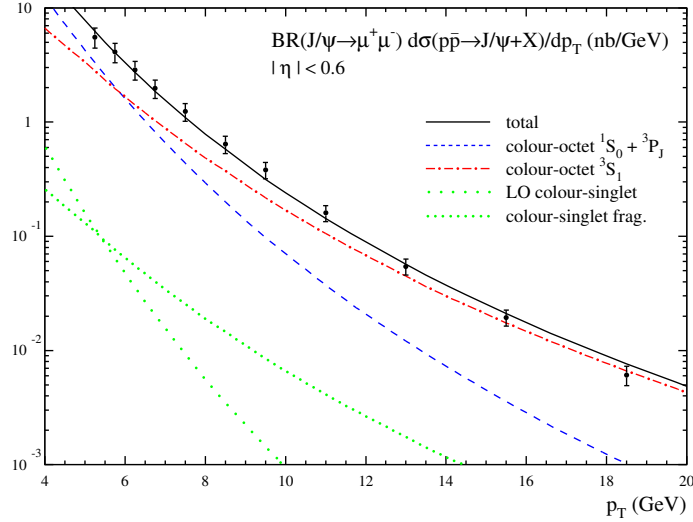
Figure 41: Differential cross sections for the production of direct J/ψ at the Tevatron as a function of p_t. The data points are CDF measurements from Run I [191, 192]. The dotted curves are the CSM contributions. The solid curves are the NRQCD factorization fits, and the other curves are individual color-octet contributions to the fits (taken from [165]).

poration model [171, 172] and soft color interactions [173]. Most recently the ansatz of non-relativistic quantum chromodynamics (NRQCD) factorization was introduced in which colour octet $c\bar{c}$ states contribute to the charmonium production cross section.

Theoretical calculations based on the NRQCD factorization approach [174–176] are available in leading order [177–182]. In the NRQCD factorization approach the size of the color octet contributions, which are described by long distance matrix elements (LDME), are additional free parameters and have been determined in fits to the Tevatron data [183]. The NRQCD factorization approach contains the color singlet model which is recovered in the limit in which the long distance matrix elements tend to zero.

For J/ψ and $\psi(2S)$ photoproduction, the CSM calculations are available including next-to-leading order contributions [184, 185]. Alternatively, using the CSM, inelastic J/ψ production can be modeled in the k_t factorization approach (see section 2.5) using an unintegrated (k_t dependent) gluon density in the proton [186, 187, 190].

Figure 41 shows data from CDF [191, 192] together with CSM calculations to leading order and fitted color octet contributions. It can be seen that the color octet contributions are large, leading to a good description of the data. Unfortunately those long distance matrix elements which are most important in J/ψ and $\psi(2S)$ photoproduction at HERA, are not well constrained by the Tevatron data and thus contain large uncertainties [165]. The new charmonium results from the Tevatron Run-II (see e.g. fig. 7) which provide much more statistics and extend to lower values of $p_{t,\psi}$ could help to reduce the uncertainties of the LDME significantly.

It should be noted that next-to-leading-order corrections might change the size of the color octet contributions substantially. Although the NLO terms have not been calculated in the NRQCD approach, effects that are similar to those in the CSM may be expected, in which the
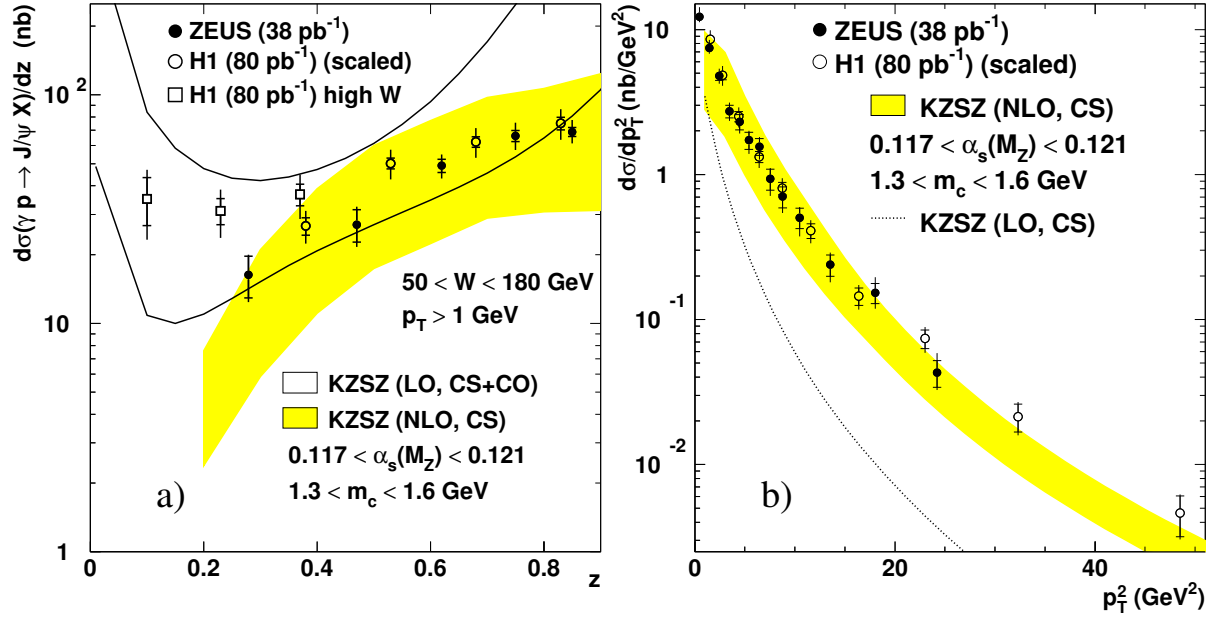
Figure 42: The rate for inelastic J/ψ photoproduction at HERA as a function of a) z and b) $p_{t,\psi}$. The open band represents the LO NRQCD factorization prediction [165]. The shaded band represents the NLO color-singlet contribution [165, 185]. The dotted line in b) denotes the LO color-singlet contribution. The data points are from the H1 [29] and ZEUS [32] measurements.

NLO terms lead to an increase in the cross section of typically a factor two, with a strong $p_{t,\psi}$ dependence.

Figure 42 shows the measurements of the J/ψ cross section by the H1 collaboration [29] and the ZEUS collaboration [32], compared with the theoretical predictions given in Ref. [165]. The variable z denotes the fraction of the photon energy in the proton rest frame that is transferred to the J/ψ and is defined as

$$z = \frac{(E - p_z)_{J/\psi}}{(E - p_z)_{\text{hadrons}}}, \tag{10}$$

where E and p_z in the numerator are the energy and z-component of the momentum of the J/ψ and E and p_z in the denominator are the sums of the energies and z-components of the momenta of all the hadrons in the final state.

The J/ψ data are not corrected for feeddown processes from diffractive and inelastic production of $\psi(2S)$ mesons ($\approx 15\%$), the production of b hadrons with subsequent decays to J/ψ mesons, or feeddown from the production of χ_c states. The latter two contributions are estimated to contribute between 5% at medium z and 30% at the lowest values of z.

The open band in fig. 42 represents the sum of the color-singlet and color-octet contributions, calculated in leading order NRQCD. The uncertainty is due to the uncertainty in the color-octet NRQCD matrix elements. The shaded band shows the calculation of the color-singlet contribution to next-to-leading order in α_s [184, 185] which describes the data quite well without the inclusion of a color-octet contribution. The next-to-leading-order QCD corrections are crucial in describing the shape of the transverse-momentum distribution of the J/ψ.
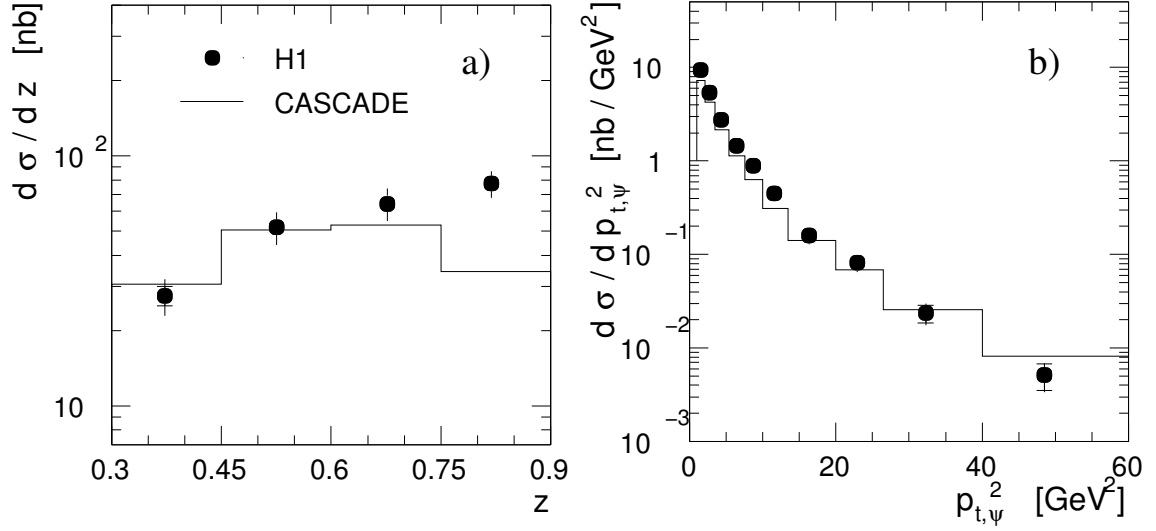
57

Figure 43: Inelastic J/ψ production in the region $60 < W_{\gamma p} < 240$ GeV, $0.3 < z < 0.9$, and $p_{t,\psi}^2 > 1$ GeV^2, in comparison with a k_t factorization model implemented in the Monte Carlo generator CASCADE [188, 189]. In a) the differential cross section $d\sigma/dz$ is shown and in b) $d\sigma/dp_{t,\psi}^2$ in the range $0.3 < z < 0.9$.

The k_t factorization approach [187–190] has been applied for J/ψ production [186]. Figure 43 shows a comparison of the data with the predictions from the k_t factorization approach as implemented in the Monte Carlo generator CASCADE. Good agreement is observed between data and predictions for $z \lesssim 0.8$. At high z values, the CASCADE calculation underestimates the cross section. The CASCADE predictions for the the $p_{t,\psi}^2$ dependence of the cross section (fig. 43c) fit the data considerably better than the collinear LO calculations (dotted curve in fig. 42b). This improved fit is attributed to the transverse momentum of the gluons from the proton, which contribute to the transverse momentum of the J/ψ meson.

The polarization of the J/ψ meson is expected to differ in the various theoretical approaches discussed here and could in principle be used to distinguish between them, independently of normalization uncertainties. The general decay angular distribution can be parameterized as

$$\frac{d\Gamma(J/\psi \to \ell^+\ell^-)}{d\Omega} \propto 1 + \lambda \cos^2\theta + \mu \sin 2\theta \cos\phi + \frac{\nu}{2}\sin^2\theta \cos 2\phi, \qquad (11)$$

where θ and ϕ refer to the polar and azimuthal angle of the three-momentum of the positive lepton with respect to a coordinate system that is defined in the J/ψ rest frame [178]. The parameters λ, μ, ν can be calculated within NRQCD or the CSM as a function of the kinematic variables, such as z and $p_{t,\psi}$.

In fig. 44, the data are shown, together with the results from two LO calculations: the NRQCD prediction, including color-octet and color-singlet contributions [178], and the color-singlet contribution alone. In contrast to the predictions shown in fig. 44, in which λ is zero or positive, the prediction of the k_t factorization approach is that λ should become increasingly negative toward larger values of $p_{t,J/\psi}$, reaching $\lambda \sim -0.5$ at $p_{t,\psi} = 6$ GeV. However, at present, the errors in the data preclude any firm conclusions. In order to distinguish between full NRQCD and the color-singlet contribution alone, measurements at larger $p_{t,\psi}$ are required. The

58

Figure 44: Polarization parameters λ (left panels) and ν (right panels) in the target rest frame as functions of z (top panels) and $p_{t,\psi}$ (bottom panels). The error bars on the data points correspond to the total experimental error. The theoretical calculations shown are from the NRQCD approach [178] (shaded bands) with color-octet and color-singlet contributions, while the curves show the result from the color-singlet contribution separately.
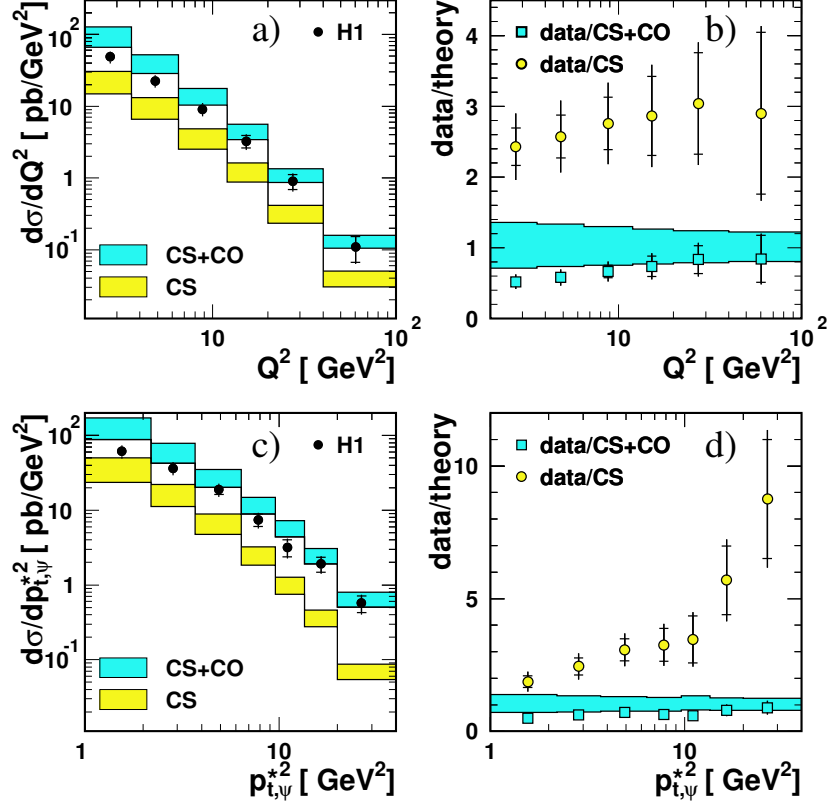
Figure 45: Differential cross sections a) $d\sigma/dQ^2$ and c) $d\sigma/dp^{*2}_{t,\psi}$ and the corresponding ratios of data to theory (b and d). The data from H1 [30] are compared with the NRQCD calculation [193] (CO+CS, dark band) and the color-singlet contribution [193] (CS, light band).

measured values of ν, for which no prediction is available from the k_t factorization approach, slightly favor the full NRQCD prediction.

In conclusion, it should be noted that calculations to next-to-leading order, which are not yet available in the framework of NRQCD factorization, could be an essential ingredient in a full quantitative understanding of charmonium production at HERA, and also at other experiments, such as those at the Tevatron.

6.4.2 Inelastic Electroproduction of Charmonium

The analysis of leptoproduction at finite Q^2 has experimental and theoretical advantages in comparison with the analysis of photoproduction. At high Q^2, theoretical uncertainties in the models decrease and resolved-photon processes are expected to be negligible. Furthermore, the distinct signature of the scattered lepton makes the inelastic process easier to detect. However, due to the steeply falling Q^2 dependence the data are more limited statistically.

The cross section for J/ψ production in deep-inelastic ep scattering at HERA was calculated in the NRQCD factorization approach at leading order in α_s taking into account diagrams of the type "2 → 2" [193] using the matrix elements as determined in [183] and the MRST98LO [73]
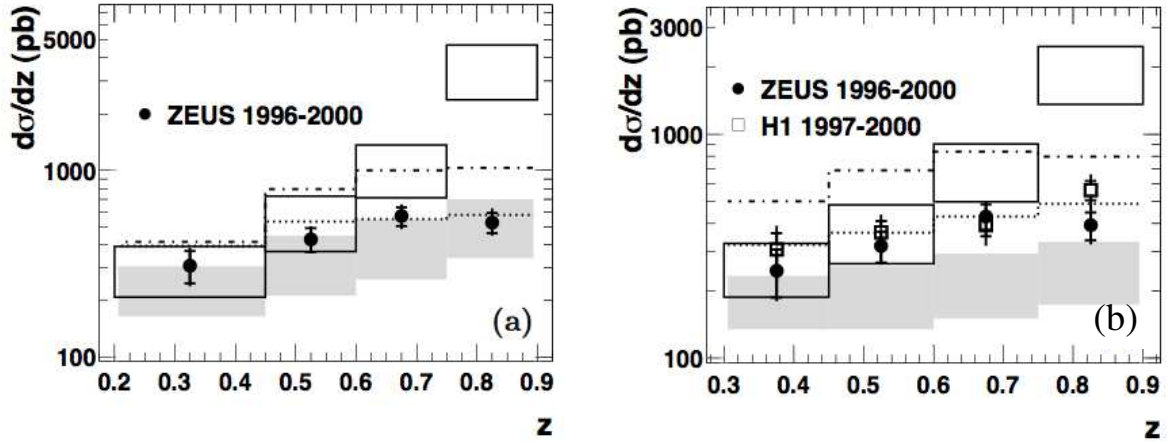
Figure 46: Differential cross section $d\sigma/dz$ a) without and b) with a cut on $p_{t,\psi}^{*2} > 1$ GeV. The data from ZEUS [33] and in b) also H1 [30] are compared with the NRQCD calculation [193] (CS+CO, open band), the color-singlet contribution (CS, shaded band), with a prediction in the k_t factorization approach assuming the CSM [190] (dotted line) and with the Monte Carlo generator CASCADE (dash-dotted line).

and CTEQ5L [72] parton distributions. In fig. 45, the results of this calculation are plotted as a function of Q^2 and $p_{t,\psi}^{*2}$, along with the H1 data [30]. The NRQCD results that are shown in fig. 45 include the contributions from the color-octet channels ${}^3S_1$, ${}^3P_{J=0,1,2}$, ${}^1S_0$, as well as from the color-singlet channel ${}^3S_1$. The contribution of the color-singlet channel is also shown separately. The values of the NRQCD matrix elements were determined from the distribution of transverse momenta of J/ψ mesons produced in $p\bar{p}$ collisions [183]. The bands include theoretical uncertainties, which originate from the uncertainty in the charm-quark mass $m_c = 1.5 \pm 0.1$ GeV, the variation of renormalization and factorization scales by factors 1/2 and 2, and the uncertainties in the NRQCD matrix elements, all of which result mainly in normalization uncertainties that do not affect the shapes of the distributions.

Figure 46 shows the differential electroproduction cross sections for J/ψ mesons from ZEUS [33] and H1 [30] as function of z. The data are compared with predictions in the framework of NRQCD (NRQCD) [193] and also with predictions in the k_t factorization approach in which only the color-singlet contribution (CS) is included [104, 190]. The uncertainties in the NRQCD calculations are indicated in fig. 46 as bands. The agreement with the color singlet model (CS), seen in fig. 46a, deteriorates when the cut $p_{t,\psi}^{*2} > 1$ GeV is applied (fig. 46b). This cut is justified, however, as towards small $p_{t,\psi}^{*2}$, perturbation theory becomes increasingly unreliable due to collinear singularities for the contributions $e + g \rightarrow e + c\bar{c}[n] + g$ with $n={}^1S_0^{(8)}$ and ${}^3P_J^{(8)}$ [193].

6.4.3 Diffractive Charmonium Production

At HERA, the dominant production channel for quarkonia with quantum numbers of real photons (i.e. $J^{PC} = 1^{--}$) is through diffractive processes. In perturbative QCD, the diffractive
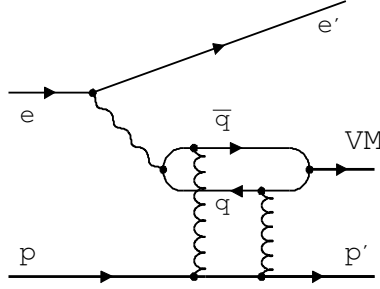
61

Figure 47: Diagram for diffractive charmonium production via exchange of two gluons in a color-singlet state.

production of vector mesons can be modeled in the proton rest frame by a process in which the photon fluctuates into a $q\bar{q}$ pair at a long distance from the proton target. The $q\bar{q}$ subsequently interacts with the proton via a color-singlet exchange, i.e. in lowest order QCD via the exchange of a pair of gluons with opposite color (see fig. 47) [194–200]. At small $|t|$, where t is the momentum-transfer-squared at the proton vertex, the elastic process dominates, in which the proton stays intact. Toward larger values of $|t|$, the dissociation of the proton into a small-invariant-mass baryonic state becomes dominant. Measurements of diffractive vector-meson production cross sections and helicity structure from the H1 [28, 201–208] and ZEUS [209–217] collaborations are available for ρ^0, ω, ϕ, J/ψ, ψ', and Υ production, spanning the ranges of $0 \simeq Q^2 < 100\,\text{GeV}^2$, $0 \simeq |t| < 20\,\text{GeV}^2$, and $20 < W_{\gamma p} < 290\,\text{GeV}$. ($W_{\gamma p}$ is the γp center-of-mass energy.) In Figure 48, the elastic photoproduction cross sections are shown. Perturbative calculations in QCD are available for the kinematic regions in which at least one of the energy scales μ^2 (i.e. Q^2, M_V^2 or $|t|$) is large and the strong-coupling constant $\alpha_s(\mu^2)$ is small [218–224].

In the presence of such a 'hard' scale, QCD predicts a steep rise of the cross section with $W_{\gamma p}$. At small Q^2, $|t|$ and meson masses M_V, vector-meson production is known to show a non-perturbative 'soft' behavior that is described, for example, by Regge-type models [225–229]. Toward larger values of $|t|$, in the leading logarithmic approximation, diffractive J/ψ production can be described by the effective exchange of a gluonic ladder. At sufficiently low values of Bjorken-x (i.e. large values of $W_{\gamma p}$), the gluon ladder is expected to include contributions from BFKL evolution [61–64, 230], as well as from DGLAP evolution [59, 231].

The elasticity variable z defined in equation (10) is often used to demark the boundary between the elastic and inelastic regions, with a typical demarcation for J/ψ production being $z > 0.95$ for the diffractive region and $z < 0.95$ for the inelastic region. However, at large z, there is actually no clear distinction between inelastic J/ψ production and diffractive J/ψ production in which the proton dissociates into a final state with large invariant mass, owing to the fact that the two processes can produce the same final-state particles. In the region of large z, both inelastic (section 6.4.1) and diffractive production processes are expected to contribute to the cross section. At the same time, calculations in perturbative QCD that assume a diffractive color-singlet exchange are capable of describing the production cross sections at large z [207, 214, 215]. A unified description in QCD of the large z region, taking into account both inelastic and diffractive contributions, is yet to be developed.
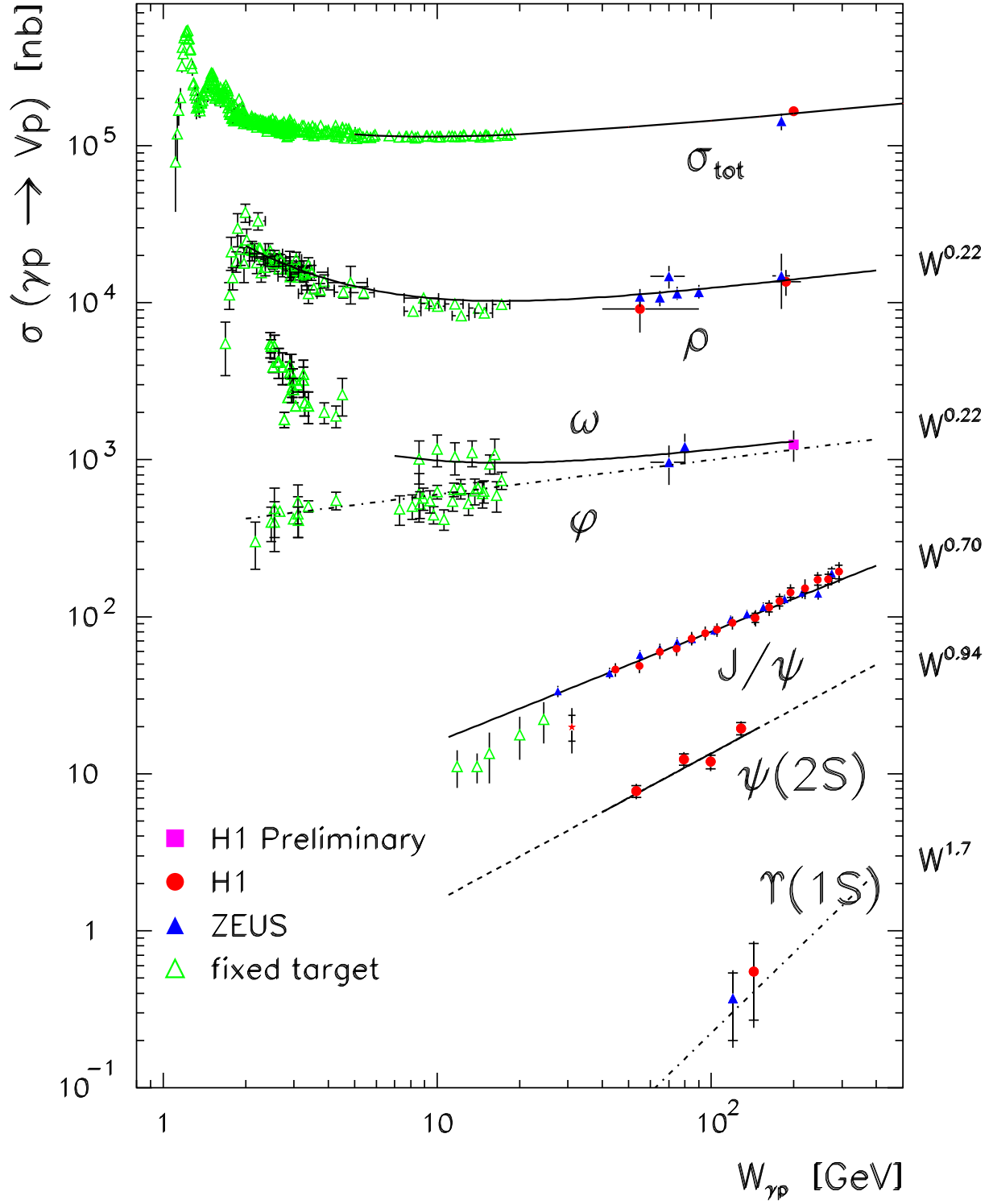
Figure 48: Total cross section and cross sections for production of various vector mesons in γp collisions as a function of $W_{\gamma p}$, as measured at HERA and in fixed-target experiments.
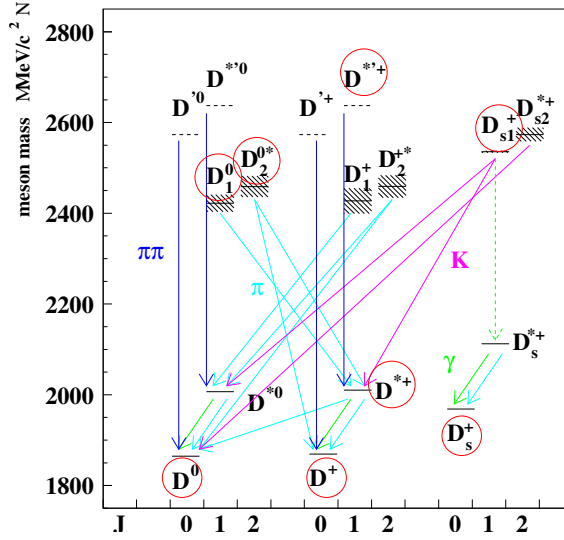
Figure 49: Overview of the known D-Meson states. The three columns show the states with $\bar{u}$, $\bar{d}$ and $\bar{s}$ for angular momenta $J = 0, 1, 2$, respectively. The circles indicate those states which have been studied so far at HERA.

6.5 Spectroscopy

The large sample of fully reconstructed charm events at HERA (as illustrated e.g. in the size of the D^* signal shown in fig. 11) opens opportunities for the study of excited charm states and also for searches for as yet unmeasured states.

6.5.1 Studies of Charm Decays

In fig. 49 the various D-meson states are shown. ZEUS has reconstructed the resonances D_1^0 and D_2^{*0} in the decays into $D^{*\pm}\pi^{\mp}$ (fig. 50a) [49]. The fraction of $D^{*\pm}$ mesons produced in decays from D_1^0 and D_2^{*0} was determined to be at the level of 3.4 and 1.4%, respectively. In the same analysis, the production rate of $D^{*\prime\pm}$ mesons in charm fragmentation was determined to be less than 0.7% (95%C.L.). ZEUS also measured the production of the excited charm-strange meson $D_{s1}^{\pm}(2536)$ using its decays into the final state $D^{*\pm}K_S^0$ [50]. In fig. 50b the invariant mass distribution of $D^{*\pm}K_S^0$ candidates is shown. The fraction of c quarks hadronizing as $D_{s1}^{\pm}$ mesons was determined to be $f(c \to D_{s1}^+) = 1.24 \pm 0.18(stat.)^{+0.08}_{-0.06}(syst.) \pm 0.14(BR)$.

6.5.2 Searches for New States

Since the year 2003 several experiments have reported the observation of a narrow resonance in the K^+n channel at mass values around 1540 MeV [232]. The minimal constituent quark content of such a state is $uudd\bar{s}$. These measurements, supported by similar observations in the K_S^0p channel [233], were interpreted as evidence for a pentaquark state. ZEUS performed searches for resonances decaying into K_S^0p [53] and found a signal of around 1520 MeV which has a probability of being a statistical fluctuation of the background of $6 \cdot 10^{-6}$. No signal was

Figure 50: The distributions of a-c) $M(D^*\pi)$ and d) of $\Delta M^{ext} + M(D^{*+})_{PDG} + M(K^0)_{PDG}$. Here, $M^{ext} = M(K\pi\pi_s\pi_3\pi_4) - M(K\pi\pi_s) - M(\pi_3\pi_4)$ and $M(D^{*+})_{PDG}$ and $M(K^0)_{PDG}$ are the nominal masses of the D^{*+} and K^0_S, respectively.

Figure 51: $M(D^*p)$ distribution from opposite-charge D^*p combinations, compared with the results of a fit in which both signal and background components are included (solid line) and with the results of a fit in which only the background component is included (dashed line).

found for the final state $\Xi\pi$ [54]. In analogy a charmed pentaquark state, with minimal quark contents $uudd\bar{c}$ as predicted in [234] might lead to an observable signal in the D^*p invariant mass combination. H1 [51] and ZEUS [52] have investigated their data for signals and found different results.

H1 reports evidence for a resonance observed when studying the invariant mass combinations of D^{*-} ($d\bar{c}$) with protons (uud) and 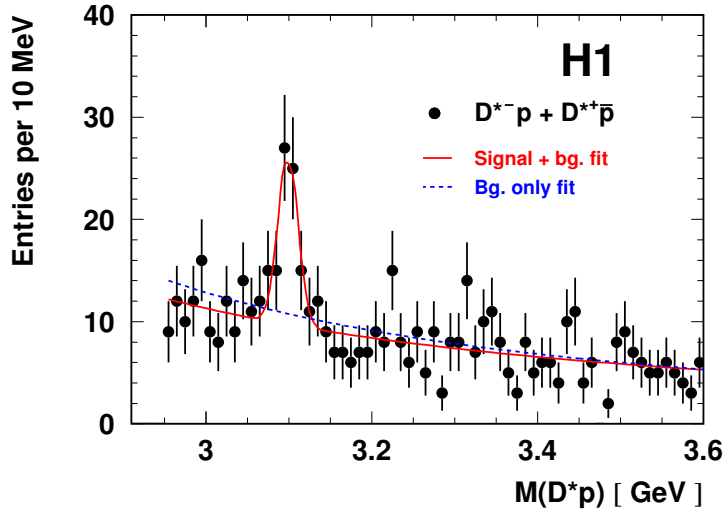the anti-matter equivalent, D^{*+} mesons with anti-protons. A strong signal is observed at a mass of 3099 +/- 6 MeV, containing roughly equal contributions from $D^{*-}p$ and $D^{*+}\bar{p}$ combinations above a moderate background (fig. 51). The resonance, corresponding to a minimal quark composition $uudd\bar{c}$ is produced along with other particles in DIS events. The fraction of events in the resonance peak compared to the number of D^* events is about 1%. The probability that a background of $N_b = 51.7$ events fluctuates to produce at least the number of events in the signal is $4 \cdot 10^{-8}$, assuming Poisson statistics. This number corresponds to 5.4 σ when expressed as an equivalent number of Gaussian standard deviations.

ZEUS has performed a similar analysis and found no indication for a signal [52]. An upper limit on the fraction of $D^{*\pm}$ mesons originating from a resonance decay in the mass region around 3.1 GeV was calculated to be around 0.25%. There is hope that the apparent contradiction between the two experiments will be resolved with improved statistics and a more detailed analysis of the properties of the observed signal.

7 Measurements with HERA-II Data

The analysis of the HERA-I data has led to a tremendous increase in the understanding of the mechanisms of heavy quark production in ep and γp scattering. In general, perturbative QCD has been proven to give reliable predictions. Experimentally, the HERA-I data are well understood and a large number of the important analyses have been performed and published or are in the process of being finished.

With HERA-II, the instantaneous luminosity has been increased by roughly a factor of 3 and the size and statistical precision of the data samples will be significantly improved. Furthermore a number of detector upgrades have been performed which open opportunities for new measurements in yet unexplored kinematic regions and will help reduce the systematic uncertainties. It is expected that the HERA-II data sample for heavy quark physics will be of order 500 pb^{-1}.

The main physics goals of Heavy Quark physics at HERA-II are

- to complete the picture of heavy quark production to large values of p_t and Q^2, i.e. to gain statistics in regions in which both the charm and beauty masses are small in comparison to p_t or Q^2 and massless models are expected to hold.

- to perform double differential measurements, allowing to study the differences between data and theory in detail.

- to cross check the results obtained with charm with precision measurements of beauty production.

- to extend the kinematic reach into the forward region. This is the kinematic region in which the largest differences between the data and the theory have been found. New and upgraded forward detectors will allow for measurements up to larger values of rapidity.

- to exploit more decay channels, e.g. by use of the new silicon detectors and larger statistics.

- to search for new states and to verify the findings of possible new states of HERA-I.

In the following the new detector components most relevant to heavy quark physics are described and possible future measurements are discussed.

7.1 New Instrumentation and Trigger Electronics

Both H1 and ZEUS have been equipped with new tracking devices in the forward direction and with additional silicon detectors, providing refined possibilities for lifetime tagging. In addition the triggering capabilities have been improved in order to cope with the increased rates of signal and background events. Furthermore a number of new software tools have been put in place which are designed to allow for a faster turn-around for physics analyses.
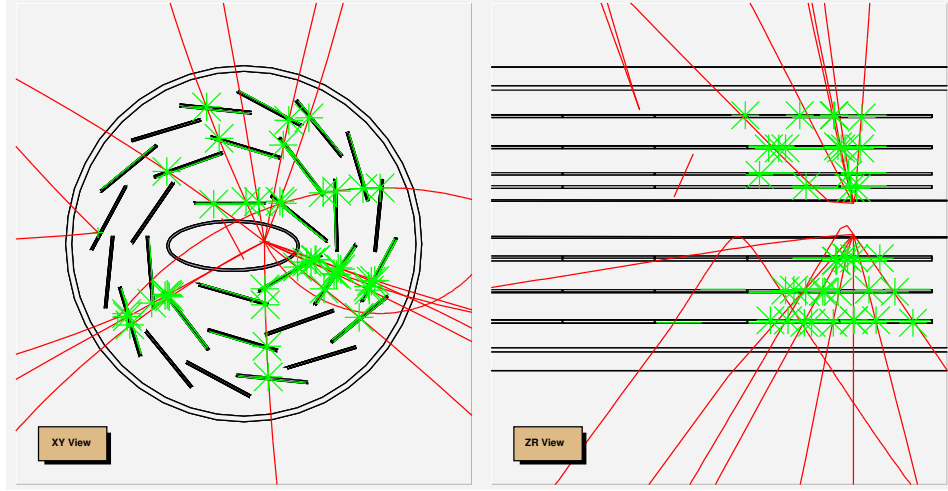
Figure 52: Display of the barrel of the ZEUS Microvertex Detector (MVD) in the r-ϕ and r-z view (taken from [235]).

7.1.1 The ZEUS Micro-Vertex Detector

The ZEUS experiment has installed a silicon detector for the HERA-II running period. In fig. 52 a sketch of the barrel region of the ZEUS micro vertex detector (MVD) is shown [235]. The barrel detector is made up of three layers each consisting of two single sided silicon strip wavers glued together back-to-back with perpendicular strip orientation. It provides a hit resolution of 7.5 μm and a hit efficiency of larger than 95%. The barrel detector is complemented with a forward micro-vertex detector which consists of 4 planes (wheels) perpendicular to the beam axis. The MVD system provides a polar angular coverage for charged tracks coming from the ep interaction point between $10°$ and $150°$.

Figure 53 shows the impact parameter distribution of muon tracks in a dijet event sample recorded in the years 2003 and 2004. The solid line indicates the number of entries in the corresponding bin for negative values on the negative side of the δ distribution. The difference between the points and the solid line shows the lifetime effect. The corresponding distribution based on HERA-I data from the H1 experiment was shown in fig. 15 in section 5.5.1.

7.1.2 The H1 Forward Silicon Tracker

The new H1 Forward Silicon Tracker (FST) extends the central silicon tracker (CST), which was already used in HERA-I, into the forward direction (see fig. 54a). The FST consists of five layers of two silicon strip planes each providing u-v coordinates and two r-planes. It covers a range of polar angles between $8°$ and $16°$. The additional angular acceptance of the FST leads to an increase of the reach for charm physics in Bjorken-x as illustrated in fig. 54.

In the 2004 data, the FST was shown to have a signal hit efficiency of close to 100% and a track efficiency of larger than 95% [236]. The alignment of the device and the optimization of the reconstruction algorithms are not fully completed yet. For the analysis of charm production optimal transverse momentum resolution and impact parameter resolution are required. These
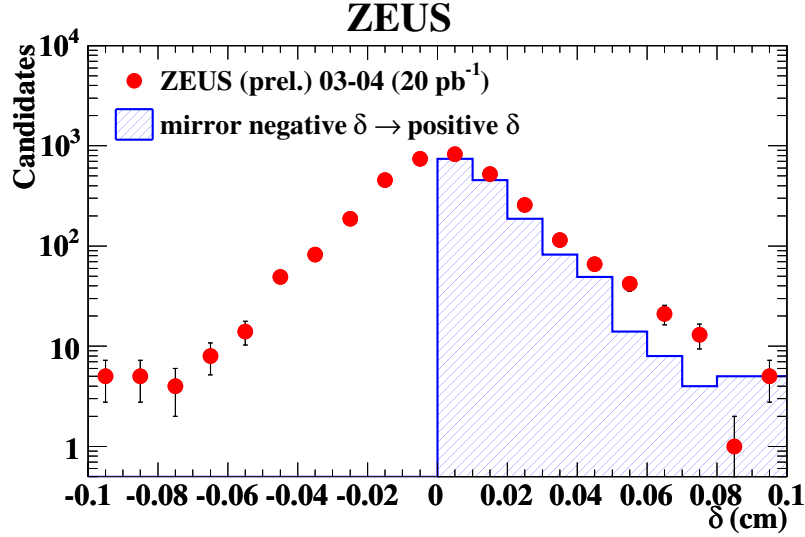
68

ZEUS

Figure 53: Impact parameter distribution of muon tracks in μ+dijet events as measured by ZEUS using data recorded in 2003 and 2004.

are limited by significant multiple scattering effects. At the end of the 2004 running period the FST was damaged by a water leak. It is planned to reimplement a reassembled FST detector, equipped with radition hard electronics, in the shutdown 2005/06.

7.1.3 Forward Track Detectors

Two new modules of Straw Tube Trackers have been implemented in the forward region of the ZEUS detector which are interleaved with the existing three sets of planar drift chamber modules. Each of the modules consists of four superlayers of straws as shown in fig. 55.

In the case of H1 five new planar drift chambers were installed each with eight wires strung perpendicular to the beam axis. Including the existing planar drift chambers up to 76 hits can be obtained for tracks going in the forward direction.

7.1.4 The ZEUS Global Trigger

ZEUS has implemented a new second level trigger based on 12 dual-CPU PCs which use tracking information from the new microvertex detector (MVD, see above), the central track detector and the new forward straw tube tracker. The mean processing time is $10 - 15$ μs at an input rate of about 300 Hz, as determined by the first level trigger.

7.1.5 New H1 Track Triggers

The H1 Collaboration has upgraded the trigger electronics (described in section 5.7) in order to be able to improve the signal to background ratio and to collect useful physics events while suppressing the triggering of events that are not of interest or are beam-related background.

69

Figure 54: a) Side view of the interaction region of the H1 detector. The three silicon strip detectors FST, CST and BST are indicated. b) Acceptance for charm events ($ep \rightarrow D^*X \rightarrow D^0\pi_s X \rightarrow K\pi\pi_s X$) for $Q^2 < 100$ GeV^2 using the central tracker and the CST (open points) and adding the FST (and the backward silicon tracker BST) with different assumptions on the acceptance range η of the D^* (full points).

Figure 55: The two new ZEUS Straw Tube Tracker modules with four superlayers each.

Figure 56: r-ϕ view of a charged particle track from the interaction point traversing the central drift chambers of the H1 experiment. The sense and cathode wires of the chambers are indicated.

The H1 Fast Track Trigger (FTT) [237] implements charged track finder and mass reconstruction algorithms in the first three levels of the H1 trigger scheme. For the charged particle track reconstruction at the first trigger level 1 (2.3 μs) and level 2 (23 μs), the FTT makes use of Field Programmable Gate Arrays (FPGA) and their embedded Content Addressable Memories (CAM). The track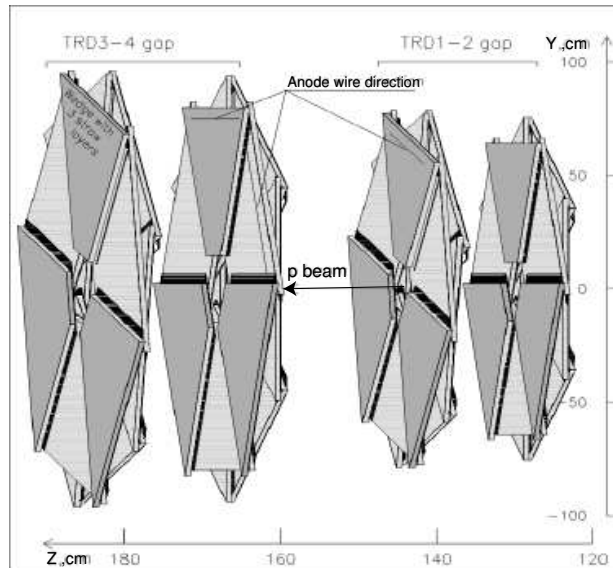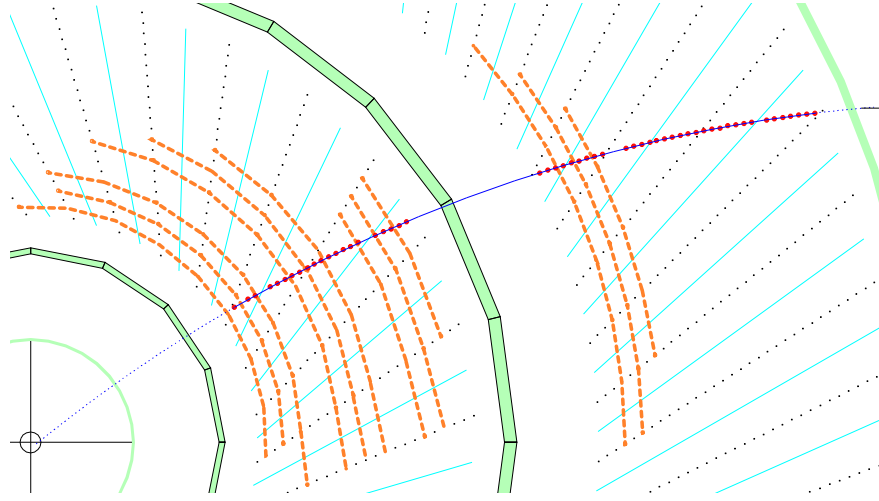 parameters are determined by comparing hit-patterns with predefined masks implemented in digital signal processors (DSP). The FTT can reconstruct up to 48 tracks which is sufficient for about 98% of the events of interest.

The FTT functionality is based on hit information in the central jet chambers CJC. In fig. 56, the geometrical cell structure of both chambers is sketched. In the first step track segments are formed separately in four groups of three layers of wires each. A fast track segment linking, based on matches of track segments in $\kappa (\propto 1/p_t)$ and ϕ is completed within 2 μs to provide level 1 trigger decisions based on charged track multiplicities and charged particle topologies for coarse p_t cuts. The result is used by the second level FTT where the track segments are linked and re-fitted to better precision within 20 μs including the determination of event quantities like a refined track multiplicity, momentum sums and invariant masses for low multiplicity events. Figure 57 shows the measured precision for FTT tracks at level 2. The resolutions are given here with respect to the full off-line reconstruction. The resolution in $1/p_t$ is approximately 2%, approximately 2 mrad in ϕ and 75 mrad in θ.

The track parameters of the fitted tracks are sent to FTT L3 where a farm of commercial processor boards is used to perform a full search for particle resonances within 100 μs. The L3 track information is either used directly or in combination with information from other trigger subsystems to generate a final L3 decision.

In addition to upgrading the drift chamber trigger, the H1 experiment has improved the robustness against severe background conditions by replacing its double layer central inner multi-wire proportional chamber by a chamber with five layers of pads with geometry projective to the z-position of the ep interactions. The new detector has ten times more channels and, like
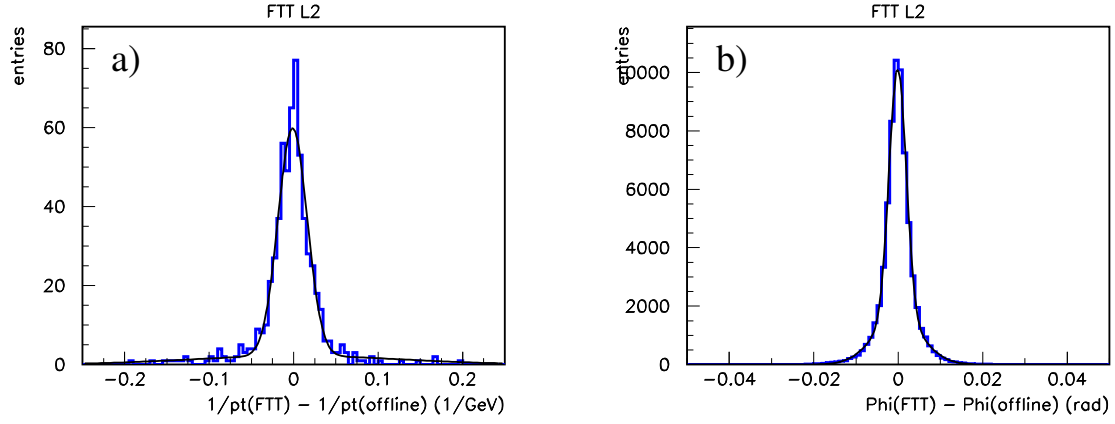
71

Figure 57: Measured resolution of the FTT algorithm at second trigger level relative to the full off-line CJC reconstruction for a) $1/p_t$ for tracks with $p_t > 500$ MeV and b) ϕ for tracks with $p_t > 100$ MeV.

the old proportional chamber, provides trigger decisions, based on a z-vertex histogramming technique, at level 1, within a latency of 2.3 μs.

7.1.6 Software Upgrades

During the shutdown between HERA-I and HERA-II, ZEUS and H1 launched a number of software upgrade projects. In this section the most prominent among these projects are briefly described.

- The H1 Collaboration has upgraded its analysis software. The new integrated object-oriented physics analysis environment is based on the RooT framework and comprises a new data storage scheme, a data access front-end, and a new event display [238]. The analysis data is stored in three layers of separate files. The upper most event summary layer (HAT) facilitates a fast selection via event classification and kinematic event quantities. At the particle level (second layer, μODS) a custom-built pointer relation (H1Pointer) allows for direct access from the particle 4-vectors to the corresponding track and cluster information which is stored at reconstruction level (ODS). The user access to the data files is encapsulated using extensions to the RooT tree classes. The framework contains information, software tools and calibrations for most of the H1 physics analysis topics, thus allowing efficient exchange of results between different analysis groups.

- ZEUS has developed a new event display program 'ZeVis' which is a distributed application and based on client-server technology [239]. On the client side, requests to the server are handled by classes embedded in RooT [240] with extensions allowing for the passing of parameters and version qualifiers. The display provides various views (2d and 3d) which can be displayed simultaneously and for collections of selected detector components. It encompasses a GUI toolkit, object inspection, and histogramming and statistics

functionality. The average response time between request of an event from the server and display on the client is less than 2s.

- In preparation of the LHC the resources of computing hardware available for high energy physics experiments are being restructured. The GRID infrastructure already contains large amounts of CPU and storage capacity which are accessible through the GRID middleware. Both H1 and ZEUS have started to use the GRID software framework for the mass production of Monte Carlo simulation event samples. The experiments have developed toolkits which contain general interfaces to the GRID services and book keeping facilities. Particular emphasis is put on the fault tolerance of the custom software as the GRID software is not yet perfect. Incomplete or corrupt jobs can be recognized by automatic job submission monitoring and output analysis tools which are able to recover most errors without human intervention. ZEUS started production running in 2004 and between November 2004 and February 2005 in excess of 60 million events were produced. H1 is in the process of launching mass production in spring 2005.

7.2 Future Measurements

7.2.1 Heavy Quark Structure Functions

The most prominent measurement of heavy quark production is the measurement of the structure functions $F_2^{c\bar{c}}$ and $F_2^{b\bar{b}}$. The HERA-I results were presented in section 6.1.2 and 6.2.2. Towards large values of Q^2 and low values of x the charm results are largely limited by statistical uncertainties while the beauty results are statistically limited everywhere. With the expected increase of integrated luminosity to a value of 500 pb^{-1} obtained in HERA-II the experimental errors are expected to shrink significantly, such that the data can provide useful constraints for global fits. In fig. 58 the expectation for the measurement of $F_2^{c\bar{c}}$ using an integrated luminosity of 200 pb^{-1} is shown. The central values of the expectation are based on an H1 measurement of the gluon density from Q^2 evolution studies of the inclusive proton structure function F_2 in next-to-leading order QCD, such as reported in [66]. The overall average precision is 10% and is systematically limited at low Q^2 and statistically limited at high Q^2. Different methods for charm and beauty tagging have been established in HERA-I which are explained in section 5, i.e. the use of reconstructed D^* mesons [2–5, 7–9, 11–19, 21, 23–26, 55–58], the use of semi-leptonic decays [36–42] and the use of lifetime tags made possible by the use of silicon vertex detectors [6, 43–46], providing superior spatial resolution close to the interaction region. For HERA-II a combination of these methods will help to further reduce the systematic and theoretical uncertainties to the level of few percent.

7.2.2 Open Charm Production

With the HERA-II luminosity and new detector components enhanced systematic precision and increased kinematic reach will be provided by both increased statistics and also by the use of the upgraded detector components described in section 7.1. The statistics can be used to reduce the statistical errors or to increase the number of measured cross section points. Figure 59 illustrates
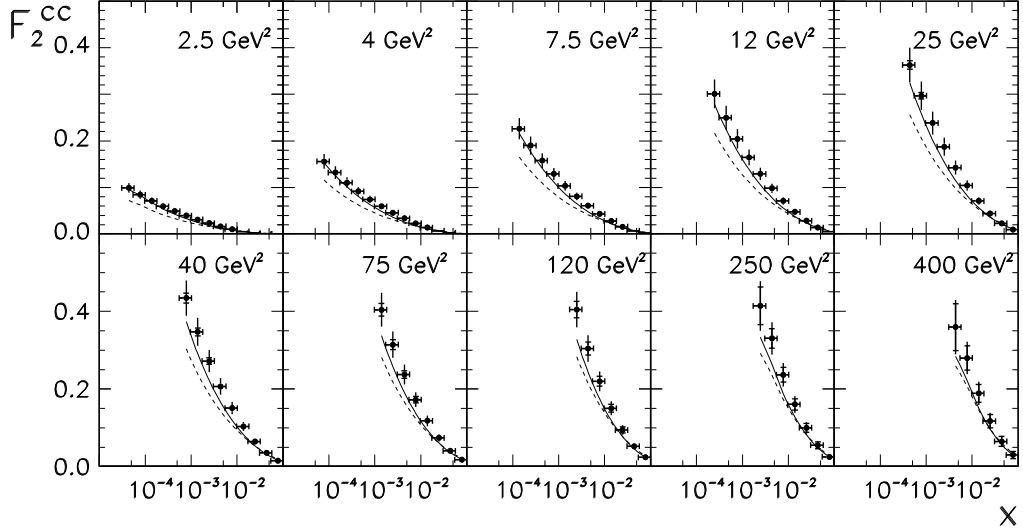
Figure 58: Result of a simulated measurement of the charm contribution $F_2^{c\bar{c}}$ to the proton structure function F_2 using 200 pb^{-1} of ep data (see text). The inner error bars are statistical, the outer error bars show the statistical and the systematical error added in quadrature. The curves refer to GRV-HO [241] and MRSH [242] predictions. The existing measurements for $F_2^{c\bar{c}}$ using HERA-I data are shown in fig.24 in section 6.1.2.

the kinematic reach for reconstructed D^* events as a function of the transverse momentum p_t of the charm quark. Double and triple-differential cross section measurements, e.g. as functions of Q^2, p_t and η, allow to probe the theoretical predictions at a deeper level and better accuracy and characteristic effects in specific regions of the phase space can be isolated.

In HERA-I, differential measurements of exclusive final states with charm (e.g. identified by the reconstruction of D-meson) were performed in the central rapidity regions ($|\eta(D^*)| <$ 1.5|) up to transverse momenta of the D^* of 20 GeV (see section 6.1.1). While the data are generally described by pQCD calculations, discrepancies of order 20% are seen among different theory predictions and with the data in particular at large transverse momenta and in the forward direction.

This is illustrated in fig. 60 in which the H1 data are compared to predictions from different models as a function of the pseudo-rapidity of D^* mesons and of the transverse energy E_t of jets in charm events. In general, the cross section predictions from CASCADE are higher towards large values of η and p_t of the charm quark than those from calculations in the collinear factorization scheme using the DGLAP evolution equations. The HERA-II data are expected to provide sufficient precision to unambiguously discriminate between the different models. The upgraded forward detectors of H1 and ZEUS and more luminosity will make the forward region, i.e. regions of pseudo-rapidity larger than 1.5, more accessible than it has been so far.

Measurements of exclusive final states with jets give access to a number of aspects of heavy quark production and fragmentation as the jets contain information about the kinematics and type of the hard partonic interaction. In photoproduction and at small values of Q^2, $Q^2 \lesssim m_{c \text{ or } b}^2$ the measurement of jet correlations gives access to the hadronic structure of resolved photons. As explained in section 2.3 the particular role of heavy quarks in resolved photon processes is yet to be clarified. The measurement of the shape of the x_γ^{OBS} distribution and of dijet

74

Figure 59: a) Projected number of D^* events in the central H1 detector acceptance as a function of transverse momentum p_t of the charm quark for an integrated luminosity of 400 pb^{-1}. The solid line shows the rate for photoproduction while the light (dark) shaded histograms refer to cuts of $Q^2 > 5(100)$ GeV^2, respectively.

Figure 60: a) Comparison of the cross section predictions for the inclusive charm cross section as a function of pseudo-rapidity, from NLO calculation HVQDIS in the collinear factorization approach using the DGLAP evolution equation (light shaded) and from CASCADE using the k_t factorization approach and the CCFM evolution equation (dark shaded). b) Charm dijet cross sections as a function of E_t of the leading jet in the event as predicted by the RAPGAP Monte Carlo generator (solid line) and by CASCADE (dashed line). In both figures the theory predictions are shown together with the H1 data [8] (see also fig. 23 in section 6.1.2 and fig. 25 in section 6.1.3).

angular distributions of charm jets in different regions of x_γ^{OBS} have given first insights into the relative fractions of the processes of gluon-gluon fusion and charm-excitation. High statistics measurements will allow to obtain details at better precision and to determine the dependence on the external scales Q^2 and p_t, where p_t is the transverse momentum of the final state jets.

The measurement of dijet correlations gives access to the distribution of gluons from the proton in the initial state. In the k_t factorization scheme, the k_t of the gluon can be determined. Predictions in the k_t factorization scheme (CCFM-evolution equation) differ from those using the DGLAP evolution equation in particular in the forward region, i.e. at large values of pseudo-rapidity. Measurements in the forward direction will provide for valuable tests of the different approaches.

The HERA-I data have already provided precise input to the issue of fragmentation. Comparisons of the HERA-data with results from LEP have shown that the assumption of universality is justified. This is all the more interesting as the typical jet energies at HERA are around 10 GeV, and thus significantly lower than those at LEP. One useful question to be addressed with high statistics HERA-II data is to confirm the finding that the fragmentation is independent of the energy by measuring the fragmentation for different processes and at different energies within the same experiment. Furthermore, a fit of the fragmentation distributions could help to discriminate between different fragmentation models, e.g. Lund, [108], Peterson [109], Kartvelishvili [113]. These studies should be performed for both fragmentation fractions and fragmentation functions of charm. For beauty, the production cross sections and branching ratios are too small to allow a full reconstruction of a sufficiently large sample of B-hadrons with the statistics expected at HERA.

The analysis of charm and beauty events in which both quark and anti-quark are explicitly identified is particularly useful for the study of heavy quark production at small transverse momenta. Due to the double-tag the background from uds events is strongly suppressed. This allows to perform measurements at small transverse momenta and small invariant masses $M(Q\bar{Q})$ where present results indicate an excess of the data over the expectations. These data samples allow to make measurements to very small transverse momenta of the quark and anti-quarks, such that the total cross section can be measured with few or no model assumptions.

7.2.3 Beauty Production

The beauty measurements performed with HERA-I data were drastically limited by statistics. It can be estimated that the structure function $F_2^{b\bar{b}}$ can be measured at a four times better accuracy than with HERA-I, i.e. at an experimental uncertainty of better than 10% in the range of $Q^2 < 1000\,\text{GeV}^2$. At this precision the data can help to constrain the theoretical predictions for the charm and beauty components to the inclusive cross section which is presently most precisely measured from scaling violations of the inclusive structure function F_2. Beauty production in channels with exclusive final states, such as $ep \rightarrow e b\bar{b} X \rightarrow e j(j)\mu X$ need to be repeated at higher precision and in a larger kinematic range. Double differential measurements might help to isolate those regions in which the description of the data possibly breaks down. It can be expected that the measurement of the process $ep \rightarrow e b\bar{b} X \rightarrow e B X \rightarrow e J/\psi X$ becomes statistically feasible. With the silicon vertex detectors the lifetime distribution can be used to separate contributions from the process of prompt J/ψ production $ep \rightarrow e c\bar{c} X \rightarrow e J/\psi X$.

7.2.4 Charm and Beauty in Charged Current events

In charged current processes, $e^{\pm}p \to \overset{(-)}{\nu} X$, the charge of the exchanged W-boson provides sensitivity to the charges of the quarks and anti-quarks in the proton. Charm final states in charged current events are dominantly produced from the strange-quark distribution in the proton, $sW^+ \to c$, as the contribution from $dW^+ \to c$ processes is Cabibbo-suppressed: $d^2\sigma(e^+p \to cX)/dxdQ^2 \propto (1-y)^2(d(x)|V_{cd}|^2 + s(x)|V_{cs}|^2)$.

The production of charm in charged current processes has been used at fixed target experiments [243]. At HERA-I, first attempts to measure charm final states in charged current events have been made, but the statistical precision is yet too limited for the measurement to be performed. With the HERA-II statistics and refined methods of charm tagging, the measurement of charm production in charged current processes should become possible.

7.2.5 Charmonium Production

Future analyses of quarkonium production at HERA offer unique possibilities to test the theoretical framework of NRQCD factorization. The existing J/ψ and $\psi(2S)$ measurements can be improved and extended into new kinematic regions, and other quarkonium final states, such as χ_c, may become accessible.

The measurement of inelastic χ_c photoproduction is a particularly powerful way to discriminate between NRQCD and the color-evaporation model. The assumption of a single, universal long-distance factor in the color-evaporation model implies a universal $\sigma[\chi_c]/\sigma[J/\psi]$ ratio. A large χ_c cross section is predicted for photon-proton collisions. The ratio of χ_c production to J/ψ production is expected to be similar to that at hadron colliders, for which $\sigma[\chi_c]/\sigma[J/\psi] \approx 0.5$ [192]. In NRQCD, on the other hand, the $\sigma[\chi_c]/\sigma[J/\psi]$ ratio is process-dependent and strongly suppressed in photoproduction. A search for χ_c production at HERA that results in a cross section measurement or an upper limit on the cross section would probe directly the color-octet matrix element $\langle \mathcal{O}_8^{\chi_J}(^3S_1)\rangle$ and would test the assumption of a single, universal long-distance factor that is implicit in the color-evaporation model.

The inclusion of color-octet processes is crucial in describing the photoproduction of the spin-singlet states $\eta_c(1S)$, $\eta_c(2S)$, and $h_c(1P)$. With regard to the P-wave state h_c, the color-octet contribution is required to cancel the infrared divergence that is present in the color-singlet cross section [244]. The production of the η_c, on the other hand, is dominated by color-octet processes, since the color-singlet cross section vanishes at leading-order, owing to charge-conjugation invariance [245, 246], as is the case for χ_c photoproduction. The cross sections for $\eta_c(1S)$, $\eta_c(2S)$, and $h_c(1P)$ photoproduction are sizable [244, 245], but it is not obvious that these particles can be detected experimentally, even with high-statistics data.

The energy spectrum of J/ψ's produced in association with a photon via the process $\gamma p \to J/\psi + \gamma X$ is a distinctive probe of color-octet processes [247–250]. In the color-singlet channel and at leading-order in α_s, $J/\psi + \gamma$ can be produced only through resolved-photon interactions. The corresponding energy distribution is therefore peaked at low values of z. The intermediate-z and large-z regions of the energy spectrum are expected to be dominated by the color-octet

process $\gamma g \to c\bar{c}_8(^3S_1)\gamma$. Observation of a substantial fraction of $J/\psi + \gamma$ events at $z \gtrsim 0.5$ would provide clear evidence for the presence of color-octet processes in quarkonium photoproduction. Experimentally, this measurement is very difficult due to the large background from photons from π^0 decays which are produced in the final state.

With the significant increase in statistics at the upgraded HERA collider, it might be possible to study inelastic photoproduction of bottomonium states for the first time. The large value of the b quark mass makes the perturbative QCD predictions more reliable than for charm production, and the application of NRQCD should be on safer ground for the bottomonium system, in which $v^2 \approx 0.1$. However, the production rates for Υ states are suppressed compared with those for J/ψ by more than two orders of magnitude at HERA – a consequence of the smaller b quark electric charge and the phase-space reduction that follows from the larger b quark mass.

Precision measurements of heavy vector mesons remain an important part of the HERA physics program. The systematic errors of the HERA-I measurements of diffractive J/ψ production are mostly limited by the statistics available for systematic studies, and HERA-II data will allow for even more precise results. An important goal for HERA-II will be the investigation of Υ production. The existing measurements of Υ production cross section in diffraction at HERA-I [203, 210] indicate that a luminosity of 500 pb^{-1} might yield about 150 events in the detector acceptance. With this statistics a coarse measurement of the energy dependence will be possible.

7.2.6   Charm Spectroscopy

Spectroscopy studies are directly dependent on the size of the data sample. Already in HERA-I sample of charm events, larger than that at the LEP experiments, was collected. While the samples of the new dedicated experiments, such as CLEO-c, FOCUS, Selex, BaBar and Belle, as well as those of the Tevatron experiments are already now significantly larger than the charm samples expected at HERA-II, it will still be interesting to investigate the HERA-data for higher charm resonances. The production process in ep-collisions might provide opportunities to measure particles the production of which is suppressed at other colliders. In this context the question of the existence or non-existence of charmed (and strange) pentaquarks must be resolved.

8 Conclusions

The production of heavy quarks in electron proton collisions at HERA has proven to be a complex and fascinating field of experimental, phenomenological and theoretical challenges. The measurements performed by the H1 and ZEUS collaborations at the HERA collider at DESY have made strong contributions to the quantitative understanding of quantum chromodynamics, the theory of the strong interactions. Since the first measurements of charm at HERA in 1995, new theoretical approaches have been developed and new experimental opportunities have been opened up which allow for detailed tests of the theoretical predictions.

Experimentally, the measurement of heavy quarks poses specific difficulties as the heavy quark cross sections and heavy hadron branching ratios are small compared to the inclusive ep event rates. To cope with the challenge of measuring charm and also beauty, the experiments H1 and ZEUS have continuously refined both the online and offline selection criteria and analysis techniques for heavy quark events. Special purpose detectors, such as the silicon vertex detectors, and dedicated trigger electronics have been implemented in the H1 and ZEUS detectors in order to enhance the efficiencies for identifying and recording events with heavy quarks. Novel analysis methods have been introduced to determine the rates and distributions of events with heavy quarks down to very low transverse momenta and photon virtualities.

Several theoretical calculations are available and are commonly used to describe heavy quark production. In Monte Carlo generators, the matrix element is usually calculated at leading order and parton showers are used to simulate the presence of parton radiations, thus approximating higher order contributions. Calculations at next-to-leading order perturbation theory are available in the collinear factorization approach. These calculations are complemented by predictions using the k_t factorization ansatz. The complexity of the perturbative calculations increases when the one or both of the scales Q^2 and/or p_t are of similar size as the quark mass. The most recent theoretical calculations have been seen to be successful in dealing with this multi-scale problem of heavy quark production.

In particular for charm production, the theories provide predictions that are in reasonable agreement with the H1 and ZEUS measurements. In these calculations the charm mass is typically set to 1.5 GeV or lower, thus allowing the predictions to match with the normalization of the data. In general, the achieved overall precision of the data and the general agreement of the theory suggest the use of the charm data for constraints in global fits of the parton distributions of the proton.

Measurements of charm with jets in photoproduction, when compared to predictions from event generators with leading order matrix elements in the collinear factorization approach, show large contributions from processes with resolved photons, described by photon structure functions. Next-to-leading order calculations in the collinear factorization approach, as well as calculations using k_t factorization are able to give a reasonable description of the contributions from resolved photons already at leading order. The contribution from processes with resolved virtual photons, i.e. in electroproduction, has not yet been precisely determined.

HERA has also provided results on charm fragmentation fractions and momentum distributions which show general agreement with the results from e^+e^- experiments. The measurements of fragmentation, together with the cross section measurements should be used for a

(model-dependent) determination of the parameter choices for the charm mass, the renormalization and factorization scales and the fragmentation functions and parameters.

In more exclusive measurements, some deviations between data and predictions, and among the predictions, have been observed which are situated in distinct areas of phase space. Most prominently, in the region of forward rapidity, the data tend to be higher than the predictions in the collinear factorization approach. New instrumentation of the experiments in the forward region will provide access to this problem in the HERA-II data.

Over the last few years, differential measurements of beauty production have become available. The measurements using events with jets and muons are reasonably reproduced by QCD calculations at next-to-leading order perturbation theory, with a slight excess ($\sim 2\sigma$) of the data in normalization. The analyses make use of new techniques in order to enhance the fraction of b-events in the data samples. In particular the long lifetime of the B-hadrons is exploited using the silicon vertex detectors to determine the beauty production cross sections. H1 measurements using inclusive lifetime tagging have led to the first measurement of the structure function $F_2^{b\bar{b}}$ which describes the contribution of events with b-quarks to the inclusive ep cross section. The results are in good agreement with the predictions based on global fits to inclusive data.

First measurements in which both heavy quarks are identified have been performed. These events allow the simultaneous extraction of the charm and beauty cross sections from angular and charge correlations, and provide access to new tests of higher order QCD effects. Although the available statistics are still poor, there is a general trend for the measured beauty cross sections to be higher than the expectations while the charm results agree with the predictions.

The HERA collider experiments have also contributed to the study of the process of inelastic charmonium production. The description of the data by leading order calculations based on non-relativistic QCD (NRQCD) is yet to be clarified.

While the picture of heavy quark production in ep collisions is taking on shape, it is clear that many more measurements are needed to reach a precision which allows to discriminate between the existing theories and to establish precision predictions. At HERA-II, increased luminosity and new detectors will allow for the data to match or exceed the precision of the theory calculations. The goals for HERA-II are to complete the picture of charm production towards the highest possible photon virtualities Q^2, transverse momenta p_t, and pseudo-rapidities η and to verify the models using beauty production. With increased luminosity, ample statistics of charmed mesons will be produced allowing to answer the open questions in the field of spectroscopy, the most prominent of which is the apparent contradiction between H1 who have reported evidence for an exotic resonance with charm contents and ZEUS who have not confirmed this observation.

In summary, the understanding of heavy-quark production is currently one of the many intriguing issues in ep collision physics. During HERA-I the field has been outlined and many questions have been raised and provisionally answered. The HERA-II data will be instrumental in bringing many of the still open questions to a conclusion.

Acknowledgments

References

[1] S. I. Alekhin *et al.* [HERA and COMPAS Groups Collaboration], "Compilation Of Cross-Sections. 4. Gamma, Neutrino, Lambda, Sigma, Xi, And K0(L) Induced Reactions" CERN-HERA-87-01

[2] S. Aid *et al.* [H1 Collaboration], Nucl. Phys. B **472** (1996) 32 [hep-ex/9604005].

[3] C. Adloff *et al.* [H1 Collaboration], Z. Phys. C **72** (1996) 593 [hep-ex/9607012].

[4] C. Adloff *et al.* [H1 Collaboration], Nucl. Phys. B **545** (1999) 21 [hep-ex/9812023].

[5] C. Adloff *et al.* [H1 Collaboration], Phys. Lett. B **528** (2002) 199 [hep-ex/0108039].

[6] A. Aktas *et al.* [H1 Collaboration], Eur. Phys. J. C **38** (2005) 447 [hep-ex/0408149].

[7] A. Aktas *et al.* [H1 Collaboration], contributed paper 5-0162, International Conference on High Energy Physics (ICHEP04), Beijing, China, 2004.

[8] A. Aktas *et al.* [H1 Collaboration], contributed paper 5-0163, International Conference on High Energy Physics (ICHEP04), Beijing, China, 2004.

[9] A. Aktas *et al.* [H1 Collaboration], Submitted to the XXII International Symposium on Lepton-Photon Interactions at High Energy, June 30-July 5, Uppsala, Sweden, Abstract 406.

[10] A. Aktas *et al.* [H1 Collaboration], Submitted to the XXII International Symposium on Lepton-Photon Interactions at High Energy, June 30-July 5, Uppsala, Sweden, Abstract 407.

[11] M. Derrick *et al.* [ZEUS Collaboration], Phys. Lett. B **349** (1995) 225 [hep-ex/9502002].

[12] J. Breitweg *et al.* [ZEUS Collaboration], Phys. Lett. B **401** (1997) 192 [hep-ex/9704011].

[13] J. Breitweg *et al.* [ZEUS Collaboration], Phys. Lett. B **407** (1997) 402 [hep-ex/9706009].

[14] J. Breitweg *et al.* [ZEUS Collaboration], Eur. Phys. J. C **6** (1999) 67 [hep-ex/9807008].

[15] J. Breitweg *et al.* [ZEUS Collaboration], Eur. Phys. J. C **12** (2000) 35 [hep-ex/9908012].

[16] S. Chekanov *et al.* [ZEUS Collaboration], Phys. Rev. D **69**, 012004 (2004) [hep-ex/0308068].

[17] S. Chekanov *et al.* [ZEUS Collaboration], Phys. Lett. B **565** (2003) 87 [hep-ex/0302025].

[18] S. Chekanov *et al.* [ZEUS Collaboration], Phys. Lett. B **590** (2004) 143 [hep-ex/0401017].

[19] ZEUS Collaboration, Submitted to the 31st International Conference on High Energy Physics, ICHEP02, 2002, Amsterdam, Abstract 786.

[20] ZEUS Collaboration, contributed paper 564, International Europhysics Conference on High Energy Physics (EPS 2003), Aachen, Germany, 2003.

[21] ZEUS Collaboration, Submitted to the 31st International Conference on High Energy Physics, ICHEP02, 2002, Amsterdam, Abstract 778.

[22] ZEUS Collaboration, Submitted to the 32nd International Conference on High Energy Physics, ICHEP04, August 16, 2004, Beijing, Abstract 5-0332, 11-333.

[23] ZEUS Collaboration, Submitted to the 32nd International Conference on High Energy Physics, ICHEP04, August 16, 2004, Beijing, Abstract 5-0344, 11-345.

[24] ZEUS Collaboration, Submitted to the 32nd International Conference on High Energy Physics, ICHEP04, August 16, 2004, Beijing, Abstract 5-0347, 11-348.

[25] ZEUS Collaboration, Submitted to the XXII International Symposium on Lepton-Photon Interactions at High Energy, June 30-July 5, Uppsala, Sweden, Abstract 264.

[26] ZEUS Collaboration, Submitted to the XXII International Symposium on Lepton-Photon Interactions at High Energy, June 30-July 5, Uppsala, Sweden, Abstract 266.

[27] S. Aid *et al.* [H1 Collaboration], Nucl. Phys. B **472** (1996) 3 [hep-ex/9603005].

[28] C. Adloff *et al.* [H1 Collaboration], Eur. Phys. J. C **10** (1999) 373 [hep-ex/9903008].

[29] C. Adloff *et al.* [H1 Collaboration], Eur. Phys. J. C **25** (2002) 25 [hep-ex/0205064].

[30] C. Adloff *et al.* [H1 Collaboration], Eur. Phys. J. C **25** (2002) 41 [hep-ex/0205065].

[31] J. Breitweg *et al.* [ZEUS Collaboration], Z. Phys. C **76** (1997) 599 [hep-ex/9708010].

[32] S. Chekanov *et al.* [ZEUS Collaboration], Eur. Phys. J. C **27** (2003) 173 [hep-ex/0211011].

[33] S. Chekanov *et al.* [ZEUS Collaboration], hep-ex/0505008.

[34] S. Chekanov *et al.* [ZEUS Collaboration], contributed paper 569, International Europhysics Conference on High Energy Physics (EPS 2003), Aachen, Germany, 2003.

[35] J. Breitweg *et al.* [ZEUS Collaboration], Phys. Lett. B **481** (2000) 213 [hep-ex/0003018].

[36] C. Adloff *et al.* [H1 Collaboration], Phys. Lett. B **467** (1999) 156 [hep-ex/9909029]; [Erratum-ibid. B **518** (2001) 331].

[37] ZEUS Collaboration, Submitted to the 30th International Conference on High Energy Physics, ICHEP00, July 27, 2000, Osaka, Abstract 853.

[38] ZEUS Collaboration, Submitted to the 29th International Conference on High Energy Physics, ICHEP90, July 23, 1998, Vancouver, Abstract 772.

[39] J. Breitweg *et al.* [ZEUS Collaboration], Eur. Phys. J. C **18** (2001) 625 [hep-ex/0011081].

[40] S. Chekanov *et al.* [ZEUS Collaboration], Phys. Rev. D **70** (2004) 012008 [hep-ex/0312057].

[41] S. Chekanov *et al.* [ZEUS Collaboration], Phys. Lett. B **599** (2004) 173 [hep-ex/0405069].

[42] S. Chekanov *et al.* [ZEUS Collaboration],

[43] A. Aktas *et al.* [H1 Collaboration], to appear in Eur. Phys. J. C., [hep-ex/0411046].

[44] A. Aktas *et al.* [H1 Collaboration], Eur. Phys. J. C **41** (2005) 453 [hep-ex/0502010].

[45] A. Aktas *et al.* [H1 Collaboration], Submitted to the 32nd International Conference on High Energy Physics, ICHEP04, August 16, 2004, Beijing, Abstract 5-0760.

[46] A. Aktas *et al.* [H1 Collaboration], Submitted to the XXII International Symposium on Lepton-Photon Interactions at High Energy, June 30-July 5, Uppsala, Sweden, Abstract 385.

[47] A. Aktas *et al.* [H1 Collaboration], submitted to Phys. Lett. B, 03/05, hep-ex/0503038.

[48] S. Chekanov *et al.* [ZEUS Collaboration], contributed paper 575, International Europhysics Conference on High Energy Physics (EPS 2003), Aachen, Germany, 2003.

[49] ZEUS Collaboration, Submitted to the 30th International Conference on High Energy Physics, ICHEP00, July 27, 2000, Osaka, Abstract 854.

[50] ZEUS Collaboration, contributed paper 497, International Europhysics Conference on High Energy Physics (EPS 2001), Budapest, Hungary, 2001.

[51] A. Aktas *et al.* [H1 Collaboration], Phys. Lett. B **588** (2004) 17 [hep-ex/0403017].

[52] S. Chekanov *et al.* [ZEUS Collaboration], Eur. Phys. J. C **38** (2004) 29 [hep-ex/0409033].

[53] S. Chekanov *et al.* [ZEUS Collaboration], Phys. Lett. B **591** (2004) 7 [hep-ex/0403051].

[54] S. Chekanov *et al.* [ZEUS Collaboration], Phys. Lett. B **610** (2005) 212 [hep-ex/0501069].

[55] S. Chekanov *et al.* [ZEUS Collaboration], Phys. Lett. B **545** (2002) 244 [hep-ex/0206020].

[56] S. Chekanov *et al.* [ZEUS Collaboration], Nucl. Phys. B **672** (2003) 3 [hep-ex/0307068].

[57] C. Adloff *et al.* [H1 Collaboration], Phys. Lett. B **520** (2001) 191 [hep-ex/0108047].

[58] A. Aktas *et al.* [H1 Collaboration], contributed paper 6-0178, International Conference on High Energy Physics (ICHEP04), Beijing, China, 2004.

[59] V.N. Gribov and L.N. Lipatov, Yad. Fiz. **15** (1972) 781 [Sov. J. Nucl. Phys. **15** (1972) 438];
G. Altarelli and G. Parisi, Nucl. Phys. B **126** (1977) 298;
Y.L. Dokshitzer, Sov. Phys. JETP **46** (1977) 641 [Zh. Eksp. Teor. Fiz. **73** (1977) 1216].

[60] R. Thorne, to appear in the proceedings of 13th International Workshop on Deep Inelastic Scattering (DIS 2005), Madison, Wisconsin, USA, April 2005, hep-ph/05XXXXX.

[61] E. A. Kuraev, L. N. Lipatov and V. S. Fadin, Sov. Phys. JETP **44** (1976) 443 [Zh. Eksp. Teor. Fiz. **71** (1976) 840].

[62] E. A. Kuraev, L. N. Lipatov and V. S. Fadin, Sov. Phys. JETP **45** (1977) 199 [Zh. Eksp. Teor. Fiz. **72** (1977) 377].

[63] I. I. Balitsky and L. N. Lipatov, Sov. J. Nucl. Phys. **28** (1978) 822 [Yad. Fiz. **28** (1978) 1597].

[64] A. H. Mueller and B. Patel, Nucl. Phys. B **425** (1994) 471 [hep-ph/9403256].

[65] M. Ciafaloni, Nucl. Phys. B **296** (1988) 49;
S. Catani, F. Fiorani and G. Marchesini, Phys. Lett. B **234** (1990) 339;
S. Catani, F. Fiorani and G. Marchesini, Nucl. Phys. B **336** (1990) 18;
G. Marchesini, Nucl. Phys. B **445** (1995) 49.

[66] C. Adloff *et al.* [H1 Collaboration], Eur. Phys. J. C **21** (2001) 33 [hep-ex/0012053].

[67] S. Chekanov *et al.* [ZEUS Collaboration], Eur. Phys. J. C **21** (2001) 443 [hep-ex/0105090].

[68] S. Chekanov *et al.* [ZEUS Collaboration], Phys. Rev. D **67** (2003) 012007 [hep-ex/0208023].

[69] C. Adloff *et al.* [H1 Collaboration], Eur. Phys. J. C **30** (2003) 1 [hep-ex/0304003].

[70] A. D. Martin, W. J. Stirling and R. G. Roberts, Phys. Rev. D **50** (1994) 6734 [hep-ph/9406315].

[71] H. L. Lai *et al.*, Phys. Rev. D **55** (1997) 1280 [hep-ph/9606399].

[72] H.L. Lai *et al.* [CTEQ Collaboration], Eur. Phys. J. C **12** (2000) 375 [hep-ph/9903282].

[73] A.D. Martin, R.G. Roberts, W.J. Stirling and R.S. Thorne, Eur. Phys. J. C **4** (1998) 463 [hep-ph/9803445].

[74] A. D. Martin, R. G. Roberts, W. J. Stirling and R. S. Thorne, Eur. Phys. J. C **23** (2002) 73 [hep-ph/0110215].

[75] S. Kretzer, H. L. Lai, F. I. Olness and W. K. Tung, Phys. Rev. D **69** (2004) 114005 [hep-ph/0307022].

[76] A. D. Martin, R. G. Roberts, W. J. Stirling and R. S. Thorne, Eur. Phys. J. C **35** (2004) 325 [hep-ph/0308087].

[77] E. Laenen, S. Riemersma, J. Smith and W. L. van Neerven, Nucl. Phys. B **392** (1993) 162;

[78] E. Laenen, S. Riemersma, J. Smith and W. L. van Neerven, Nucl. Phys. B **392** (1993) 229;

[79] S. Riemersma, J. Smith and W. L. van Neerven, Phys. Lett. B **347** (1995) 143 [hep-ph/9411431].

[80] S. Frixione, P. Nason and G. Ridolfi, Nucl. Phys. B **454** (1995) 3 [hep-ph/9506226].

[81] B. W. Harris and J. Smith, Nucl. Phys. B **452** (1995) 109 [hep-ph/9503484].

[82] F. I. Olness and W. K. Tung, Nucl. Phys. B **308** (1988) 813;

[83] M. A. G. Aivazis, J. C. Collins, F. I. Olness and W. K. Tung, Phys. Rev. D **50** (1994) 3102 [hep-ph/9312319];

[84] M. A. G. Aivazis, F. I. Olness and W. K. Tung, Phys. Rev. D **50** (1994) 3085 [hep-ph/9312318];

[85] M. Kramer, F. I. Olness and D. E. Soper, Phys. Rev. D **62** (2000) 096007 [hep-ph/0003035];

[86] R. S. Thorne and R. G. Roberts, Phys. Rev. D **57** (1998) 6871 [hep-ph/9709442]; Phys. Lett. B **421** (1998) 303 [hep-ph/9711223]; Eur. Phys. J. C **19** (2001) 339 [hep-ph/0010344].

[87] M. Cacciari, M. Greco and P. Nason, JHEP **9805** (1998) 007 [hep-ph/9803400];

[88] M. Cacciari, S. Frixione and P. Nason, JHEP **0103** (2001) 006 [hep-ph/0102134].

[89] M. Buza, Y. Matiounine, J. Smith and W. L. van Neerven, Phys. Lett. B **411** (1997) 211 [hep-ph/9707263];

[90] A. Chuvakin, J. Smith and W. L. van Neerven, Phys. Rev. D **61** (2000) 096004 [hep-ph/9910250]; Phys. Rev. D **62** (2000) 036004 [hep-ph/0002011].

[91] M. Cacciari and P. Nason, Phys. Rev. Lett. **89** (2002) 122003 [hep-ph/0204025].

[92] S. Frixione and P. Nason, JHEP **0203** (2002) 053 [hep-ph/0201281].

[93] M. Cacciari and P. Nason, JHEP **0309** (2003) 006 [hep-ph/0306212].

[94] B. Mele and P. Nason, Nucl. Phys. B **361** (1991) 626.

[95] J. Binnewies, B. A. Kniehl and G. Kramer, Z. Phys. C **76** (1997) 677 [hep-ph/9702408].

[96] J. Binnewies, B.A. Kniehl and G. Kramer, Phys. Rev. D **58** (1998) 014014 [hep-ph/9712482].

[97] G. Kramer, Proceedings of the Ringberg Workshop New Trends in HERA Physics 1999, eds. G. Grindhammer, B. A. Kniehl and G. Kramer, Lecture Notes in Physics 546, Springer, 2000, p. 275.

[98] B. A. Kniehl, in 14th Topical Conference on Hadron Collider Physics (eds. M. Erdmann, T. M?uller), p. 161 (Springer, Heidelberg, 2003), hep-ph/0211008.

[99] G. Kramer and H. Spiesberger, Eur. Phys. J. C **38** (2004) 309 [hep-ph/0311062].

[100] B. A. Kniehl, G. Kramer, I. Schienbein and H. Spiesberger, hep-ph/0502194.

[101] R. Nisius, Phys. Rept. **332** (2000) 165 [hep-ex/9912049].

[102] J. Breitweg *et al.* [ZEUS Collaboration], contributed paper 495, International Europhysics Conference on High Energy Physics (EPS 2001), Budapest, Hungary, 2001.

[103] G. Ingelman, J. Rathsman and G.A. Schuler, Comput. Phys. Commun. **101** (1997) 135 [hep-ph/9605285].

[104] H. Jung and G.P. Salam, Eur. Phys. J. C **19** (2001) 351 [hep-ph/0012143];
H. Jung, Comput. Phys. Commun. **143** (2002) 100 [hep-ph/0109102].

[105] B. Andersson, G. Gustafson and C. Peterson, Z. Phys. C **1**, 105 (1979).

[106] B. Andersson, G. Gustafson, G. Ingelman and T. Sjöstrand, Phys. Rept. **97** (1983) 31.

[107] T. Sjostrand, Comput. Phys. Commun. **82** (1994) 74.

[108] T. Sjöstrand, Comput. Phys. Commun. **39** (1986) 347;
T. Sjöstrand and M. Bengtsson, Comput. Phys. Commun. **43** (1987) 367;
T. Sjöstrand *et al.*, Comput. Phys. Commun. **135** (2001) 238 [hep-ph/0010017].

[109] C. Peterson, D. Schlatter, I. Schmitt and P.M. Zerwas, Phys. Rev. D **27** (1983) 105.

[110] M. G. Bowler, Z. Phys. C **11** (1981) 169.

[111] B. Andersson, G. Gustafson and B. Soderberg, Z. Phys. C **20** (1983) 317.

[112] P. D. B. Collins and T. P. Spiller, J. Phys. G **11** (1985) 1289.

[113] V. G. Kartvelishvili, A. K. Likhoded and V. A. Petrov, Phys. Lett. B 78 (1978) 615.

[114] E. Norrbin and T. Sjostrand, Eur. Phys. J. C **17** (2000) 137 [hep-ph/0005110].

[115] R. Barate *et al.* [ALEPH Collaboration], Eur. Phys. J. C **16** (2000) 597 [hep-ex/9909032].

[116] P. Abreu *et al.* [DELPHI Collaboration], Eur. Phys. J. C **12** (2000) 225.

[117] G. Rudolph [ALEPH collaboration], private communication.

[118] H. Jung, Mod. Phys. Lett. A **19** (2004) 1 [hep-ph/0311249].

[119] J.R. Andersen *et al.* [Small x Coll.], Eur. Phys. J. C **35** (2004) 67 [hep-ph/0312333].

[120] M. Hansson and H. Jung, hep-ph/0309009.

[121] M. Hansson, H. Jung and L. Jonsson, hep-ph/0402019.

[122] S. Catani, M. Ciafaloni and F. Hautmann, Nucl. Phys. B **366** (1991) 135.

[123] J. C. Collins and R. K. Ellis, Nucl. Phys. B **360** (1991) 3.

[124] H. Jung, Comput. Phys. Commun. **86** (1995) 147.

[125] G. Marchesini, B.R. Webber, G. Abbiendi, I.G. Knowles, M.H. Seymour and L. Stanco, Computer Phys. Commun. 67 (1992) 465; HERWIG 6.5, G. Corcella, I.G. Knowles, G. Marchesini, S. Moretti, K. Odagiri, P. Richardson, M.H. Seymour and B.R. Webber, JHEP 0101 (2001) 010 [hep-ph/0011363]; hep-ph/0210213.

[126] G. A. Schuler and H. Spiesberger, Proceedings, Physics at HERA, vol. 3* 1419-1432.

[127] A. Kwiatkowski, H. Spiesberger and H.J. Möhring, Comput. Phys. Commun. **69** (1992) 155.

[128] H. Jung, Phys. Rev. D **65**, 034015 (2002) [hep-ph/0110034].

[129] P. Nason and C. Oleari, Nucl. Phys. B **565** (2000) 245 [hep-ph/9903541].

[130] S. Frixione and B. R. Webber, JHEP **0206** (2002) 029 [hep-ph/0204244].

[131] S. Frixione, P. Nason and B. R. Webber, JHEP **0308** (2003) 007 [hep-ph/0305252].

[132] M. Cacciari, S. Frixione, M. L. Mangano, P. Nason and G. Ridolfi, JHEP **0407** (2004) 033 [hep-ph/0312132].

[133] C. Chen, [CDF Collaboration], presentation at Beauty 2003, http://www-cdf.fnal.gov/physics/new/bottom/030904.blessed-bxsec-jpsi/ ; M. Bishai [CDF Collaboration], presentation at Fermilab, Dec 5. 2003, http://www-cdf.fnal.gov/~bishai/papers/wandc.pdf

[134] K. Ackerstaff *et al.* [HERMES Collaboration], Nucl. Instrum. Meth. A **417**, 230 (1998) [hep-ex/9806008].

[135] HERA-B Design Report, DESY-PRC 95/01 (ftp://ftp.desy.de/pub/herab/tdr/tdr.ps.gz)

[136] H1 and ZEUS publications are listed at http://www-h1.desy.de/publications/H1publication.short_list.html and http://www-zeus.desy.de/zeus_papers/zeus_papers.html

[137] http://www-cdf.fnal.gov/

[138] http://www-d0.fnal.gov/

[139] I. Abt *et al.* [H1 Collaboration], Nucl. Instrum. Meth. A **386** (1997) 310 and 348.

88

[140] D. Pitzl *et al.*, Nucl. Instrum. Meth. A **454** (2000) 334 [hep-ex/0002044].

[141] T. Nicholls *et al.* [H1 SpaCal Group], Nucl. Instrum. Meth. A **374** (1996) 149.

[142] M. Derrick *et al.* [ZEUS Collaboration], Phys. Lett. B **293**, 465 (1992).

[143] ZEUS Collaboration, U.Holm (ed.), (unpublished), DESY 1993, available at http://www-zeus.desy.de/bluebook/bluebook.html

[144] D. E. Groom *et al.* [Particle Data Group Collaboration], Eur. Phys. J. C **15** (2000) 1.

[145] H1 Internal Note 518 (05/1997).

[146] B. Wessling, Dissertation, Univ. Hamburg 2004, unpublished, available at http://www-h1.desy.de/publications/theses.list.html.

[147] S.D. Ellis and D.E. Soper, Phys. Rev. D **48** (1993) 3160 [hep-ph/9305266].

[148] S. Catani, Y.L. Dokshitzer, M.H. Seymour and B.R. Webber, Nucl. Phys. B **406** (1993) 187.

[149] J.M. Butterworth, J.P. Couchman, B.E. Cox and B.M. Waugh, Comput. Phys. Commun. **153** (2003) 85 [hep-ph/0210022].

[150] R. J. Barlow and C. Beeston, Comput. Phys. Commun. **77** (1993) 219.

[151] http://root.cern.ch/root/html/TFractionFitter.h

[152] R. Frühwirth and A. Strandlie, Comput. Phys. Commun. **120** (1999) 197.

[153] R. Frühwirth *et al.*, Nucl. Instrum. Meth. A **502** (2003) 699.

[154] R. Akers *et al.* [OPAL Collaboration], Z. Phys. C **67** (1995) 27.

[155] H. Albrecht *et al.* [ARGUS Collaboration], Z. Phys. C **52** (1991) 353.

[156] M. Artuso *et al.* [CLEO Collaboration], Phys. Rev. D **70** (2004) 112001 [hep-ex/0402040].

[157] D. Buskulic *et al.* [ALEPH Collaboration], Phys. Lett. B **357** (1995) 699.

[158] K. Ackerstaff *et al.* [OPAL Collaboration], Eur. Phys. J. C **5** (1998) 1 [hep-ex/9802008].

[159] L. Gladilin, hep-ex/9912064.

[160] F. Abe *et al.* [CDF Collaboration], Phys. Rev. Lett. **71** (1993) 2396; Phys. Rev. D **53** (1996) 1051 [hep-ex/9508017];
S. Abachi *et al.* [D0 Collaboration], Phys. Rev. Lett. **74** (1995) 3548; Phys. Lett. B **370** (1996) 239.

[161] M. Acciarri *et al.* [L3 Collaboration], Phys. Lett. B **503** (2001) 10 [hep-ex/0011070].

[162] M. Cacciari, hep-ph/0407187.

[163] T. Carli, V. Chiochia and K. Klimek, JHEP **0309**, 070 (2003) [hep-ph/0305103].

[164] A. D. Martin, R. G. Roberts, W. J. Stirling and R. S. Thorne, Eur. Phys. J. C **39** (2005) 155 [hep-ph/0411040].

[165] M. Krämer, Prog. Part. Nucl. Phys. **47** (2001) 141 [hep-ph/0106120].

[166] N. Brambilla *et al.*, hep-ph/0412158.

[167] E. L. Berger and D. L. Jones, Phys. Rev. D **23** (1981) 1521.

[168] R. Baier and R. Rückl, Nucl. Phys. B **201** (1982) 1.

[169] R. Baier and R. Rückl, Phys. Lett. B **102** (1981) 364.

[170] R. Baier and R. Rückl, Z. Phys. C **19** (1983) 251.

[171] F. Halzen, Phys. Lett. B **69** (1977) 105.

[172] O. J. P. Eboli, E. M. Gregores and F. Halzen, Phys. Lett. B **451** (1999) 241 [hep-ph/9802421].

[173] A. Edin, G. Ingelman and J. Rathsman, Phys. Rev. D **56** (1997) 7317 [hep-ph/9705311].

[174] W. E. Caswell and G. P. Lepage, Phys. Lett. B **167** (1986) 437.

[175] B. A. Thacker and G. P. Lepage, Phys. Rev. D **43** (1991) 196.

[176] G. T. Bodwin, E. Braaten and G. P. Lepage, Phys. Rev. D **51** (1995) 1125 [Erratum-ibid. D **55** (1997) 5853] [hep-ph/9407339].

[177] M. Cacciari and M. Krämer, Phys. Rev. Lett. **76** (1996) 4128 [hep-ph/9601276].

[178] M. Beneke, M. Krämer, and M. Vanttinen, Phys. Rev. D **57** (1998) 4258 [hep-ph/9709376].

[179] J. Amundson, S. Fleming and I. Maksymyk, Phys. Rev. D **56** (1997) 5844 [hep-ph/9601298].

[180] R. M. Godbole, D. P. Roy, and K. Sridhar, Phys. Lett. B **373** (1996) 328 [hep-ph/9511433].

[181] B. A. Kniehl and G. Kramer, Phys. Lett. B **413** (1997) 416 [hep-ph/9703280].

[182] B. A. Kniehl and G. Kramer, Phys. Rev. D **56** (1997) 5820 [hep-ph/9706369].

[183] E. Braaten, B. A. Kniehl and J. Lee, Phys. Rev. D **62** (2000) 094005 [hep-ph/9911436].

[184] M. Krämer, J. Zunft, J. Steegborn, and P. M. Zerwas, Phys. Lett. B **348** (1995) 657 [hep-ph/9411372].

[185] M. Krämer, Nucl. Phys. B **459** (1996) 3 [hep-ph/9508409].

[186] S. P. Baranov, Phys. Lett. B **428** (1998) 377.

[187] V. A. Saleev and N. P. Zotov, Mod. Phys. Lett. A **9** (1994) 151 [Erratum-ibid. A **9** (1994) 1517].

[188] H. Jung and G. P. Salam, Eur. Phys. J. C **19** (2001) 351 [hep-ph/0012143].

[189] H. Jung, Comput. Phys. Commun. **143** (2002) 100 [hep-ph/0109102].

[190] A. V. Lipatov and N. P. Zotov, Eur. Phys. J. C **27** (2003) 87 [hep-ph/0210310].

[191] F. Abe *et al.* [CDF Collaboration], Phys. Rev. Lett. **79** (1997) 572.

[192] F. Abe *et al.* [CDF Collaboration], Phys. Rev. Lett. **79** (1997) 578.

[193] B. A. Kniehl and L. Zwirner, Nucl. Phys. **B621** (2002) 337 [hep-ph/0112199].

[194] M. G. Ryskin, Z. Phys. C **57** (1993) 89.

[195] S. J. Brodsky, L. Frankfurt, J. F. Gunion, A. H. Mueller and M. Strikman, Phys. Rev. D **50** (1994) 3134 [hep-ph/9402283].

[196] J. C. Collins, L. Frankfurt and M. Strikman, Phys. Rev. D **56** (1997) 2982 [hep-ph/9611433].

[197] J. C. Collins, Phys. Rev. D **57** (1998) 3051 [Erratum-ibid. D **61** (2000) 019902] [hep-ph/9709499].

[198] T. Teubner, hep-ph/9910329.

[199] J. Bartels and H. Kowalski, Eur. Phys. J. C **19** (2001) 693 [hep-ph/0010345].

[200] A. Hayashigaki and K. Tanaka, hep-ph/0401053.

[201] S. Aid *et al.* [H1 Collaboration], Nucl. Phys. B **463** (1996) 3 [hep-ex/9601004].

[202] C. Adloff *et al.* [H1 Collaboration], Eur. Phys. J. C **13** (2000) 371 [hep-ex/9902019].

[203] C. Adloff *et al.* [H1 Collaboration], Phys. Lett. B **483** (2000) 23 [hep-ex/0003020].

[204] C. Adloff *et al.* [H1 Collaboration], Phys. Lett. B **483** (2000) 360 [hep-ex/0005010].

[205] C. Adloff *et al.* [H1 Collaboration], Phys. Lett. B **539** (2002) 25 [hep-ex/0203022].

[206] C. Adloff *et al.* [H1 Collaboration], Phys. Lett. B **541** (2002) 251 [hep-ex/0205107].

[207] A. Aktas *et al.* [H1 Collaboration], Phys. Lett. B **568** (2003) 205 [hep-ex/0306013].

[208] A. Aktas *et al.* [H1 Collaboration], contributed paper 6-0180, International Conference on High Energy Physics (ICHEP04), Beijing, China, 2004.

[209] J. Breitweg *et al.* [ZEUS Collaboration], Eur. Phys. J. C **6** (1999) 603 [hep-ex/9808020].

[210] J. Breitweg *et al.* [ZEUS Collaboration], Phys. Lett. B **437** (1998) 432 [hep-ex/9807020].

[211] J. Breitweg *et al.* [ZEUS Collaboration], Eur. Phys. J. C **14** (2000) 213 [hep-ex/9910038].

[212] J. Breitweg *et al.* [ZEUS Collaborations], Eur. Phys. J. C **12** (2000) 393 [hep-ex/9908026].

[213] J. Breitweg *et al.* [ZEUS Collaboration], Phys. Lett. B **487** (2000) 273 [hep-ex/0006013].

[214] S. Chekanov *et al.* [ZEUS Collaboration], Eur. Phys. J. C **26** (2003) 389 [hep-ex/0205081].

[215] S. Chekanov *et al.* [ZEUS Collaboration], contributed paper 549, International Europhysics Conference on High Energy Physics (EPS 2003), Aachen, Germany, 2003.

[216] S. Chekanov *et al.* [ZEUS Collaboration], Eur. Phys. J. C **24** (2002) 345 [hep-ex/0201043].

[217] S. Chekanov *et al.* [ZEUS Collaboration], Nucl. Phys. B **695** (2004) 3 [hep-ex/0404008].

[218] L. Frankfurt, W. Koepf and M. Strikman, Phys. Rev. D **57** (1998) 512 [hep-ph/9702216].

[219] M. McDermott, L. Frankfurt, V. Guzey and M. Strikman, Eur. Phys. J. C **16** (2000) 641 [hep-ph/9912547].

[220] L. Frankfurt, M. McDermott and M. Strikman, JHEP **0103** (2001) 045 [hep-ph/0009086].

[221] M. G. Ryskin, R. G. Roberts, A. D. Martin and E. M. Levin, Z. Phys. C **76** (1997) 231 [hep-ph/9511228].

[222] A. D. Martin and M. G. Ryskin, Phys. Rev. D **57** (1998) 6692 [hep-ph/9711371].

[223] A. D. Martin, M. G. Ryskin and T. Teubner, Phys. Rev. D **62** (2000) 014022 [hep-ph/9912551].

[224] D. Y. Ivanov, A. Schäfer, L. Szymanowski and G. Krasnikov, Eur. Phys. J. C **34** (2004) 297 [hep-ph/0401131].

[225] T. Regge, Nuovo Cim. **14** (1959) 951.

[226] T. Regge, Nuovo Cim. **18** (1960) 947.

[227] J. J. Sakurai, Phys. Rev. Lett. **22** (1969) 981.

[228] A. Donnachie and P. V. Landshoff, Phys. Lett. B **296** (1992) 227 [hep-ph/9209205].

[229] A. Donnachie and P. V. Landshoff, Phys. Lett. B **437** (1998) 408 [hep-ph/9806344].

[230] N. N. Nikolaev and B. G. Zakharov, Z. Phys. C **64** (1994) 631 [hep-ph/9306230].

[231] E. Gotsman, E. Levin, U. Maor and E. Naftali, Phys. Lett. B **532** (2002) 37 [hep-ph/0110256].

[232] T. Nakano et al. [LEPS Collaboration], Phys. Rev. Lett. 91 (2003) 012002;
J. Barth et al. [SAPHIR Collaboration], Phys. Lett. B 572 (2003) 127;
V. Kubarovsky et al. [CLAS Collaboration], Phys. Rev. Lett. 92 (2004) 032001;
[Erratum-ibid. 92 (2004) 049902].

[233] V. V. Barmin et al. [DIANA Collaboration], Phys. Atom. Nucl. 66 (2003) 1715 [Yad. Fiz. 66 (2003) 1763];
A. E. Asratyan, A. G. Dolgolenko and M. A. Kubantsev, Phys. Atom. Nucl. 67 (2004) 682;
A. Aleev et al. [SVD Collaboration], hep-ex/0401024;
A. Airapetian et al. [HERMES Collaboration], Phys. Lett. B 585 (2004) 213;
M. Abdel-Bary et al. [COSY-TOF Collab.], Phys. Lett. B 595 (2004) 127;
S. Chekanov et al. [ZEUS Collaboration], Phys. Lett. B 591 (2004) 7.

[234] H. J. Lipkin, Phys. Lett. B 195 (1987) 484;
C. Gignoux, B. Silvestre-Brac and J. M. Richard, Phys. Lett. B 193 (1987) 323;
D. O. Riska and N. N. Scoccola, Phys. Lett. B 299 (1993) 338;
F. Stancu, Phys. Rev. D 58 (1998) 111501.

[235] O. Gutsche, Dissertation, Univ. Hamburg 2005, unpublished.

[236] M. Göttlich, I. Glushkov, private communication.

[237] A. Baird *et al.*, IEEE Trans. Nucl. Sci. **48** (2001) 1276 [hep-ex/0104010].

[238] A. B. Meyer [H1 Collaboration], "A New Object-Oriented Physics Analysis Framework for the H1 Experiment", published in *Budapest 2001, High energy physics* hep2001/276.

[239] O. Kind *et al.*, eConf **C0303241** (2003) MOLT002 [hep-ex/0305095].

[240] Rene Brun and Fons Rademakers, Proceedings AIHENP'96 Workshop, Lausanne, Sep. 1996, Nucl. Instrum. Meth. A **389** (1997) 81-86. See also http://root.cern.ch/.

[241] M. Glück, E. Reya and A. Vogt, Phys. Rev. D **45** (1992) 3986;
M. Glück, E. Reya and A. Vogt, Phys. Rev. D **46** (1992) 1973.

[242] A.D. Martin, W.J. Stirling and R.G. Roberts, in: Proc. of the Workshop on Quantum Field Theory and Theoretical Aspects of High Energy Physics, eds. B. Geyer and E.M. Ilgenfritz (1993) p. 11.

[243] A.O. Bazarko et al., Z. Phys. C65 (1995) 189;
S.A. Rabinowitz et al., Phys. Rev. Lett. 70 (1993) 134.

[244] S. Fleming and T. Mehen, Phys. Rev. D **58** (1998) 037503 [hep-ph/9801328].

[245] L. Hao, F. Yuan and K. Chao, Phys. Rev. Lett. **83** (1999) 4490 [hep-ph/9902338].

[246] L. Hao, F. Yuan and K. Chao, Phys. Rev. D **62** (2000) 074023 [hep-ph/0004203].

[247] C. S. Kim and E. Reya, Phys. Lett. B **300** (1993) 298.

[248] T. Mehen, Phys. Rev. D **55** (1997) 4338 [hep-ph/9611321].

[249] M. Cacciari, M. Greco and M. Krämer, Phys. Rev. D **55** (1997) 7126 [hep-ph/9611324].

[250] M. Cacciari and M. Krämer, Talk given at the Workshop on Future Physics at HERA, Hamburg, Germany, 30-31 May 1996 [hep-ph/9609500].